NTNU – Trondheim
Norwegian University of
Science and Technology

Modelling the Effect of Continuous Circulation on Downhole Pressure Oscillations Caused by Rig Heaving

Anders Rønning Dahlen

Master of Science in Cybernetics and Robotics
Submission date: June 2015
Supervisor: Ole Morten Aamo, ITK

Norwegian University of Science and Technology
Department of Engineering Cybernetics

NTNU
Norges teknisk-naturvitenskapelige universitet

Fakultet for informasjonsteknologi, matematikk og elektroteknikk

Institutt for teknisk kybernetikk

HOVEDTOPPGAVE

Kandidatens navn: Anders Dahlen

Fag: Teknisk Kybernetikk

Oppgavens tittel: Modelling the effect of continuous circulation on downhole pressure oscillations caused by rig heaving

Bakgrunn

In drilling operations performed in the oil and gas industry it is important to control pressure of the drilling fluid, also called drilling mud. Drilling mud is used primarily for removing cuttings from the well. It is injected at high pressure at the top of the drill string. At the end of the drill string, called the drilling bit, the drilling mud gets into the annulus and then rises together with cuttings up to the surface. At the surface, the cuttings are separated from the mud and the cleaned mud is reinjected into the drill string for further circulation. Apart from removing cuttings from the well, drilling mud is also needed for pressurizing the well. If the pressure in the well is too low, the pressure of the surrounding rock formation can make the well collapse and the drill string gets stuck. At the same time, if the pressure exceeds a certain threshold, it may fracture the well leading to costly consequences. For this reason, it is important to control mud pressure in the well.

In managed pressure drilling (MPD) operations, the well is sealed at the top and the pressure is controlled by opening/closing the valve that releases the mud at the top of the well. This technology has proven successful when drilling from stationary platforms. When drilling from a floater, however, the heaving motion of the floater causes major pressure fluctuations in the well, which must be compensated for using automatic control. Several studies have been performed in the search for a remedy for the problem, all considering main pump shutdown during connections. The objective of this project is to investigate the effect of continuous circulation on the pressure oscillations. In order to do so, a substantial revision of our models is needed. The following points should be addressed by the student:

Oppgave:

1) Review prior work on the heave-problem, and in particular work on modelling.
2) Mathematical model: suggest a mathematical model incorporating drill string flow, annulus flow, drill string elasticity and appropriate boundary conditions. Implement the model in MATLAB/SIMULINK using an appropriate spatial discretization scheme.
3) Perform a simulation study that demonstrates the capabilities of the model. Explore different scenarios and study downhole pressure oscillations the effect of continuous circulation on pressure.
4) If time permits, do one or more of the following:
    a. Implement an appropriate user interface for the model.
    b. Set up a case for simulating the laboratory setup at the petroleum department.
    c. Test control strategies for attenuating heave pressure oscillations (several methods are suggested in the literature, but you may suggest your own as well).
5) Write a report.

Faglærer/Veileder: Professor Ole Morten Aamo

Abstract

In the oil and gas industry a new technology known as Managed Pressure Drilling (MPD) is emerging, allowing for faster and more accurate well pressure control. MPD differs from conventional drilling methods by closing the well using a controlled choke, often in combination with a backpressure pump allowing for automatic pressure control. When the drill string is extended the pipe is typically sealed of and detached from the MPD system. This process is time consuming and limits pressure control, because the mud flow is stopped. The Continuous Circulation System was developed to allow for better pressure control during connections and reducing connection time. For these technologies to become viable for use on floating rigs advanced control algorithms are necessary. To be able to test such system simulators are necessary. In this thesis a transmission line containing the mud column in the pipe and the annulus coupled through an elastic pipe is presented in the frequency domain. A set of Robin boundary conditions representing CCS is developed and coupled with a pressure node. A Ritz approximation is developed in order to discretize the transmission line, and the Laguerre-Gram model order reduction method is applied to obtain rational transfer function approximation. Some likely numerical issues are discussed with this method.

Sammendrag

I olje og gass industrien har en ny og muliggjørende teknologi kalt Kontrollert Trykk Boring (*Managed Pressure Drilling*), eller MPD, begynt å få fotfeste. Ved bruk av denne teknologien kan brønntrykket kontrolleres raskere og mer nøyaktig. Forskjellen på konvensjonell boring og boring med MPD er at brønnen er forseilet og trykket justert automatisk ved bruk av pumper. Under forlenging av borestrengen blir den koblet vekk fra brønnen og MPD-systemet, noe som tar mye tid. Under denne prosessen blir også da flyten av borevæske stoppet, noe som vanskeligjør kontrollen av brønntrykket. Ett Kontinuerlig Flytsystem (*Continuous Circulation System*), eller CCS, har blitt utviklet for å redusere tilkoblingstiden og å opprettholde flyten av borevæske. For at denne teknologien skal kunne brukes kommersielt på flytende rigger må avanserte reguleringsmetoder brukes, for dette trengs gode matematiske modeller. I denne oppgaven er en transmisjonslinje som modellerer borevæsken i drillstrengen og ringrommet, og er koblet sammen via ett elastisk rør presentert i frekvensplanet. Ett sett med Robin grensebetingelser, som tar hensyn til kontinuerlig flyt, blir modellert. Grensebingelsene nedhulls blir så koblet via en trykknode, slik at trykk og flyt blir koblet. En Ritz tilnærming blir utledet for å diskretisere transmissionslinjen, og en Laguerre-Gram modellreduksjon blir brukt for å finne rasjonelle transferfunksjoner som tilnærmer transmisjonslinen. Noen sannsynelige numeriske problemer blir også diskutert.

Preface

This report is the result of a master thesis performed during the spring semester 2015. This report is completing the my Master of Science in Engineering Cybernetics at the Norwegian University of Science and Technology (NTNU).

I would like to thank my supervisor, Professor Ole Morten Aamo for the interesting assignment and excellent guidance throughout the semester. In addition I would like to thank my family for their support and encouragement throughout my studies, and my friends and Frokostklubben V.I.P. for making my years in Trondheim into the incredible experience it has been.

Anders Rønning Dahlen
Trondheim, June 2015

Table of Contents

Chapter 1

Introduction

1.1 Motivation

During drilling operations performed in the oil and gas industry it is important to control the pressure of the drilling fluid, called drilling mud or just mud. One of the primary tasks of the drilling mud is to remove cuttings from the well. The mud is injected at high pressure into the pipe and flow down and through the drill bit continuing back up the annulus carrying cuttings up to the surface. At the surface a separator is used to remove the cuttings from the mud, and the cleaned mud is reinjected into to the system.

In addition to remove cuttings from the well, drilling mud is used to pressurize the well in order to maintain its integrety. If the pressure in the well becomes to low, the pressure in the surrounding rock formation may cause hydrocarbons to leak into the drilling mud, or a well collapse. Similarly if the pressure becomes to high the well might fracture, that can lead to loss of circulation or hydrocarbons leaking into the drilling mud. In any case costly consequences are almost certain.

In managed pressure drilling (MPD) operations the well is sealed topside, making a closed system, where the pressure is controlled using the annulus release valve. For more about different techniques and tools utilized in MPD operations the reader is referred to the master thesis by Martin (2006). By controlling the pressure dynamically, smaller pressure windows become viable; increasing the potential yield for existing fields, and making previously undrillable reservoirs drillable. This technology has proven successful when drilling from stationary platforms. When drilling from floating vessels, the heave motion cause major pressure fluctuations in the drilling well. These fluctuations are fast and must therefore be compensated for automatically.

Several studies have previously been completed either investigating or searching for solutions for this problem, all of which consider shutting down the main pump during connections. By shutting down the main pump during connections, a lot of time is wasted waiting for the pump to stop and start. As a solution to this a continous ciculation system (CCS) has been developed (Jenner et al. (2005)), where the main pump is not shut down during connections increasing uptime, and hence profitability. The motivation for this

thesis is to investigate the effects of heave on the downhole pressure, in a drilling system equipped with CCS.

1.2 Outline and Contribution

In chapter 2 the reader is introduced to terms and equippment used in drilling operations. The CCS is also introduced and a connection with heave problem is served. Chapter 3 presents some background on modelling and a hydraulic transmission line is stated in the frequency domain. A set of boundary conditions are stated in chapter 4 aswell as a pressure node used to model the downhole pressure. A Ritz approximation is developed in chapter 5 in order to discretize the stated transmission line, and the Laguerre-Gram model order reduction method is presented in order to obtain rational transfer function approximations. A frequency analysis is performed in chapter 6, and the results are discussed in chapter 7 and concluded in chapter 8.

1.3 Task Description

- Review prior work on the heave induced pressured oscillations, with emphasis on modeling.
- Suggest a mathematical model incorporating drill string flow, annulus flow, drill string elasticity and appropriate boundary conditions.
- Implement the suggested model using Matlab/Simulink.
- Perform a simulation study that demonstrate the capabilities of the model. Study the downhole pressure oscillations for different scenarios.
- Write a report.

Chapter 2

Background on Drilling

The purpose of this chapter is to give the reader a brief introduction to necessary terms in drilling. An introduction to the concepts of managed pressure drilling (MPD) and the continous circulations system (CCS) is then served. Lastly the relation between floating rigs equipped with MPD and CCS, and the heave problem is introduced. This chapter is mainly based on Totland (2014), Deveraux (2012), Rehm et al. (2008), Jenner et al. (2005) and Martin (2006).

2.1 Drilling Terms and Equipment

This section provides a short description of some common terms and equipment in drilling operations that the reader should be familiar with. For the remainder of this thesis these terms will be used frequently.

Rig: is a complete installation of equipment needed to perform drilling operations. Marine rigs are classified as either floating or bottom supported rigs. Examples of floating rigs are semi-submersibles and drilling ships. Examples of bottom supported rigs are jackup rigs and fixed platforms.

Drill pipe: a string of connected hollow pipe sections. Each pipe section is typically 9.5m long. The drill pipe is where the drilling mud is pumped down.

Drill bit (or just bit): a device placed at the lower end of the drill pipe, designed to cut rock formations. The bit is equipped with nozzels, leading the drilling fluid from the drill pipe into the downhole part of the well.

Bottom hole assembly (BHA): a construction connecting the drill pipe and the drill bit. This construction contain a variaty of instruments and other mechanisms to improve drilling operations.

Drill string: is the complete structure of drill pipe, drill bit and BHA.

Annulus: is the space between the drill string and the well wall. This is where the drilling mud is flowing up, carrying out cuttings.

Drilling mud (or just mud): a fluid pumped down through the drill string into the bottom hole, and back up the annulus. When the mud returns from the annulus it is lead to separators and cleaned, recycling it back to the system. The drilling mud serves several purposes, among others pressure control, removal of cuttings, cooling of the drill bit and to minimize reservoir damage.

2.2 Conventional Drilling

Different technologies have been developed over many years in order to produce oil and gas from offshore reservoirs. Conventional drilling operations consist of a rig with a complete installation of drives, pumps and other equipment, controlled by field engineers and operators.

Wells are created by rotating the drill string and lowering it to the seabed, where the rock formations are then penetrated. During drilling, mud is pumped at high pressures down and through the drill string and back up again through the annulus. A challenge related to drilling is maintaining the correct well pressure. That is keeping the annulus and downhole pressure inside what is known as a pressure window. The lower boundary of the pressure window is given by the surrounding rock formations collapse and pore pressures, and the upper boundary by its fracture pressure.

The collapse pressure is defined as the pressure needed to keep the rock formation from collapsing in on itself. If this happens the drill string will often get stuck or twisted off, and there will be a loss of circulation resulting in a significant downtime. The pore pressure is given by the pressure of the fluid inside the pores of the rock formation. If the well pressure decrease below the pore pressure, unwanted fluids and sediments will leak into to the well. This may lead to a blowout, releasing oil and/or gas into the air. The result of a blowout can be disastrous (McAndrews (2011)). Similarly if the pressure becomes higher than the rock formations fracture pressure the well will fracture, causing drilling mud to leak into the surrounding rock formation. If this happens the rock formation will fracture, and as a result the drill string may be damaged or get stuck. In any case, if the pressure window is broken costly consequences are expected.

Conventionally the bottom hole pressure is controlled by adjusting the density of the drilling mud, using chemicals and weighting materials. This is obviously a time consuming process as the drilling mud has to be exchanged in the entire well, increasing the nonproductive time of the rig. Another technique in use is to adjust the frictional pressure in the well by changing the circulation rate of the mud. One disadvantage of this method is zero control of pressure when subject to zero flow.

2.3 Managed Pressure Drilling

Normally drilling operations are very costly, and naturally the petroleum industry is always searching for solutions that will minimize economical cost and maximize drilling

efficiency. Using conventional drilling methods costly delays often arise, such as differentially stuck pipe, circulation loss and narrow pressure margins. Subsequently these delays lead to large economical costs.

In the master thesis by Martin (2006) some statistical data are presented for the time period $1993-2002$. Showing that more than 20% of operational days were nonproductive, and approximatly 40% of the nonproductive time was related to drilling operations. This data in supported by Rehm et al. (2008) and Godhavn (2010). The MPD discipline have arised due to the high costs of nonproductive time, contributing to reduce problems related to drilling operations.

MPD operations work by automatic pressure control techniques during drilling. In general this is done by sealing of the top of the well, and controlling the pressure by opening/closing teh valve releasing the mud. This allows for a faster and and more accurate control of the well pressure, compared to conventional drilling methods. This in turn will increase production rate by decreasing nonproductive time, aswell as allowing for drilling in more narrow pressure windows.

2.4 Continous Circulation System

The continous circulation system (CCS) (Jenner et al. (2005)) is a technology that enables the driller to add connections to the drill string without stopping fluid circulation. Allowing for maintaing a constant bottom hole pressure during drill string extensions. In conventional drilling operations the mud circulation is stopped before a pipe segment is added, allowing for numerous problems due to pressure surges and zero flow.

Some considerable advantages of CCS is reduced total connection time and a reduction in nonproductive time related to connection problems. Another advantage is by eliminating the pressure surges experienced during connections smaller pressure windows become feasable; allowing for a better production yield from many already drilled wells, aswell as making previously infeasable fields feasable.

2.5 Heave Motion

MPD operations with and withtout CCS have been shown successfull for fixed rigs. For floating rigs heave motion is known to cause significant pressure fluctuations. During drilling heave compensation techniques are often used, decoupling the drill string from the ocean wave disturbance. However during pipe extensions, the drill string is normally detached from the heave compensation system and fixed with the rig motion; in turn leading to pressure fluctuations in the drilling mud, aswell as stretching and contracting the pipe itself. In some cases these pressure fluctuations break the pressure window, leading to costly consequences. Because of these ocean wave induced pressure fluctuations and its problems MPD operations are usually only done in good weather conditions.

Chapter 3

Hydraulic Transmission Line

3.1 Introduction

In this chapter a distributed parameter hyperbolic model for heave-induced pressure fluctuations is presented for a floating rig outfitted for MPD operations with a CCS.

Many different models have previously been presented modeling the dynamics of a floating rig equipped with a MPD system, most of which only consider the annulus flow. In its simplest form the flow and pressure dynamics in the annulus can be modeled using a one dimensional wave equation; which is a distributed parameter hyperbolic system. To simulate such a model in the time domain, a spatial discretization is typically applied.

In Kaasa and Stamnes (2011) an ordinary differential equation with three dynamic states was developed. Because of the models low order it fails to capture the distributed nature of the system, in turn limiting it's validity to very small frequencies, as shown in Pavlov et al. (2010). To address this problem Landet et al. (2012) used a higher order discretization, based on the control volume method. Using this higher order model, the distributed nature of the system dynamics was much better captured. In Aarsnes et al. (2012) the control volume method was further investigated, who also noted the possible occurence of reconance.

In the mentioned litterature only the annulus dynamics were considered. In papers such as Chung and Whitney (1981), Niedzwecki and Thampi (1988) and Tikhonov and Safronov (2002) the significance of the pipe elasticity were investigated, which was found to be important to capture the entire relevant frequency range. In Miller and Young (1985) the significance of the pressure dynamics of the mud column were investigated, and established by the experiments of Namba et al. (2010).

Extending the results of Burkhardt (1961) a time-domain model predicting the surge/swab pressure in pipe-tripping operations is given in Mitchell (1988) and Mitchell (2004). This model includes the elasticity of the pipe, and the dynamics of the mud column in both the pipe and the annulus. In his model the annulus and pipe flow were also coupled through a dynamic downhole model. However the model was designed for pipe-running and pipe-tripping operations, and does not include periodic pipe movement.

A fully coupled dynamic model of the annulus and pipe flow connected through an elastic pipe was presented in Aarsnes et al. (2013), including an exact solution in the frequency domain. In Stecki and Davis (1986a) and Stecki and Davis (1986b) it was shown both theoretically and experimantally that the effect of a radially distributed velocity profile is necessary to capture fast transients, such as pressure fluctations caused by piston like systems. To better capture these effects the model presented in Aarsnes et al. (2013) was extended using this radially ditributed velocity profile in Aarsnes et al. (2014), and a similar exact solution in the frequency domain was presented.

In the next section the model from Aarsnes et al. (2014) is presented, and put on a form suitable for the Ritz approximation developed in chapter 5. The analytical frequency domain from Aarsnes et al. (2013) and Aarsnes et al. (2014) solution is then stated in the last section.

3.2 Hydraulic Transmission Line

In this section the dynamic model in Aarsnes et al. (2014) is presented. First a general expression for the equation of continuity and state of a fluid in an elastic conduit is presented in the frequency domain. Then momentum balance for a fluid in an elastic conduit is presented, inlcuding its solution in the frequency domain.

Equation of continuity and state of mud in an elastic conduit Using the first-principle relation of the one dimensional continuity equation combined with the equation of state, relating pressure p to density ρ, equation (3.1) is obtained. Where β is the bulk-modulus of the drilling mud.

$$\frac{\partial p(x,t)}{\partial t} + \beta \frac{\partial \bar{v}}{\partial x} = 0 \tag{3.1}$$

Because the fluid in the annulus and the pipe is flowing in an elastic conduit, pressure fluctuations will cause the conduit to expand and contract. To account for this the bulk-modulus in (3.1) is exchanged by an effective bulk-modulus.

First let $\mathcal{B} := \{a, i\}$, where a and i are indices representing the annulus and pipe conduits respectively. Now let $(n, m) \in \mathcal{B}$ be two constant such that $n \neq m$. The effective bulk-modulus (Mitchell (1988)) for conduit n can now be stated according to equation (3.2). Where $\bar{A}_n$ is the nominal cross sectional area of the n'th conduit and A_n is assumed to be a linear function in pressure, making $\bar{\beta}_n$ constant.

$$\frac{1}{\bar{\beta}_n} := \frac{1}{\bar{A}_n} \frac{\partial A_n}{\partial p_n} + \frac{1}{\beta} \tag{3.2}$$

Including the effect of pressure changes in conduit m equation (3.1) can be rewritten according to equation (3.3).

$$\frac{1}{\bar{\beta}_n} \frac{\partial p_n}{\partial t} + \left(\frac{1}{\bar{A}_n} \frac{\partial A_n}{\partial p_m} \right) \frac{\partial p_m}{\partial t} + \frac{\partial \bar{v}_n}{\partial x} = 0 \tag{3.3}$$

In equation (3.3) x is the axial position and t is time. Taking the Laplace transform of equation (3.3) and rearranging, equation (3.4) is obtained, with paramters given by definition (3.5). Where the Laplace transformed variables of pressure and velocity is denoted

by its capital letters.

$$\frac{\partial \bar{V}_n}{\partial x} = -Y_n P_n - Y_{n,x} P_m \tag{3.4}$$

$$Y_n = s\frac{1}{\bar{\beta}_n}, \qquad Y_{n,x} = s\frac{1}{\bar{A}_n}\frac{\partial A_n}{\partial p_m} \tag{3.5}$$

Momentum balance of mud in an elastic conduit. The momentum balance is given by the Navier-Stokes equation (Cengel and Cimbala (2010)). Assuming axis-symmetric flow with a negligible radial component the momentum balance is, after linearization, given by equation (3.6). Where r is radial position, v is mud velocity and p denote the pressure. The parameters ν and ρ_0 are kinematic viscosity and mud density respectivly.

$$\rho_0 \frac{\partial v}{\partial t} = -\frac{\partial p}{\partial x} + \nu\rho_0 \left(\frac{\partial^2 v}{\partial r^2} + \frac{1}{r}\frac{\partial v}{\partial r} \right) \tag{3.6}$$

Laplace transforming equation (3.6), and letting $V_n(x, r, s)$ be the Laplace transformed axial velocity component, yields equation (3.7). Which can be recognized as a Bessel function with an inhomogeneity due to the pressure gradient. Assuming that this gradient is independent of the radial component r, the genereal solution of equation (3.7) is given by equation (3.8), with ξ defined in equation (3.9).

$$sV(x, r, s) = -\frac{1}{\rho_0}\frac{\partial P(x, s)}{\partial x} + \nu \left(\frac{\partial^2 V(x, r, s)}{\partial r^2} + \frac{1}{r}\frac{\partial V(x, r, s)}{\partial r} \right) \tag{3.7}$$

$$V(x, r, s) = h^{(1)}(x, s)H_0^{(1)}(\xi r) + h^{(2)}(x, s)H_0^{(2)}(\xi r) - \frac{1}{\rho_0 s}\frac{\partial P(x, s)}{\partial x} \tag{3.8}$$

$$\xi = i\sqrt{\frac{s}{\nu}} \tag{3.9}$$

The components $H_0^{(1)}$ and $H_0^{(2)}$ of equation (3.8) are the zeroth order Hankel functions[1] of the first and second kind respectively, and $h^{(1)}$ and $h^{(2)}$ are their respective constants of integration.

To eliminate radial dependency, the velocity is averaged over the cross-sectional area A of its conduit, resulting in equation (3.11).

$$\bar{V} = \frac{2\pi}{A}\left[h^{(1)} \int_{r_0}^{r_1} H_0^{(1)}(\xi r) r dr + h^{(2)} \int_{r_0}^{r_1} H_0^{(2)}(\xi r) r dr \right] - \frac{1}{\rho_0 s}\frac{\partial P}{\partial x} \tag{3.10}$$

$$= \frac{2\pi}{A}\left[h^{(1)} I^{(1)} + h^{(2)} I^{(2)} \right] - \frac{1}{\rho_0 s}\frac{\partial P}{\partial x} \tag{3.11}$$

$$I^{(1)} := \frac{1}{\xi}\left[H_1^{(1)}(\xi r_1) r_1 - H_1^{(1)}(\xi r_0) r_0 \right] \tag{3.12}$$

$$I^{(2)} := \frac{1}{\xi}\left[H_1^{(2)}(\xi r_1) r_1 - H_1^{(2)}(\xi r_0) r_0 \right] \tag{3.13}$$

[1] As noted in Aarsnes et al. (2014), the basis of the solution of (3.7) in the context of hydraulic transmission lines are usually expressed as Bessel functions. However for annular flow Bessel functions yields a numerically ill-posed problem, and therefore Hankel functions are used instead.

3.2.1 Pipe Flow Subsystem

The equation of continuity and state for the mud in pipe subsystem is obtained by using equation (3.4) with $n = i$ and $m = a$, resulting in equation (3.14). Where the admittance terms Y_i and $Y_{i,x}$ are stated in equation (3.15).

$$\frac{\partial \bar{V}_i}{\partial x} = -Y_i P_i - Y_{i,x} P_a \tag{3.14}$$

$$Y_i = s\frac{1}{\bar{\beta}_i}, \qquad Y_{i,x} = s\frac{1}{\bar{A}_i}\frac{\partial A_i}{\partial p_a}, \qquad \frac{1}{\bar{\beta}_i} = \frac{1}{\bar{A}_i}\frac{\partial A_i}{\partial p_i} + \frac{1}{\beta} \tag{3.15}$$

The momentum balance is found by using equation (3.11) with appropriate radial boundary conditions. The flow considered is in a pipe of radius r_0, where the pipe walls are moving with velocity $V_p(x, s)$. Assuming that the noslip condition (Cengel and Cimbala (2010)) holds at the pipe wall, the boundary condition $V_i(x, r, s) = V_p(x, s)$ can be imposed. The other boundary condition can be defined by assuming finite velocity at the center of the pipe, resulting in $h^{(1)} = h^{(2)} = h_i$. Solving equation (3.8) for h_i gives the relation (3.16), with the frequency dependant parameter C defined according to (3.17).

$$h_i = C\frac{1}{\rho_0 s}\frac{\partial P}{\partial x} + CV_p \tag{3.16}$$

$$C := \left(H_0^{(1)}(\xi r_0) + H_0^{(2)}(\xi r_0)\right)^{-1} \tag{3.17}$$

Now the momentum equation (3.11) can be stated for the mud in pipe subsystem according to equation (3.18), with impdances given by equation (3.19).

$$\frac{\partial P_i}{\partial x} = -\bar{V}_i Z_i + Z_i X_i V_p \tag{3.18}$$

$$Z_i = \rho_0 s\left(1 - C\left[I_i^{(1)} + I_i^{(2)}\right]\frac{2\pi}{\bar{A}_i}\right)^{-1}, \qquad X_i = \frac{2\pi}{\bar{A}_i} C\left[I_i^{(1)} + I_i^{(2)}\right] \tag{3.19}$$

$$I_i^{(1)} = \frac{1}{\xi} H_1^{(1)}(\xi r_0) r_0, \qquad I_i^{(2)} = \frac{1}{\xi} H_1^{(2)}(\xi r_0) r_0 \tag{3.20}$$

3.2.2 Annulus Flow Subsystem

Similarly to the previous section the equation of continuity for the mud in annulus subsystem can be stated using equation (3.4) with $n = a$ and $m = i$ resulting in equation (3.21), with admittance terms given by equation (3.22).

$$\frac{\partial \bar{V}_a}{\partial x} = -Y_a P_a - Y_{a,x} P_i \tag{3.21}$$

$$Y_a = s\frac{1}{\bar{\beta}_a}, \qquad Y_{a,x} = s\frac{1}{\bar{A}_a}\frac{\partial A_a}{\partial p_i}, \qquad \frac{1}{\bar{\beta}_a} = \frac{1}{\bar{A}_a}\frac{\partial A_a}{\partial p_i} + \frac{1}{\beta} \tag{3.22}$$

To find the momentum balance for the annulus flow, equation (3.11) is again used, however with different boundary conditions. Consider an annulus with an inner radius r_1 and an outer radius r_2, where the inner pipe is moving with velocity $V_p(x,s)$ and the outer wall is standing still. I.e. $V_a(x,r_1,s) = V_p(x,s)$ and $V_a(x,r_2,s) = 0$. Using these boundary conditions together with equation (3.8) gives the relations (3.23).

$$\begin{bmatrix} H_0^{(1)}(\xi r_2) & H_0^{(2)}(\xi r_2) \\ H_0^{(1)}(\xi r_1) & H_0^{(2)}(\xi r_1) \end{bmatrix} \begin{bmatrix} h_a^{(1)} \\ h_a^{(2)} \end{bmatrix} = \begin{bmatrix} \frac{1}{\rho_0 s}\frac{\partial P_a(x,s)}{\partial x} \\ \frac{1}{\rho_0 s}\frac{\partial P_a(x,s)}{\partial x} + V_p(x,s) \end{bmatrix} \tag{3.23}$$

Solving equation (3.23) for $h_a^{(1)}$ and $h_a^{(1)}$ gives the constants of integration stated in equation (3.24). With parameters given by equation (3.25).

$$h_a^{(1)} = D^{(1)}\frac{\partial P_a(x,s)}{\partial x} + E^{(1)}V_p \tag{3.24a}$$

$$h_a^{(2)} = D^{(2)}\frac{\partial P_a(x,s)}{\partial x} + E^{(2)}V_p \tag{3.24b}$$

$$\begin{aligned} D^{(1)} &= -\frac{H_0^{(2)}(\xi r_2) - H_0^{(2)}(\xi r_1)}{W} & E^{(1)} &= -\frac{H_0^{(2)}(\xi r_2)}{W} \\ D^{(2)} &= \frac{H_0^{(1)}(\xi r_2) - H_0^{(1)}(\xi r_1)}{W} & E^{(2)} &= \frac{H_0^{(1)}(\xi r_2)}{W} \\ W &= H_0^{(1)}(\xi r_2)H_0^{(2)}(\xi r_1) - H_0^{(1)}(\xi r_1)H_0^{(2)}(\xi r_2) \end{aligned} \tag{3.25}$$

The momentum balance for the annulus flow subsystem can now be stated according to equation (3.26). With impedances given by equations (3.27) and (3.28).

$$\frac{\partial P_a}{\partial x} = -\bar{V}_a Z_a + Z_a X_a V_p \tag{3.26}$$

$$Z_a = \rho_0 s\left(1 - \frac{2\pi}{\bar{A}_a}\left[D^{(1)}I^{(1)} + D^{(2)}I^{(2)}\right]\right)^{-1} \tag{3.27}$$

$$X_a = \frac{2\pi}{\bar{A}_a}\left[E^{(1)}I^{(1)} + E^{(2)}I^{(2)}\right] \tag{3.28}$$

$$I_a^{(1)} = \frac{H_1^{(1)}(\xi r_2)r_2 - H_1^{(1)}(\xi r_1)r_1}{\xi} \tag{3.29}$$

$$I_a^{(2)} = \frac{H_1^{(2)}(\xi r_2)r_2 - H_1^{(2)}(\xi r_1)r_1}{\xi} \tag{3.30}$$

3.2.3 Elastic Pipe

In Aarsnes et al. (2014) the derivation from Greenfield and Lubinski (1967) is used to model the pipe as a one dimensional elastic rod. For small deformations the relationship between stress p_p and strain ε is given by $p_p = E\varepsilon$, where E is the Young's modulus. Combining this with the relation of continuity gives equation (3.31).

$$\frac{1}{E}\frac{\partial p_p(x,t)}{\partial t} + \frac{\partial v_p(x,t)}{\partial x} = f_i\frac{\partial p_i(x,t)}{\partial t} - f_a\frac{\partial p_a(x,t)}{\partial t} \tag{3.31}$$

The terms on the right side of equation (3.31) arrise from the hoops-strain effect, induced by the varying pressure on the inside and outside of the pipe. These pressure variations leads to and axial compression/extension dynamical behaviour in the pipe. The parameters f_i and f_a are the hoop-strain coefficients. Taking the Laplace transform of (3.31) results in equation (3.32). Where the shunt admittance is given by equation (3.33).

$$\frac{\partial V_p}{\partial x} = f_i s P_i - f_a s P_a - Y_p P_p \tag{3.32}$$

$$Y_p = \frac{s}{E} \tag{3.33}$$

The momentum balance for the pipe is given by equation (3.34), where the term $k_p v_p$ accounts for the force per unit length exerted on the pipe as it drags along the walls of the well and the viscous drag.

$$\rho_p \frac{\partial v_p}{\partial t} = -\frac{\partial p_p}{\partial x} - k_p v_p \tag{3.34}$$

Laplace transforming equation (3.34) gives the transfer function (3.35), with impedance given by equation (3.36).

$$\frac{\partial P_p}{\partial x} = -Z_p V_p \tag{3.35}$$

$$Z_p = \rho_p s + k_p \tag{3.36}$$

3.2.4 Summary

Using equations (3.14), (3.21) and (3.32) the pipe and flow velocities can be rewritten as a ordinary differential matrix equation, with respect to the axial length x, resulting in equation (3.37). Similarly using equations (3.18), (3.26) and (3.35) for pressure gives equation (3.38). With pressure $P = [P_i, P_a, P_p]^\top$ and flow velocity $V = \left[\bar{V}_i, \bar{V}_a, V_p\right]^\top$, and the admittance matrix Y and impedance matrix Z is defined in equations (3.41). All parameters are conveniently summarized in table A.1 and A.2

$$\frac{\partial V}{\partial x} = YP \tag{3.37}$$

$$\frac{\partial P}{\partial x} = ZV \tag{3.38}$$

$$Y := \begin{bmatrix} -Y_i & -Y_{i,x} & 0 \\ -Y_{a,x} & -Y_a & 0 \\ f_i s & -f_a s & -Y_p \end{bmatrix} \tag{3.39a}$$

$$Z := \begin{bmatrix} -Z_i & 0 & Z_i X_i \\ 0 & -Z_a & Z_a X_a \\ 0 & 0 & -Z_p \end{bmatrix} \tag{3.39b}$$

3.3 Analytical Solution in the Frequency Domain

To be able to compare the later defined Ritz-approximation with the analytical frequency solution of the system of equation given by equations (3.37) and (3.38), it's analytical frequency domain solution is here presented.

Let $y = [\bar{V}_i, P_i, \bar{V}_a, P_a, V_p, P_p]$, then equations (3.37) and (3.38) can be rewritten according to equation (3.40) where the matrix A is defined according to equation (3.41). The frequency dependent parameters defining the matrix A can be found in table A.1 and A.2.

$$\frac{\partial y}{\partial x} = Ay \tag{3.40}$$

$$A = \begin{bmatrix} 0 & -Y_i & 0 & -Y_{i,x} & 0 & 0 \\ -Z_i & 0 & 0 & 0 & Z_i X_i & 0 \\ 0 & -Y_{a,x} & 0 & -Y_a & 0 & 0 \\ 0 & 0 & -Z_a & 0 & Z_a X_a & 0 \\ 0 & f_i s & 0 & -f_a s & 0 & -Y_p \\ 0 & 0 & 0 & 0 & -Z_p & 0 \end{bmatrix} \tag{3.41}$$

As equation (3.40) is a linear ordinary differential matrix equation, it's general solution is given by equation (3.42), where B is the constant of integration.

$$y(x) = e^{Ax} B \tag{3.42}$$

The six constant of integration $B_1, B_2, ..., B_6$ constituting the matrix B can be found by specifying six linearly independent boundary conditions in the frequency domain. These boundary conditions can then be stated in the basis given by equation (3.43).

$$\bar{y}(x) = e^{Ax} \tag{3.43}$$

Then the constant of integration B can be found by solving the algebraic of equation (3.44). Where D is a matrix containing output relations expressed in the basis (3.43), and b contains the exogeneous inputs to the system.

$$DB = b \tag{3.44}$$

Chapter 4

Downhole Model and Boundary Conditions

4.1 Introduction

This chapter suggest a set of boundary conditions for the hydraulic transmission line given by equations (3.37) and (3.38). A pressure node is developedusing the the definition of bulk-modulus. The downhole boundary conditions for the transmission line are then defined using this pressure node as an interconnecting model.

To develope the pressure node and define the needed boundary conditions the well has to be divided into three control volumes. This is done in the next section.

4.2 Control Volumes

The well can conveniently be divided into three control volumes, one for the hydraulic transmission line, one for the downhole pressure node, and the last one is used to define the boundaries inbetween. In figure 4.1 the different control volumes can be seen, where the dashed lines are the borders of the control volumes. The heigth from 0 to L represents the control volume for the hydraulic transmission line, where L is the approximate nominal length of the drill pipe. The heigth from d to h_{bit} defines the downhole control volume, where d is distance from 0 to the bottom of the well and h_{bit} is the height of the drill bit above d. Lastly the heigth from h_{bit} to 0 gives the control volume for the boundary conditions.

During connections the drill string will be subject to a heave disturbance topside, resulting in a piston like effect downhole. Because of this piston like effect the heigth h_{bit} will not be constant, giving a dynamic downhole control volume.

The length of the drill bit and BHA is short compared to the drill pipe, and therefore it is reasonable to assume that the drill bit velocity will be approximatly equal to the downhole velocity of the pipe. The approximation of h_{bit} is stated in equation (4.1), where h_{bit}^0 is

the initial height of the drill bit above the well floor.

$$\frac{\partial h_{bit}}{\partial t} \approx v_p(0,t), \quad h_{bit}(0) = h_{bit}^0 \tag{4.1}$$

The downhole control volume $\mathcal{V}_d$ is given by equation (4.2), where A_d is the approximate cross sectional area of the well floor. Differentiating $\mathcal{V}_d$ with respect to time gives the differential equation (4.3) for the downhole control volume.

$$\mathcal{V}_d(t) = A_d h_{bit}(t) \tag{4.2}$$

$$\frac{\partial \mathcal{V}_d}{\partial t} = A_d v_p(0,t), \quad \mathcal{V}_d(0) = A_d h_{bit}^0 \tag{4.3}$$

For simplicity the boundary control volume between the transmission line and the downhole control volume, will be assumed constant. This simplification is reasonable because the heigth oscillations will be small compared to length of the BHA.

4.3 Downhole Pressure Node

The dynamics of the downhole pressure can be developed using the definition of the bulk-modulus with respect to volume, given by equation (4.4). Where β_d is bulk-modulus, p_d is pressure and $\mathcal{V}_d$ is the volume. This definition can be found in many text books considering fluid mechanics, e.g. Cengel and Cimbala (2010).

$$\beta_d = -\mathcal{V}_d(t)\frac{\partial p_d(t)}{\partial \mathcal{V}_d(t)} \tag{4.4}$$

Assuming conservation of mass, and incompressibility in the downhole and boundary control volumes, the volumetric flow into the downhole control volume is $\bar{A}_i \bar{v}_i(0,t)$, and similarly the volumetric flow out of the control volume is $\bar{A}_a \bar{v}_a(0,t)$. Where $\bar{v}_i(0,t)$ and $\bar{v}_a(0,t)$ are the flow velocities from the pipe and the annulus respectivly. In reality the drilling mud will be compressible in these areas, however the flow difference due to compressibilty will be small, and the assumption is reasonable. Using this the substantial derivative $\partial \mathcal{V}$ in equation (4.4) can be stated according to equation (4.5).

$$\partial \mathcal{V}_d(t) = \bar{A}_d v_p(0,t)\partial t + \bar{A}_i \bar{v}_i(0,t)\partial t + \bar{A}_a \bar{v}_a(0,t)\partial t \tag{4.5}$$

As argued in Mitchell (1988) the well walls have elastic properties, because the surrounding rock formation will deform with pressure changes. Assuming, as for the hydraulic transmission line, that the cross sectional well area A_d has a linear relation to the downhole pressure p_d, the effective bulk-modulus $\bar{\beta}_d$ given by equation (4.6) will be constant.

$$\frac{1}{\bar{\beta}_d} = \frac{1}{\bar{A}_d}\frac{\partial A_d}{\partial p_d} + \frac{1}{\beta} \tag{4.6}$$

Exchanging the bulk-modulus β_d in eqauation (4.4) with the effective bulk-modulus $\bar{\beta}_d$, and inserting equation (4.5) into equation (4.4) results in the pressure node (4.7). A

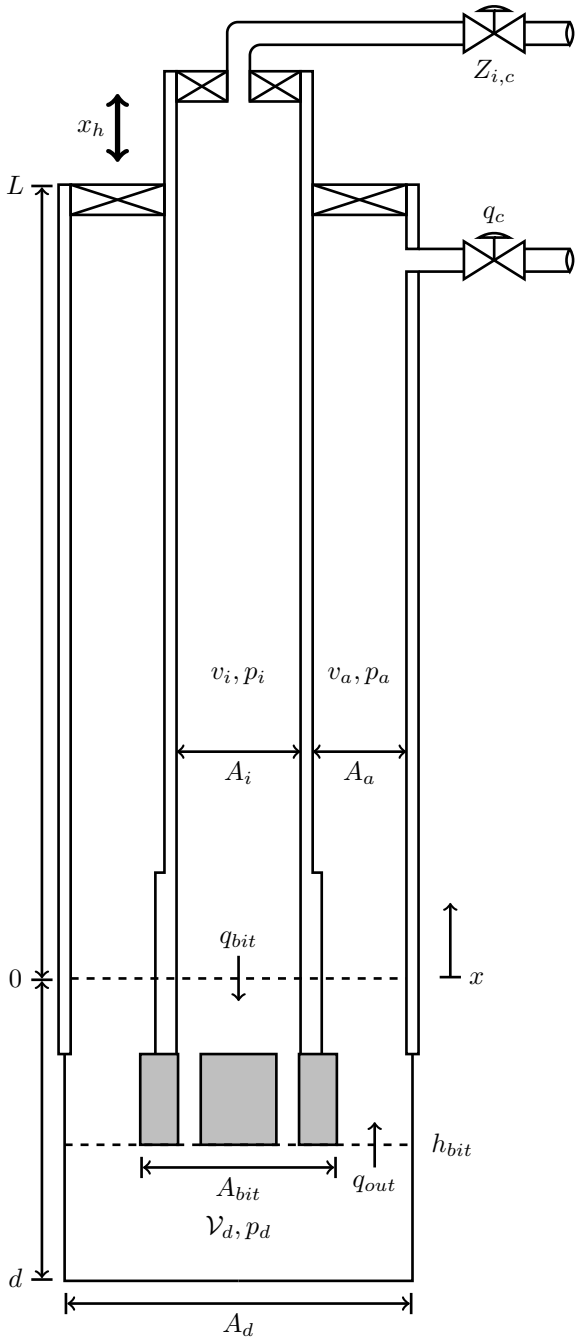

Figure 4.1: Schematic of drilling well.

reasonable estimate of the inital downhole pressure is $p_d^0 \approx mg/A_d$, where g is the gravitational constant and m is the approximate weigth of the entire drillstring.

$$\frac{\partial p_d}{\partial t} = -\frac{\bar{\beta}_d}{\mathcal{V}_d(t)} \left(\bar{A}_d v_p(0,t) + \bar{A}_i \bar{v}_i(0,t) + \bar{A}_a \bar{v}_a(0,t) \right), \quad p_d(0) = p_d^0 \tag{4.7}$$

4.4 Boundary Conditions

A set of boundary conditions is defined in this section, completing the hydraulic transmission line given by equations (3.37) and (3.38). These boundary conditions also serve as a connection between the the downhole pressure node given by equation (4.7) and the transmission line.

Because the downhole model is derived using bulk modulus, its inputs are given as flow. It is therefore natural to use flow as outputs and pressure as inputs at the lower end of the transmission line. Topside controlled chokes manages the inlfux of mass to the pipe and outflux from the annulus, and therefore these boundaries can easily be defined with respect to either pressure or flow. During connections the drillstring will be fixed with the rig, and the pipe will move with the same velocity as the rig, and hence velocity is the natural choice for the topside elastic pipe input. This makes for a set of *Robin* (or *mixed*) boundary conditions (Reddy (1986)).

In the next chapter a rational approximation of the transmission line from the previous chapter is developed, allowing for a multiple input, multiple output realization in the time domain. Therefore the following boundary conditions will be expressed in the time domain and not in the frequency domain. This allows for defining nonlinear boundary conditions, without using complicated nonlinear Laplace transforms.

4.4.1 Topside Boundary Conditions

Let v_i^c and v_a^c be the controlled flow velocity into the pipe and out of the annulus respectivly. Furthermore let x_h be the heave displacement of the rig, and v_h the corresponding heave velocity velocity. The topside boundaries can now be defined accoring to equations (4.8).

$$\bar{v}_i(L,t) = v_i^c(t) \tag{4.8a}$$
$$\bar{v}_a(L,t) = v_a^c(t) \tag{4.8b}$$
$$v_p(L,t) = v_h(t) \tag{4.8c}$$

The heave velocity v_h can be veiwed as an external disturbance, and can be modeled using a variety of sea wave spectrum models, see e.g. chapter 8 in Fossen (2011).

4.4.2 Downhole Pipe Flow Boundary Condition

During drilling operations the drilling mud flows from the pipe through nozzles in the drill bit and then into the well. According to Warren (1989) the pressure loss $\Delta p_{bit}(t) = p_i(0,t) - p_d(t)$ over the drill bit is usually calculated using equation (4.9). Where C_d is the nozzles discharge coefficient, d_n is the nozzle diameter and ρ is the density of the

drilling mud. In Warren (1989) it is argued that $C_d \approx 1.03$ is a reasonable estimate for the discharge coefficent for many drill bits.

$$p_i(0,t) = \frac{\rho \bar{v}_i(0,t)^2}{12,031(d_n C_d)^2} + p_d(t) \tag{4.9}$$

4.4.3 Downhole Elastic Pipe Boundary Condition

Due to topside heave the drill bit will experience height oscillations. Assuming that the downhole control volume is small, the dampning caused by the drill bit and BHA motion squeezing the surrounding fluid (as in Aarsnes et al. (2013) and Aarsnes et al. (2014)) can be modeled as a piston/cylinder type dashpot. The resulting momentum balance is given by equation (4.10), where m_{BHA} is the combined mass of the drill bit and BHA, γ is the dampning constant, and $\bar{A}_i$, A_{bit} and A_p are the cross sectional pipe hole area, the cross sectional drill bit area and the cross sectional area of the pipe respectively. Details on how to derive γ can be found in Rao and Yap (1995).

$$A_p p_p(0,t) + \bar{A}_i p_i(0,t) = A_{bit} p_d(t) - m_{BHA} s v_p(0,t) - \gamma v_p(0,t) \tag{4.10}$$

4.4.4 Downhole Annulus Flow Boundary Condition

The area between the downhole control volume and the transmission line control volume in the annulus, can be modeled using theory for internal flow (Cengel and Cimbala (2010)). The pressure drop from the downhole pressure $p_d(t)$ to the bottom side annulus pressure $p_a(0,t)$ can be modeled as a headloss H_l through an annular pipe section, according to equation (4.11). Where ρ is the density of the drilling mud and g is the gravitational constant.

$$P_a(0,t) = P_d(t) - \rho g H_l(\bar{V}_a(0,t)) \tag{4.11}$$

The headloss is modeled by equation (4.12) as a sum of minor and major losses. Where K_l is a loss/resitance coefficient representing the total irreversable loss over the control volume. These losses arrise from the irregular shape of the BHA and the well wall. The parameters L_{bit} and D_{bit} are the approximate lenght and hydraulic diameter of the section respectively.

$$H_l = \frac{K_l}{2g}\left(\bar{V}_a(0,t)\right)^2 + \frac{L_{bit}}{2gD_{bit}}\left(\bar{V}_a(0,t)\right)^2 f_{bit}\left(Re\right) \tag{4.12}$$

It is known that the the flow through the drill bit is turbulent, however less is know about the flow downhole and around the BHA with respect to laminarity and turbulece. For this reason the friction factor f_{bit} is modeled as a blending between a laminar and a tubrulent model, given by equation (4.13). The blending function κ, defined in equation (4.16), is assumed to be linear with respect to the Reynolds number Re in the transitional region; Re_t and Re_l are the Reynolds number thresholds for turbulent and laminar flow respectively. Figure 4.2 shows how the blending function κ transitions for arbitrary tresholds.

$$f_{bit}\left(Re\right) = \kappa\left(Re\right) f_{bit}^{l}\left(Re\right) + \left[1 - \kappa\left(Re\right)\right]\left(Re\right) f_{bit}^{t}\left(Re\right) \tag{4.13}$$

The laminar and turbulent friction functions f_{bit}^{l} and f_{bit}^{t} are given by equation (4.14) and (4.15) respectively, where the turbulent friction is modeled using the Colebrook equation. The Reynolds number is a function of flow velocity and is given by equation (4.17). The paramters ϵ and ν are the surface roughness and kinematic viscosity respectivly.

$$f_{bit}^{l}\left(Re\right) = \frac{64}{Re} \tag{4.14}$$

$$f_{bit}^{t}\left(V_a^0\right) = \left(-1.8\log\left[\frac{6.9}{Re} + \left(\frac{\epsilon}{3.7D_{bit}}\right)^{1.11}\right]\right)^{-2} \tag{4.15}$$

$$\kappa\left(Re\right) = \begin{cases} 1 & , Re \leq Re_l \\ -\frac{Re_t}{Re_l - Re_t} + \frac{1}{Re_l - Re_t}Re & , Re \in \langle Re_l, Re_t \rangle \\ 0 & , Re \geq Re_t \end{cases} \tag{4.16}$$

$$Re = \frac{D_{bit}}{\nu}\bar{V}_a^0 \tag{4.17}$$

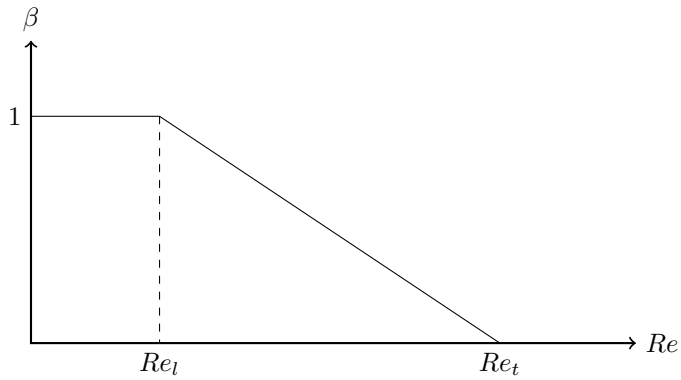

Figure 4.2: Blending function κ plotted with respect to the Reynolds number Re for arbitrary threshold values Re_l and Re_t.

In total seven parameters will have to be determined to apply the above model. For normal pipe systems, these parameters can often be accuratly meassured. However this is not the case at the bottom of a drilling well, as the surrounding rock formation will have both a varying structure and different surface properties, making $\epsilon, K_l, D_{bit}, Re_l$ and Re_t difficult to determine. In reality the fluid in the annulus will also be multiphase, containing both solids, liquids and sometimes gas, making the model less accurate, and tuning of the relevant parameter estimates necassary.

Because of the arduous task in finding and tuning these seven parameters, two simpler alternative models for this boundary condition are presented. Assuming that the boundary volume is small compared to the total drilling well, the pressure drop over drill bit and BHA can be modeled using a standard valve equation. For turbulent flow equation (4.18a)

should be used, where C_t is the discharge coefficient. For laminar flow equation (4.18b) should be used, where C_l is the discharge coefficient.

$$p_a(0,t) = \rho C_t v_a(0,t)^2 - p_d(t) \tag{4.18a}$$
$$p_a(0,t) = \rho C_l v_a(0,t) - p_d(t) \tag{4.18b}$$

The simplicity of these two models is appealing compared to the internal flow model, as it contains only one parameter with a linear relation to the states. Although these parameters does not have any direct physical relations, the estimation problem is for obvious reasons much simpler.

Chapter 5

Ritz Approximation and Polynomial Approximation

5.1 Introduction

The transmission line given by equations (3.37) and (3.38) cannot readily be simulated in the time domain. The modal method presented in Hsue and Hullender (1983) and Hullender et al. (1988) approximates the fluid dynamics given by partial differetial equations (PDE) as a system of linear ordinary differential equations (ODE), so that they can be solved using conventional numerical methods. A comparison study on numerical solution methods of transmission lines done by Watton and Tadmori (1988) concluded that the modal method was the most accurate, user friendly and numerically stable methods available at that time. Some improvements was later introduced to the modal method in the work by Piché and Ellman (1995).

In Mäkinen et al. (2000) a variational formulation of the modal method was developed and three different transient compressible laminar pipe flow models (inviscous, one dimensional viscous, and two dimensional dissipative viscous flow) were considered. A rational approximation in the frequency domain was also presented of the two dimensional dissipative viscous flow model.

In this chapter the Ritz approximation developed in Mäkinen et al. (2000) is extended to coupled transmission lines of the form given by equation (3.37) and equation (3.38). Then the Lagurre-Gram reduced order method presented in Amghayrir et al. (2005) with the extension in Anfinsen (2013) is applied to the Ritz approximation in order to get a rational approximation.

Before formulating the weak problem needed for the Ritz approximation, pressure is eliminated by differentiating equation (3.37) with respect to x, and then inserting it into equation (3.38) giving the wave equation equation (5.1). Where the matrix $\Gamma(s)$ is defined in definition (5.2).

$$\frac{\partial^2 V(x,s)}{\partial^2 x} - \Gamma(s)V(x,s) = 0 \tag{5.1}$$

$$\Gamma(s) := Y(s)Z(s) \tag{5.2}$$

Let $\gamma_{kj}(s)\ \forall k \in \mathcal{S}, \forall j \in \mathcal{S}$ be the elements of $\Gamma(s)$, where the set $\mathcal{S} := \{i, a, p\}$ contains the incices representing each subsystem in the hydraulic transmission line stated in chapter 3. Equation (5.1) can now be rewritten as three coupled equations (5.3) with respect to the elements of $\Gamma(s)$.

$$\frac{\partial^2 \bar{V}_i(x,s)}{\partial x^2} - \sum_{j\in\mathcal{S}} \gamma_{ij}(s) V_j(x,s) = 0 \tag{5.3a}$$

$$\frac{\partial^2 \bar{V}_a(x,s)}{\partial x^2} - \sum_{j\in\mathcal{S}} \gamma_{aj}(s) V_j(x,s) = 0 \tag{5.3b}$$

$$\frac{\partial^2 V_p(x,s)}{\partial x^2} - \sum_{j\in\mathcal{S}} \gamma_{pj}(s) V_j(x,s) = 0 \tag{5.3c}$$

5.2 Weak Formulation

The weak formulation (5.4) (Reddy (1986)) of the coupled equations (5.3) with Robin boundary conditions is obtained by multiplying each equation by a variational parameter $\phi_{m_k} \in H^1_\star(0,L), \forall k \in \mathcal{S}$, and integrating over the domain of $x \in [0, L]$. The set $H^1_\star(0,L)$ is defined in equation (5.5), where $H^1(0,L)$ is a Sobolov space (Reddy (1986)).

$$\int_0^L \left[\frac{\partial^2 V_k(x,s)}{\partial x^2}\phi_{m_k}(x) - \left(\sum_{j\in\mathcal{S}} \gamma_{kj}(s) V_j(x,s) \right) \phi_{m_k}(x) \right] dx = 0 \qquad \forall k \in \mathcal{S}, \qquad \forall \phi_{m_k} \in H^1_\star(0,L) \tag{5.4}$$

$$H^1_\star(0,L) = \{\phi = \phi(x) : \phi \in H^1(0,L), \phi(L) = 0\} \tag{5.5}$$

Using integration by parts the weak form (5.4) can be rewritten according to equation (5.6), where it is used that $\phi_{m_k}(L) = 0$.

$$\int_0^L \left[\frac{\partial V_k(x,s)}{\partial x}\frac{\partial \phi_{m_k}(x)}{\partial x} + \left(\sum_{j\in\mathcal{S}} \gamma_{kj}(s) V_j(x,s) \right) \phi_{m_k}(x) \right] dx = -\sum_{j\in\mathcal{S}} y_{kj}(s) P_j(0) \phi_{m_k}(0) \qquad \forall k \in \mathcal{S}, \qquad \forall \phi_{m_k} \in H^1_0(0,L) \tag{5.6}$$

5.3 Ritz Approximation

The Ritz method is a way to find an approximate solution for a given problem in terms of adjustable paramters. These parameters are are found by either minimizing a functional or

solving the weak form of the given problem, e.g. equation (5.6). Here only the solution of the weak formulation of a problem is considered.

For the variational formulation (5.6), the approximate solution $\widetilde{V}(x)$ is given by equation (5.7a) in terms of adjustable paramters $r_{k,n}$. Where y_{kj} are the elements of the matrix Y from equation (3.37). The shape functions ϕ_n were picked from the complete and linearly independent set of trigonometric functions, similarly to what was done in Mäkinen et al. (2000). To satisfy the mixed boundary conditions stated in the previous chapter the shape functions were more specifically picked as in equation (5.7b). The parameter N is the number of modes in the Ritz approximation, and as $N \to \infty$ then $\widetilde{V}_k(x)$ will converge to $V_k(x)$. For the interested reader convergence and stability properties for the Ritz approximation is proven in Reddy (1986).

$$\widetilde{V}_k(x) = V_k(L) + (x-L)\sum_{j\in\mathcal{S}} y_{kj}(s)P_j(0) + \sum_{n=1}^{N} r_{k,n}\phi_n(x), \qquad \forall k \in \mathcal{S} \tag{5.7a}$$

$$\phi_n(x) = \cos\left(\frac{(2n-1)\pi}{2L}x\right) \tag{5.7b}$$

Inserting the approximation (5.7a) into the weak problem (5.6) gives for each $k \in \mathcal{S}$ equation (5.8). Where it is used that $\phi_{m_k}(0) = \cos(0) = 1$.

$$\begin{aligned}
\int_0^L \Bigg[&\left(\sum_{n=1}^{N} \frac{(2n-1)\pi}{2L}\sin\left(\frac{(2n-1)\pi}{2L}x\right) r_{k,n} - \sum_{j\in\mathcal{S}} y_{kj}(s)P_j(0)\right) \\
&\cdot\frac{(2m_k-1)\pi}{2L}\sin\left(\frac{(2m_k-1)\pi}{2L}x\right) \\
+\sum_{j\in\mathcal{S}}\gamma_{kj}(s)&\left(V_j(L) + (x-L)\sum_{\eta\in\mathcal{S}} y_{j\eta}(s)P_\eta(0)\right)\cos\left(\frac{(2m_k-1)\pi}{2L}x\right) \\
+\sum_{j\in\mathcal{S}}\gamma_{kj}(s)&\sum_{n=1}^{N} r_{j,n}\cos\left(\frac{(2n-1)\pi}{2L}x\right)\cos\left(\frac{(2m_k-1)\pi}{2L}x\right)\Bigg] dx \\
&= -\sum_{j\in\mathcal{S}} y_{kj}(s)P_j(0), \qquad \forall m_k \in \{1,...,N\}
\end{aligned} \tag{5.8}$$

Because of the periodicity of the trigonometric shape functions, there will be two solutions of the definite integral in equation (5.8). These two solutions are when $n = m_k$ and $n \neq m_k$.

For $n \neq m_k$ the solution of the definite integral in equation (5.8) is given by equation

(5.9) for each $n \in \{1, .., N\}$.

$$\begin{aligned}
&\int_0^L \Bigg[\left(\cos\left(\frac{(n-m_k)\pi}{L}x\right) - \cos\left(\frac{(n+m_k-1)\pi}{L}x\right)\right) \\
&\qquad \cdot \frac{(2n-1)(2m_k-1)\pi^2}{8L^2} r_{k,n} \\
&\qquad - \frac{(2m_k-1)\pi}{2L} \sum_{j\in\mathcal{S}} y_{kj}(s) P_j(0) \sin\left(\frac{(2m_k-1)\pi}{2L}x\right) \\
&\quad + \sum_{j\in\mathcal{S}} \gamma_{kj}(s) \left(\cos\left(\frac{(n-m_k)\pi}{L}x\right) + \cos\left(\frac{(n+m_k-1)\pi}{L}x\right)\right) r_{j,n} \\
&+ \sum_{j\in\mathcal{S}} \gamma_{kj}(s) \left[V_j(L) + (x-L) \sum_{\eta\in\mathcal{S}} y_{j\eta}(s) P_\eta(0) \right] \cos\left(\frac{(2m_k-1)\pi}{2L}x\right) \Bigg] dx \\
&= \sum_{j\in\mathcal{S}} \frac{2L\gamma_{kj}(s)}{(2m_k-1)\pi} \left(V_j(L)(-1)^{m_k+1} - \frac{2L}{(2m_k-1)\pi} \sum_{\eta\in\mathcal{S}} y_{j\eta}(s) P_\eta(0) \right) \\
&\quad - \sum_{j\in\mathcal{S}} y_{kj}(s) P_j(0), \qquad \forall n \in \{1, ..., N\}, \quad \forall m_k \neq n \in \{1, ..., N\}
\end{aligned} \tag{5.9}$$

For $n = m_k$ the solution of the definite integral in equation (5.8) is given by equation (5.10) for each $n \in \{1, .., N\}$

$$\begin{aligned}
&\int_0^L \Bigg[\left(\frac{(2n-1)\pi}{2L}\right)^2 \sin^2\left(\frac{(2n-1)\pi}{2L}\right) r_{k,n} \\
&\qquad + \sum_{j\in\mathcal{S}} \gamma_{kj}(s) \cos^2\left(\frac{(2n-1)\pi}{2L}\right) r_{j,n} \\
&\qquad - \frac{(2n-1)\pi}{2L} \sum_{j\in\mathcal{S}} y_{kj}(s) P_j(0) \sin\left(\frac{(2n-1)\pi}{2L}x\right) \\
&+ \sum_{j\in\mathcal{S}} \gamma_{kj}(s) \left[V_j(L) + (x-L) \sum_{\eta\in\mathcal{S}} y_{j\eta}(s) P_\eta(0) \right] \cos\left(\frac{(2n-1)\pi}{2L}x\right) \Bigg] dx \\
&= \frac{L}{2} \left(\frac{(2n-1)\pi}{2L}\right)^2 r_{k,n} + \frac{L}{2} \sum_{j\in\mathcal{S}} \gamma_{kj}(s) r_{j,n} - \sum_{j\in\mathcal{S}} y_{kj}(s) P_j(0) \\
&\quad + \sum_{j\in\mathcal{S}} \frac{2L\gamma_{kj}(s)}{(2n-1)\pi} \left(V_j(L)(-1)^{n+1} - \frac{2L}{(2n-1)\pi} \sum_{\eta\in\mathcal{S}} y_{j\eta}(s) P_\eta(0) \right), \\
&\qquad \forall n \in \{1, .., N\}, \qquad \forall n = m_k
\end{aligned} \tag{5.10}$$

The solution of the Ritz coefficients for subsystem k can now be stated as a bilinear

function according to equation (5.11) , with $B_k(\cdot,\cdot)$, $C_{kj}(\cdot,\cdot)$ and $l_{kj}(\cdot)$ given by (5.12).

$$\sum_{n=1}^{N}[B_k(\phi_n,\phi_{m_k})r_{k,n}+\sum_{j\in\mathcal{S}}C_{kj}(\phi_n,\phi_{m_k})r_{j,n}]=\sum_{j\in\mathcal{S}}l_{kj}(\phi_{m_k}),\qquad \forall m_k\in\{1,...,N\},\qquad \forall k\in\mathcal{S} \tag{5.11}$$

$$B_k(\phi_n,\phi_{m_k}):=\begin{cases}0, & \text{if } n\neq m_k\\ \left(\frac{(2n-1)\pi}{2L}\right)^2, & \text{if } n=m_k\end{cases} \tag{5.12a}$$

$$C_{kj}(\phi_n,\phi_{m_k}):=\begin{cases}0, & \text{if } n\neq m_k\\ \gamma_{kj}(s), & \text{if } n=m_k\end{cases} \tag{5.12b}$$

$$l_{kj}(\phi_{m_k}):=\frac{4\gamma_{kj}(s)}{(2m_k-1)\pi}\left(V_j(L)(-1)^{m_k}+\frac{2L}{(2m_k-1)\pi}\sum_{\eta\in\mathcal{S}}y_{j\eta}(s)P_\eta(0)\right) \tag{5.12c}$$

The system of equations (5.11) is linear in the adjustable parameters $r_{k,n}$ and $r_{j,n}$; therefore the n'th Ritz coefficients can be found by solving a linear matrix equation for all $k\in\mathcal{S}$ simultaneously. Define $r_n:=[r_{i,n},r_{a,n},r_{p,n}]^\top$, then the system of equations (5.11) can be rewritten as a matrix equation for $n=m_k$ given by (5.13), where $\Theta(s)$ is defined in equation (5.14).

$$\left(\left(\frac{(2n-1)\pi}{2L}\right)^2 I+\Gamma(s)\right)r_n=\Theta(s) \tag{5.13}$$

$$\Theta(s):=\frac{4}{(2n-1)\pi}\Gamma(s)V(L)(-1)^n+\frac{8L}{(2n-1)^2\pi^2}\Gamma(s)Y(s)P(0) \tag{5.14}$$

The system of equations (5.7a) can now be written on vector form. Let $\widetilde{V}:=[\widetilde{V}_i,\widetilde{V}_a,\widetilde{V}_p]^\top$, then the system (5.7a) on matrix form is given by equation (5.15). To obtain a function for the approximate pressure $\widetilde{P}:=[\widetilde{P}_i,\widetilde{P}_a,\widetilde{P}_p]^\top$ equation (5.15) is differentiated with respect to x and inserted into equation (3.37) giving equation (5.16).

$$\widetilde{V}(x)=V(L)+(x-L)Y(s)P(0)+\sum_{n=1}^{N}r_n\cos\left(\frac{(2n-1)\pi}{2L}x\right) \tag{5.15}$$

$$\widetilde{P}(x)=P(0)+Y(s)^{-1}\sum_{n=1}^{N}\left(\frac{(2n-1)\pi}{2L}x\right)r_n\sin\left(\frac{(2n-1)\pi}{2L}x\right) \tag{5.16}$$

5.4 Polynomial Approximation

In order to simulate the transfer functions given by the Ritz approximations (5.15) and (5.16) in the time domain, their inverse Laplace transforms has to be obtained. In this

section a model reduction scheme based on a series expansion using Laguerre functions is presented.

In the article Amghayrir et al. (2005) the Laguerre series representation was used to derive a model reduction technique using a transfer function formalism. The method allowed for reducing irrational transfer functions to rational approximations, minimizing the error in the least square sense. By obtaining rational transfer functions, the system can be implemented using standard state space realizations. The method in Amghayrir et al. (2005) was applied to an irrational transfer funciton in Mahdianfar et al. (2012), providing excellent results. The method was also used with some success in Anfinsen (2013).

An issue not addressed by the method in Amghayrir et al. (2005) is finding the Laguerre spectrum of the function to be approximated. In the master thesis Anfinsen (2013) a method for approximating this spectrum using the knowledge of the functions Laplace transform was developed. The algorithm developed in Amghayrir et al. (2005), with additions from Anfinsen (2013) is stated in the next subsection.

It should be noted that a multiple input, multiple output extension of the algorithm presentet below is presented in Amghayrir et al. (2005). This extension was tested and did not provide any good results, and will therefore not be considered in this report.

5.4.1 Laguerre-Gram Based Model Order Reduction

The algorithm takes the following inputs:

1. A desired order r for the rational approximation.
2. A number of sample points N for determination of the truncated Laguerre spectrum.
3. A weight parameter $\sigma \in [0, \infty]$.
4. The transfer function to be approximated F.

The rational approxmation $\hat{F}$ of F is obtained by the following steps:

1. Find the parameters, α and γ. The minimizer of the error function (5.17) gives α, where $\hat{q}_n$ is the truncated Laguerre spectrum given by equation (5.25).

$$G_\epsilon(\alpha) = \frac{\sum_{n=0}^{N} n\hat{q}_n^2(\alpha)}{\sum_{n=0}^{N} \hat{q}_n^2(\alpha)} \tag{5.17}$$

   γ is found by solving equation (5.18).

$$\gamma = \sigma + 2\alpha \tag{5.18}$$

2. Calculate the Laguerre spectrum $\hat{q}_n$ using equation (5.25) with α and γ.
3. Form the Gram matrix defined in equation (5.19), and the vector (5.20).

$$\Psi := \begin{bmatrix} \psi_{0,0} & \psi_{0,1} & \cdots & \psi_{0,r-1} \\ \psi_{1,0} & \psi_{1,1} & \cdots & \psi_{1,r-1} \\ \vdots & \vdots & \ddots & \vdots \\ \psi_{r-1,0} & \psi_{r-1,1} & \cdots & \psi_{r-1,r-1} \end{bmatrix} \tag{5.19}$$

$$b := \begin{bmatrix} \psi_{0,r} & \psi_{1,r} & \dots & \psi_{r-1,r} \end{bmatrix}^\top \tag{5.20}$$

The coefficient $\psi_{i,j}$ are computed according to equation (5.21), using the Laguerre spectrum.

$$\psi_{i,j} = \sum_{n=0}^{N} \hat{q}_{n+i}\hat{q}_{n+j} \tag{5.21}$$

4. Solve the system of equations (5.22) for the vector of coefficients (5.23).

$$\Psi a = -b \tag{5.22}$$

$$a := \begin{bmatrix} a_0 & a_1 & \dots & a_{r-1} \end{bmatrix}^\top \tag{5.23}$$

5. Form the reduced order model (5.24), where $a_r := 1$.

$$\hat{f}(s) = \frac{\sqrt{\gamma}\sum_{i=1}^{r} a_i \sum_{j=0}^{i-1} \hat{q}_j (s+\alpha)^{i-j-1}(s-\gamma+\alpha)^{r-i+j}}{\sum_{i=0}^{r} a_i (s+\alpha)^i (s-\gamma+\alpha)^{r-i}} \tag{5.24}$$

For derivations and proofs the reader is referred to Amghayrir et al. (2005) and Anfinsen (2013).

Note that the computational speed needed for calculating $\psi_{i,j}$ can be drastically reduced using its recursion and symmetry properties. Namely that $\psi_{i,j} = \psi_{i-1,j-1} - \hat{q}_{i-1}\hat{q}_{j-1}$ for $i = 1, 2, \dots, r-1$ and $j = i, i+1, \dots, r$, and that $\psi_{i,j} = \psi_{j,i}$.

The truncated Laguerre spectrum developed in Anfinsen (2013) is stated in equation (5.25), where the function $G(\theta)$ is given by equation (5.26). Note that $\{\hat{q}_n(\alpha,\gamma)\}_{0\leq n\leq N}$ can be recognized as a shifted and scaled version of the *discrete Fourier transform* og $G(\theta)$, and the *fast Fourier transform* can be applied (Kreyszig (2005)).

$$\hat{q}_n(\alpha,\gamma) = \frac{e^{-j\pi\frac{n}{2N}}}{2N} \sum_{k=-n}^{N-1} G\left(\frac{\pi}{2}(k+\frac{1}{2})\right) e^{-j\pi\frac{nk}{N}} \tag{5.25}$$

$$G(\theta) := \frac{\sqrt{\gamma}}{1-e^{j\theta}} F\left(\frac{\gamma}{1-e^{j\theta}} - \alpha\right) \tag{5.26}$$

Chapter 6

Frequency Analysis

6.1 Introduction

In this chapter the Ritz approximations (5.15) and (5.16), and the rational approximations found using the previously stated Laguerre Gram model order reduction algorithm, will be compared to the analytical frequency domain solution (3.42).

There are six inputs and six outputs to the transmission line stated in chapter 3, resulting in 36 unique transfer functions. To obtain the analytical transfer functions that correspond to the approximated ones, six constants of integration B_1, B_2,...B_6 are needed. These are found by solving equation (3.44), where the matrix D is given by equation (6.1) and the vectors b_1, b_2...b_6 are given by equation (6.2).

$$D = \begin{bmatrix} \bar{y}_1(L,s) \\ \bar{y}_2(0,s) \\ \bar{y}_3(L,s) \\ \bar{y}_4(0,s) \\ \bar{y}_5(L,s) \\ \bar{y}_6(0,s) \end{bmatrix} \tag{6.1}$$

$$b_1 = \begin{bmatrix} 1 \\ 0 \\ 0 \\ 0 \\ 0 \\ 0 \end{bmatrix} \quad b_2 = \begin{bmatrix} 0 \\ 1 \\ 0 \\ 0 \\ 0 \\ 0 \end{bmatrix} \quad b_3 = \begin{bmatrix} 0 \\ 0 \\ 1 \\ 0 \\ 0 \\ 0 \end{bmatrix} \quad b_4 = \begin{bmatrix} 0 \\ 0 \\ 0 \\ 1 \\ 0 \\ 0 \end{bmatrix} \quad b_5 = \begin{bmatrix} 0 \\ 0 \\ 0 \\ 0 \\ 1 \\ 0 \end{bmatrix} \quad b_6 = \begin{bmatrix} 0 \\ 0 \\ 0 \\ 0 \\ 0 \\ 1 \end{bmatrix} \tag{6.2}$$

Looking at figure 6.1 narrow periodically dampned resonance peaks can be observed for the transfer function $V_p(0)/V_p(L)$ and $V_i(0)/V_i(L)$, around $\omega = 1.5, 4.5, 7.5, \ldots$ rad/s. For the transfer function $V_p(0)/V_p(L)$ these peaks are due to the elastic dynamics of the pipe, it is however not necessarily expected to see similar resonances for the transfer function $V_i(0)/V_i(L)$. The same type of narrow resonance peaks can be observed with the

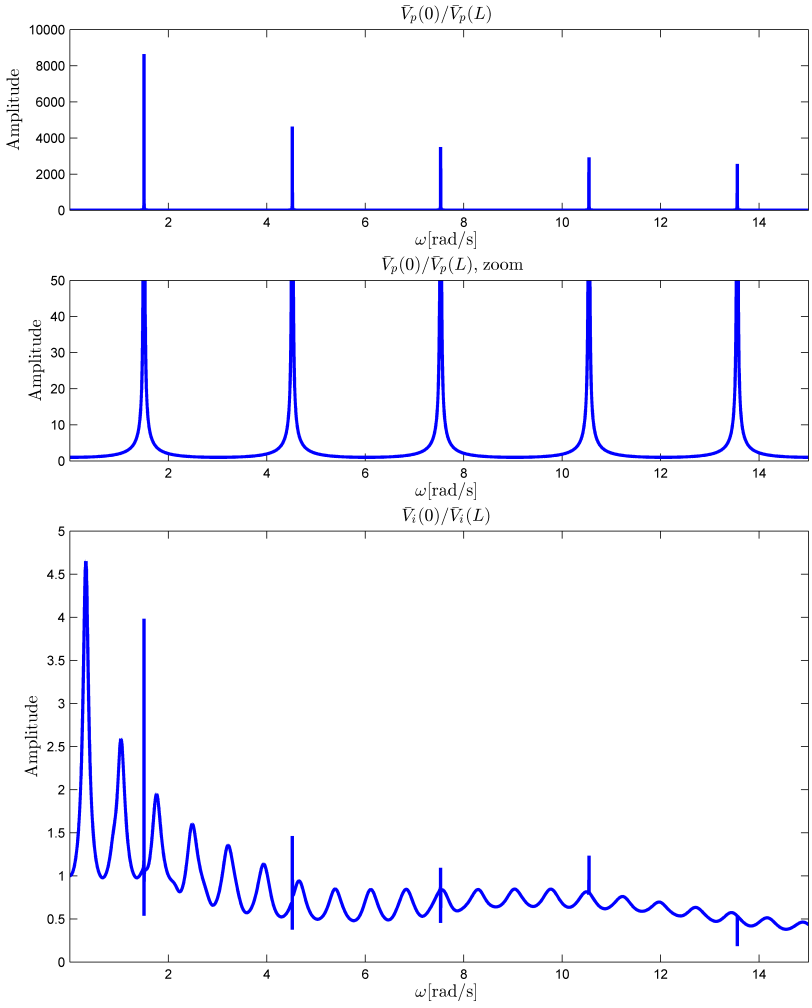

Figure 6.1: Amplitude for the analytical transfer functions $V_p(0)/V_p(L)$ and $V_i(0)/V_i(L)$.

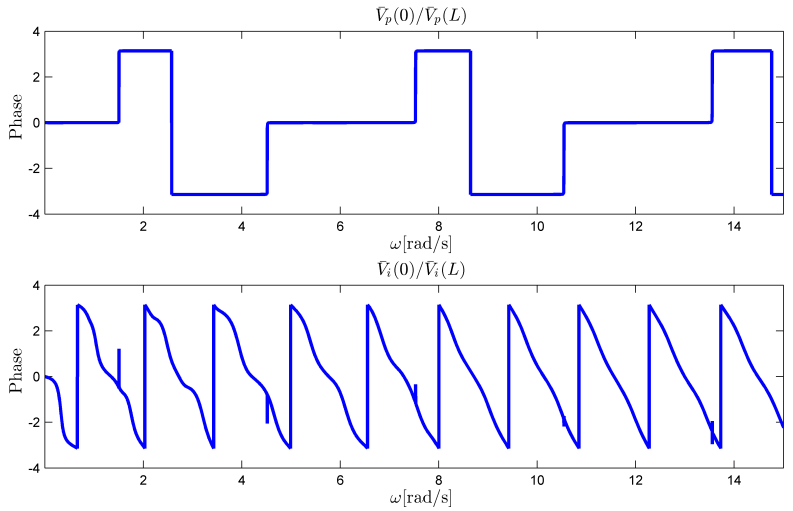

Figure 6.2: Phase for the analytical transfer functions $V_p(0)/V_p(L)$ and $V_i(0)/V_i(L)$.

same periodicity for all 36 transfer functions in appendix B. For the transfer functions from or to the pipe, these resonances are occuring due the pipe dynamics. However for the transfer functions between the mud flows, these spikes are somewhat unexpected. Zooming in on the spike around $\omega = 1.5\text{rad/s}$, shown in figure 6.3, it can be seen that the peak is smooth, suggesting that they do not occur due to numerical issues.

A closer look at the transfer functions between the mud flows reveals that the resonance spikes occur because of an indirect coupling with the pipe dynamics. When the flow velocity is averaged, reducing the model from a two dimensional model (3.8) (radial and axial) to a one dimensional model (3.11) (axial), radial boundary conditions are inserted based on the noslip condition. This radial dependency is what couples the pipe resonances into the fluid flow.

Physically these resonances are expected from the no slip condition. As the boundary layer of the fluid in contact with the pipe wall have the same velocity as the pipe wall, inducing the resonant behaviour of the pipe into the fluid. Resulting in an indirect coupling of the pipe with the mud in annulus and pipe subsystems. The mud in the annulus and the pipe are flowing in opposite directions of one another; the pipe flow downwards and the annulus flow upwards. This together with the viscous properties of the drilling mud is expected to distort and dampen these induced resonances. This can be seen by comparing the frequency response for the transfer functions $V_p(0)/V_p(L)$ and $V_i(0)/V_i(L)$ in figure 6.3.

Figure 6.2 shows the phase plots of the transfer functions $V_p(0)/V_p(L)$ and $V_i(0)/V_i(L)$. One can for the transfer function $V_p(0)/V_p(L)$ observe an oscillating phase with the same periodicity as the resonances, which is as expected. The same can be observed for $V_i(0)/V_i(L)$, however with a distortion at the same frequencies as resonance is observed

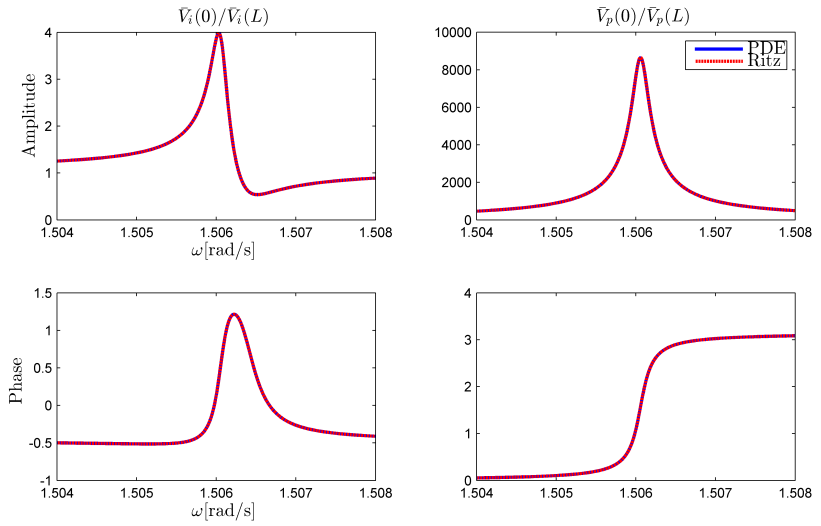

Figure 6.3: Frequency response of $V_p(0)/V_p(L)$ and $V_i(0)/V_i(L)$, at resonance around $\omega = 1.506$rad/s.

for $V_p(0)/V_p(L)$. The explanation for these distortions are of course the same as with the amplitude.

The well properties and physical parameters used to simulate all transfer functions in this chapter and appendix B, C and D are stated in table 6.1.

6.2 Ritz Approximation

In this section the frequency domain solution of the Ritz approximations (5.15) and (5.16) are compared with the analytical solution (3.42).

In figures 6.4, 6.5 and 6.6 a comparison of the analytical and the Ritz approximated transfer function $V_i(0)/V_i(L)$ can be seen, using 2, 4 and 16 modes respectively. Using 2 modes the approximation is good for frequencies below 1.2rad/s. Using 4 modes the approximation fits well up to a frequency of 2.6rad/s. Increasing the number of modes to 16 gives a very accurate fit for higher frequencies for the transfer function $V_i(0)/V_i(L)$. Looking at figure 6.3 it can be seen that the Ritz approximation also manages to catch the narrow resonant peaks around $\omega = 1.5$rad/s.

All 36 transfer functions are compared, using 16 modes, in appendix B. It can there be seen that a very accurate fit is obtained for frequencies below 1.5rad/s. Increasing the number of modes will increase accuracy of the Ritz approximation in all cases.

Table 6.1: Value of well properties and physical parameters

Constant	Value	Unit	Description
$\bar{A}_a$	0.0274	m^2	Nominal annulus flow area
$\bar{A}_i$	0.0118	m^2	Nominal pipe flow area
A_p	0.0030	m^2	Pipe cross-sectional area
L	5000	m	Length of drill string
β	2.2×10^9	Pa	Drilling mud bulk modulus
$\bar{\beta}_i$	1.84×10^9	Pa	Pipe effective bulk modulus
$\bar{\beta}_a$	1.60×10^9	Pa	Annulus effective bulk modulus
$\frac{1}{\bar{A}_i}\frac{\partial A_i}{\partial p_a}$	-9.67×10^{-11}	$1/\mathrm{Pa}$	Pipe area change coefficient
$\frac{1}{\bar{A}_a}\frac{\partial A_a}{\partial p_i}$	-4.18×10^{-11}	$1/\mathrm{Pa}$	Pipe area change coefficient
ρ	1420	$\mathrm{kg/m}^3$	Drilling mud density
ρ_p	9000	$\mathrm{kg/m}^3$	Pipe density
E	2.068×10^{11}	Pa	Pipe Young's modulus
ν	3.00×10^{-5}	m^2/s	Kinematic viscosity
k_p	0.0950	$1/\mathrm{s}$	Pipe damping coefficient
f_a	1.45×10^{-12}	$1/\mathrm{Pa}$	Annulus flow hoop-strain coefficient
f_i	1.45×10^{-12}	$1/\mathrm{Pa}$	Pipe flow hoop-strain coefficient

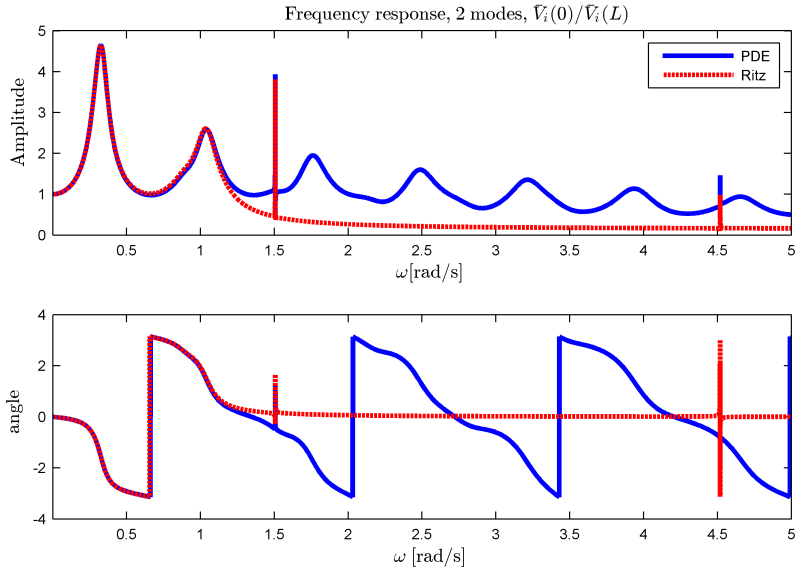

Figure 6.4: Analytical and Ritz approximation frequency response for $\bar{V}_i(0)/\bar{V}_i(L)$, using 2 modes

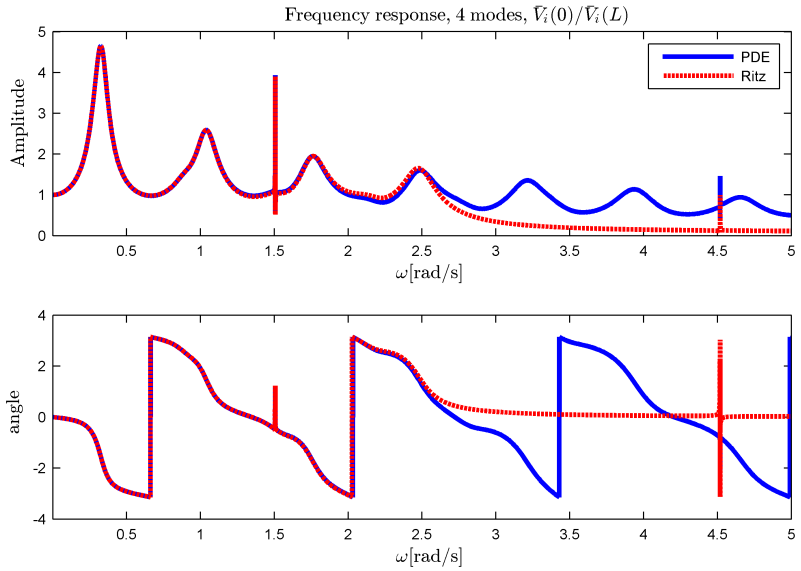

Figure 6.5: Analytical and Ritz approximation frequency response for $\bar{V}_i(0)/\bar{V}_i(L)$, using 4 modes

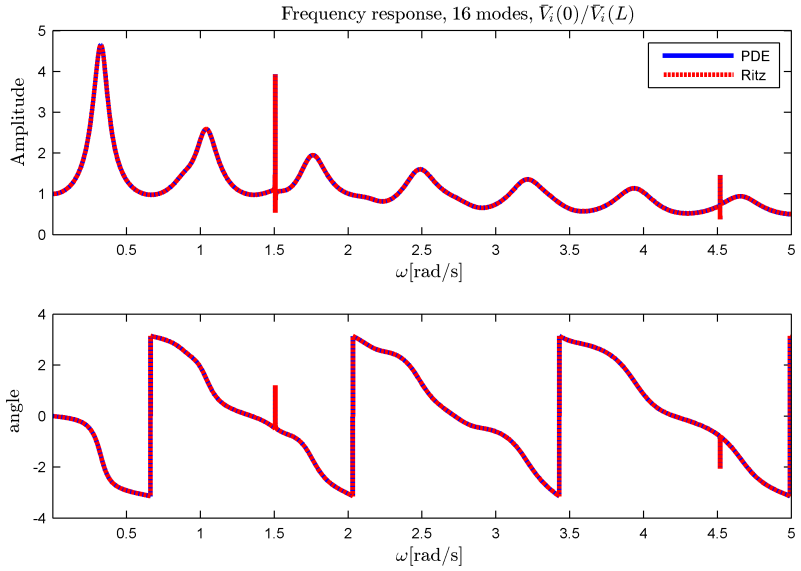

Figure 6.6: Analytical and Ritz approximation frequency response for $\bar{V}_i(0)/\bar{V}_i(L)$, using 16 modes

6.3 Rational Approximation

In this section rational approximations of the transmission line stated in chapter 3, obtained using the Laguerre-Gram method, is compared with the analytical frequency solution (3.42). Some cases are considered in detail here, while all 36 frequency responses are plotted in appendix C using $N = 1500$, $\sigma = 0$ and $r = 64$ as inputs to the Laguerre-Gram method, and appendix D using $N = 1500$, $\sigma = 0.01$ and $r = 64$.

Note that all rational approximations are found by sampling the Ritz approximation, using 32 modes. Furthermore, all transfer functions are approximated individually, which will lead nonminimal state space realizations.

6.3.1 Case 1: Order of Rational Approximation

Figures 6.7, 6.8 and 6.9 show the frequency response of the transfer function $V_i(0)/V_i(L)$ found using order $r = 32$, $r = 96$ and $r = 128$ for the rational approximation respectively. $N = 1500$ sampling points where used and $\sigma = 0$ as weighting parameter.

Figure 6.7 shows that the Laguerre-Gram gives a good approximation in both amplitude and phase for frequencies below $\omega = 3\text{rad/s}$. However it fails to capture the spike around $\omega = 1.5\text{rad/s}$. The method is however not expected to capture these spikes without using either a very high polynomial order.

Comparing the frequency reponse in figure 6.7 and 6.8 it can be seen that by increasing the order of the rational approximation from $r = 32$ to $r = 96$ its accuracy is raised. However it still fails to capture the resonance spikes, although it is better captured compared to the lower order.

Figure 6.9 shows the frequency response of the transfer function $V_i(0)/V_i(L)$ using a rational approximation of order $r = 128$, which fails horribly for frequencies from about $\omega = 0.4\text{rad/s}$ to $\omega = 2.2\text{rad/s}$. However a good fit is obtained for frequencies from $\omega = 2.2\text{rad/s}$ up to $\omega = 6\text{rad/s}$. One would expect that a higher degree for the rational approximation would give a better approximation in the entire frequency domain. One possible reason for the failure of the method when the order of the approximation is set to high, might be that the number of sample points N is to low. However this is difficult to test, because when N is increased beyond a certian point (around $N = 4400$) the problem becomes numerically singular.

Looking at the poles and zeros for the different approximations, shown in figure 6.10, one can see that one of the poles is placed further and further into the left half plane when increasing the order. It is a well know problem that sparsly spread poles may lead to numerical issues, and making the state-space realization numerically stiff (e.g. Egeland and Gravdahl (2002)). This is however probably not the source of the failure of the Laguerre-Gram method for high order approximation. A closer look at the poles of the rational approximation of order $r = 128$ reveal that some of the poles have a positive real part, making the approximated subsystem unstable. This is probably neither the source of the failure of the Laguerre-Gram method, as other approximated subsystems have unstable poles without a similar deficiency in the frequency response.

A closer look at the poles and zeros of the different order rational approximations reveal that many poles lie close to zeros. This might be a reason for the failure of the highest order approximations, as these poles and zeros would analytically cancel each other out

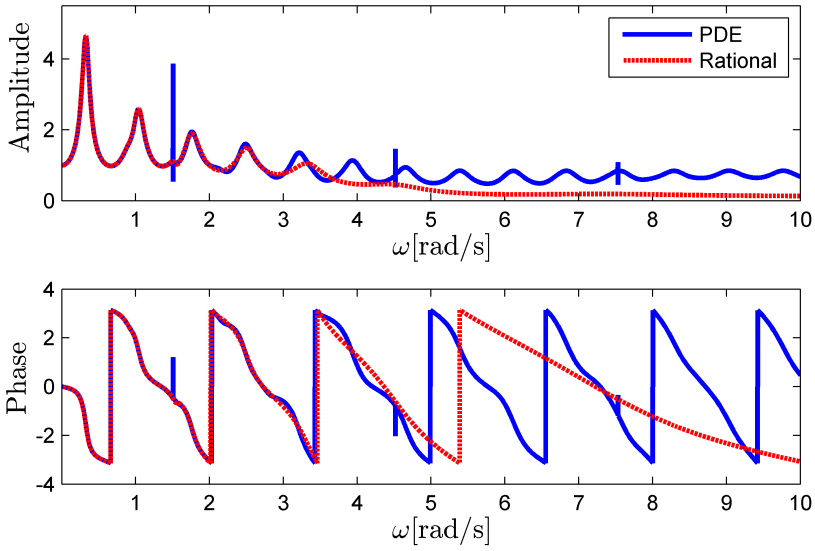

Figure 6.7: Frequency response PDE vs. rational approximation, $V_i(0)/V_i(L)$, $r = 32$, $\sigma = 0$.

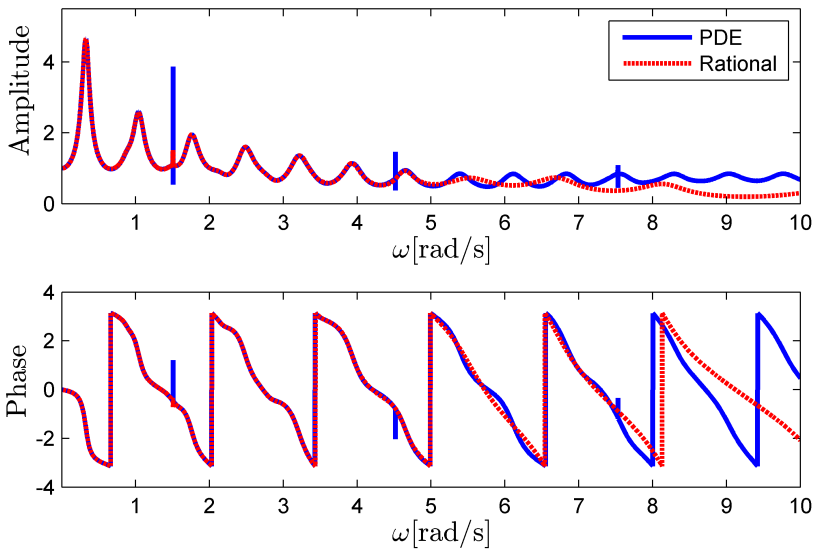

Figure 6.8: Frequency response PDE vs. rational approximation, $V_i(0)/V_i(L)$, $r = 96$, $\sigma = 0$.

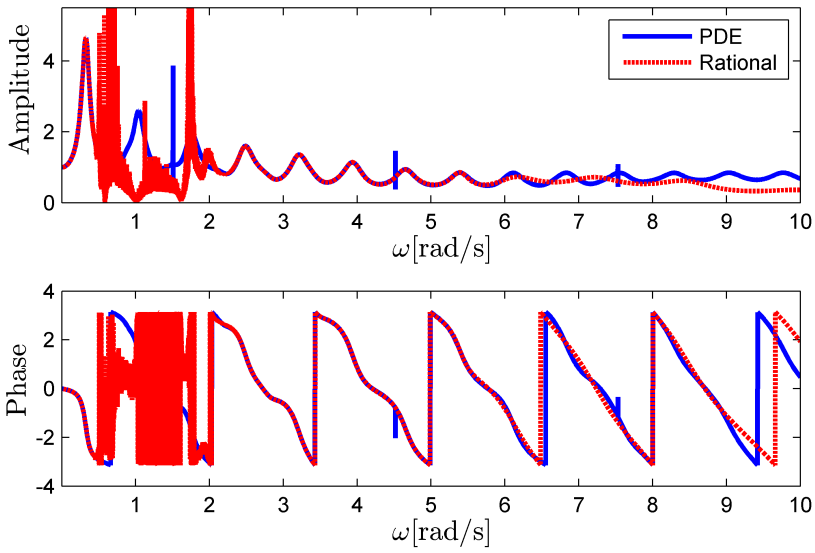

Figure 6.9: Frequency response PDE vs. rational approximation, $V_i(0)/V_i(L)$, $r = 128$, $\sigma = 0$.

but numerical issues place them appart. However all of the rational approximations contain poles and zeros placed closely, so this seems unlikely.

6.3.2 Case 2: Different Weights

In appendix C it can be seen that using $\sigma = 0$ as the weight parameter, does not result in a good rational approximation in all cases. Figure 6.11 shows the percentile error between the rational approximation obtained using the Laguerre-Gram method and the analytical solution of the transfer function $P_p(L)/V_i(L)$ for $\sigma = 0, 0.007, 0.01, 0.2$. Figures 6.12 and 6.13 shows the corresponding phase plots, and poles and zeros. These plots show that the accuracy of the rational approximation can be drastically increased by picking the correct σ, and that some of the relevant transfer functions are very sensitive to this parameter. In the case presented here $\sigma = 0.01$ gives the best approximation, with an accurate frequency domain from $\omega = 0.4\text{rad/s}$ to $\omega = 1.6\text{rad/s}$. As $\omega \to 0$ the amplitude $|P_p(L)/V_i(L)| \to 0$ for the analytical transfer function, which is not the case for the rational approximation. This will lead to a steady state error.

Looking at the poles of this rational approximation, reveals that some of the poles are unstable; making the approximation unstable. This instability is contradicting the stable nature of the physical system, making the validity of the approximation dubious. It should also be noted that the approximation of this subsytem will be stiff, as the poles are widely spread.

The results presented in this subsection are also valid for the other subsytems of the

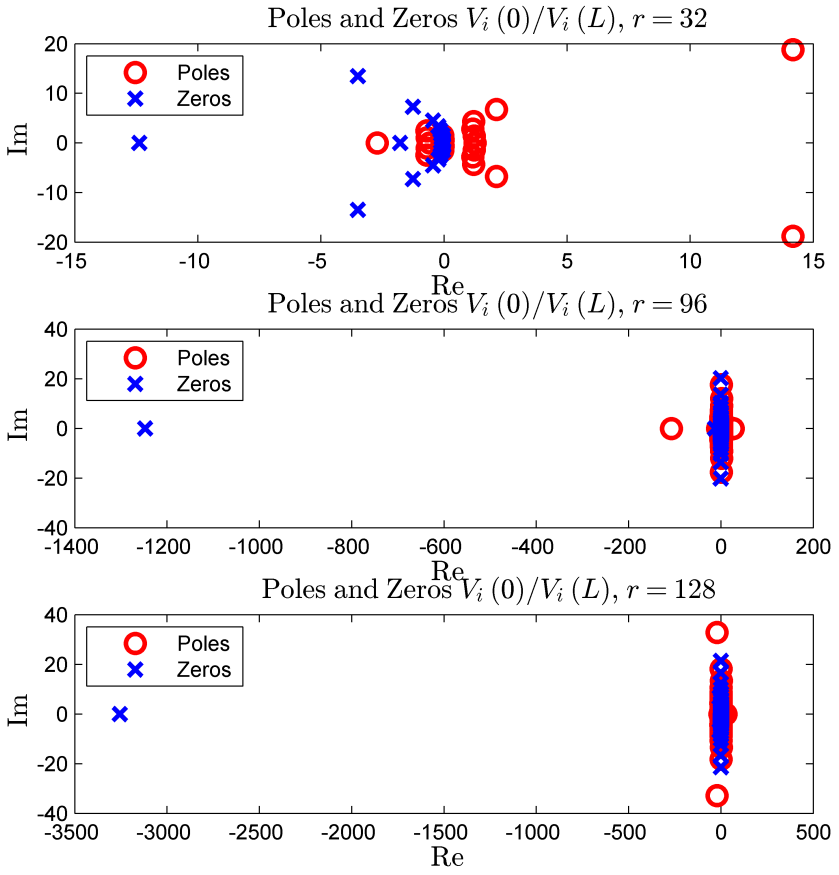

Figure 6.10: Poles and zeros for the rational approximations of $V_i(0)/V_i(L)$.

transmission line. Appendix D shows the frequency response for every subsystem, using $N = 1500$, $r = 64$ and $\sigma = 0.01$.

6.3.3 Case 3: Number of Sampling Points

To test the sensitivity of the Laguerre-Gram method with respect to the number of sampling points, the transfer function $P_p(L)/V_i(L)$ is considered. The reason for using this transfer function is that it was tested to be one of the more sensitive transfer functions with respect to the number of sampling points.

Figure 6.14 show the percentile error of between the analytical amplitude and its rational approximation for the transfer function $P_p(L)/V_i(L)$, using $N = 200, 1500, 4000$ sampling points and order $r = 64$ and weight $\sigma = 0.01$; figure 6.15 shows the corresponding phase. It can be seen that if the number of sampling points is to low, the approximation fails to capture any of the systems dynamics. Increasing the number of sampling points from $N = 200$ to $N = 1500$ reduce the error drastically, giving a valid frequency range from $\omega = 0.4\text{rad/s}$ to $\omega = 1.6\text{rad/s}$. However it can also be seen that increasing the number of sampling points more, decrease the accuracy of the approximation for lower frequencies, and increase the accuracy in the range $\omega = 3.2\text{rad/s}$ to $\omega = 4\text{rad/s}$. Further adding sampling points above around $N = 4400$ result in a numerical instability, and the Laguerre-Gram method fails.

6.4 Numerical Issues

From the cases presented in the previous section it can be seen that the Laguerre-Gram method can give good approximations for frequencies from around $\omega = 0.4\text{rad/s}$ to $\omega = 1.6\text{rad/s}$, if correct order r, number of sampling points N and weight σ is picked. It can also be seen that by picking any of these values either to low or to high results in failure. It is expected that when using either to few sampling points or a low order the method would fail. This is however not expected when they are picked to big. One likely reason for this failure is that the Hankel functions of the second kind diverge, e.g. $H_1^{(2)} \to \infty$ when $s \to \infty$. Which for high order approximations or a large number of sampling points may lead to numerical instabilities when using conventional tools. This problem was clearly observed when picking N to big, as the numerical problem became singular, while it can from the plots be clearly seen that none of analytical transfer functions diverge.

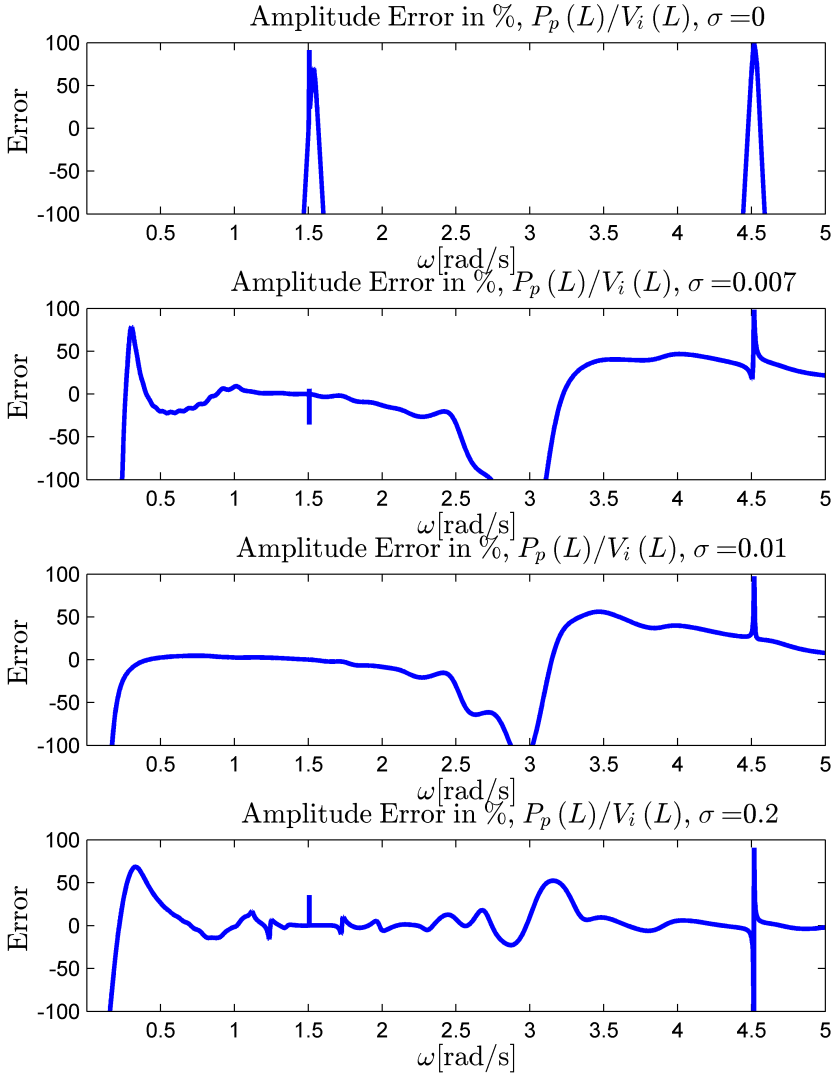

Figure 6.11: Percentile error in amplitude between rational approximation and analytical solution of $P_p(L)/V_i(L)$, for different σ, $N = 1500$, $r = 64$.

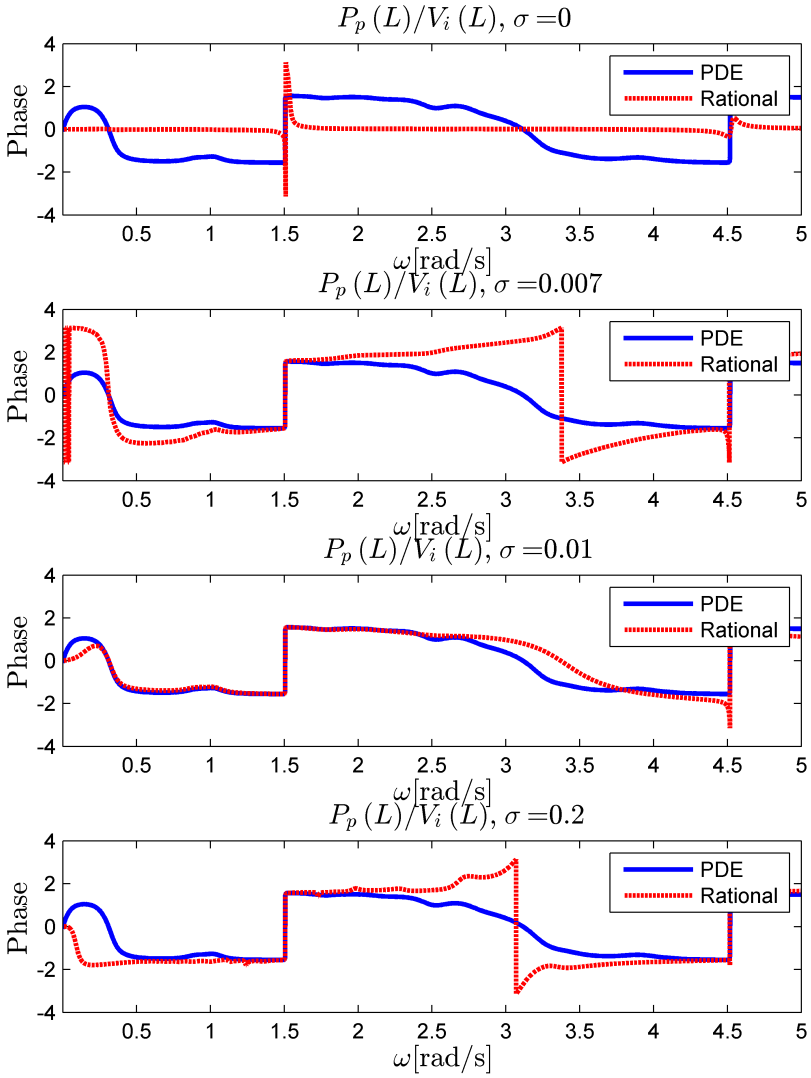

Figure 6.12: Phase of $P_p(L)/V_i(L)$, for different σ, $N = 1500$, $r = 64$.

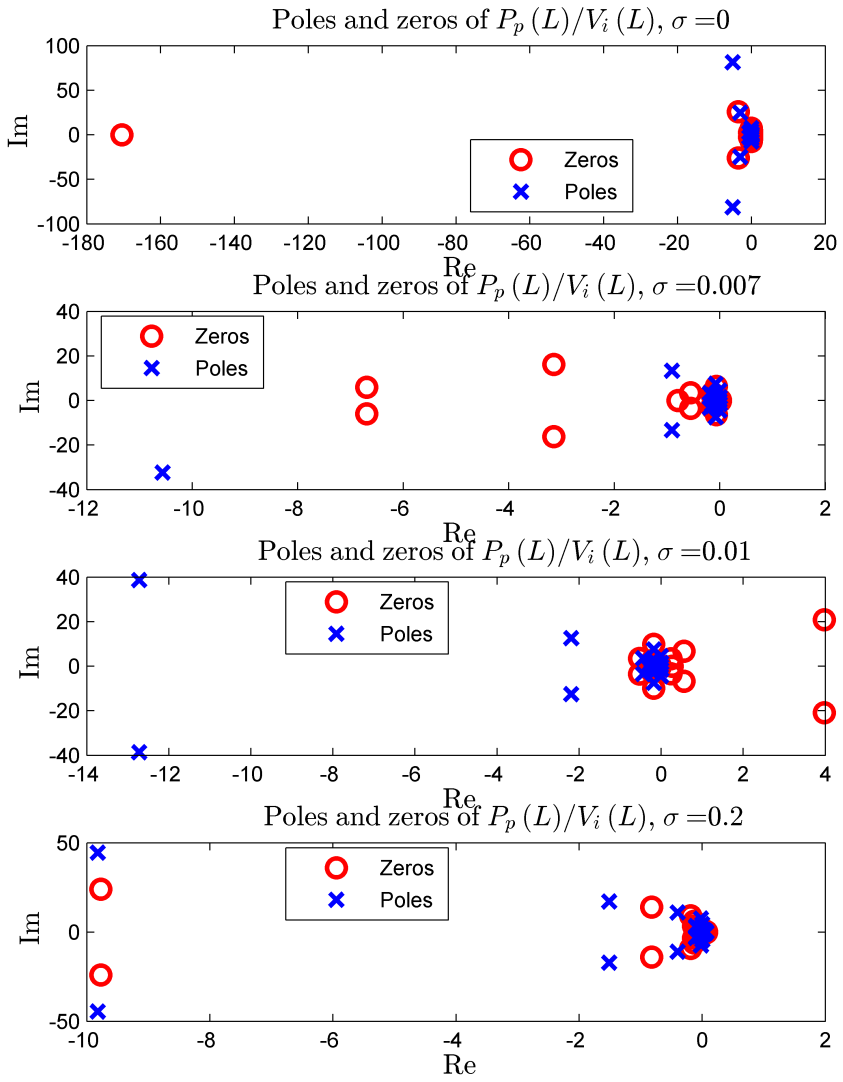

Figure 6.13: Poles and zeros of $P_p(L)/V_i(L)$, for different σ, $N = 1500$, $r = 64$.

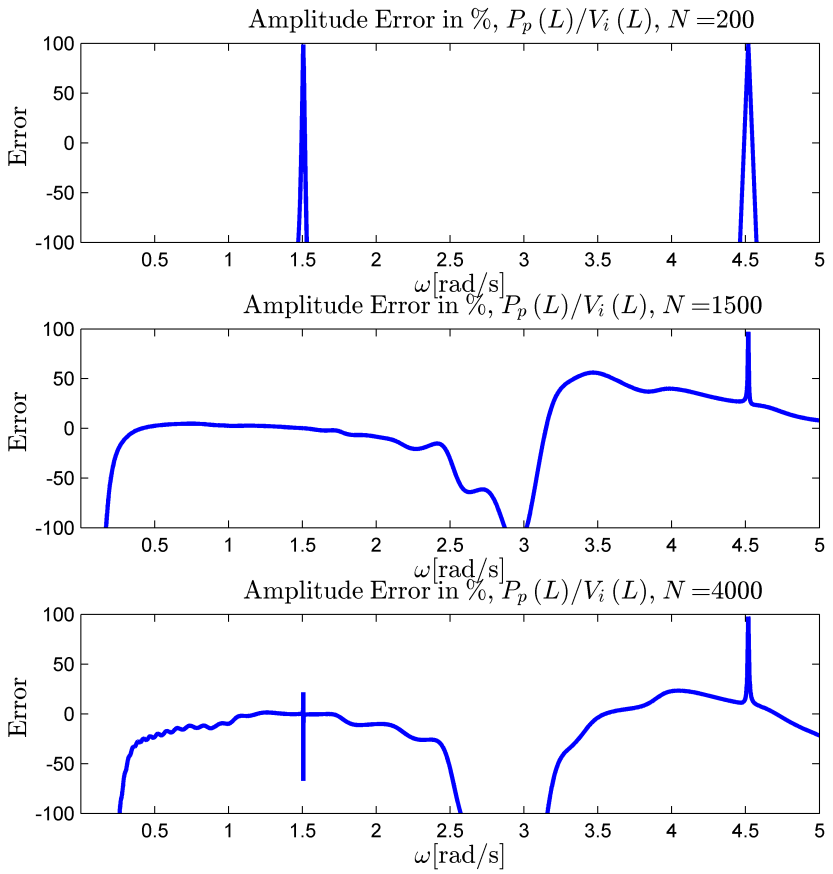

Figure 6.14: Percentile error in amplitude between rational approximation and analytical solution of $P_p(L)/V_i(L)$, for different N, $\sigma = 0.01$, $r = 64$.

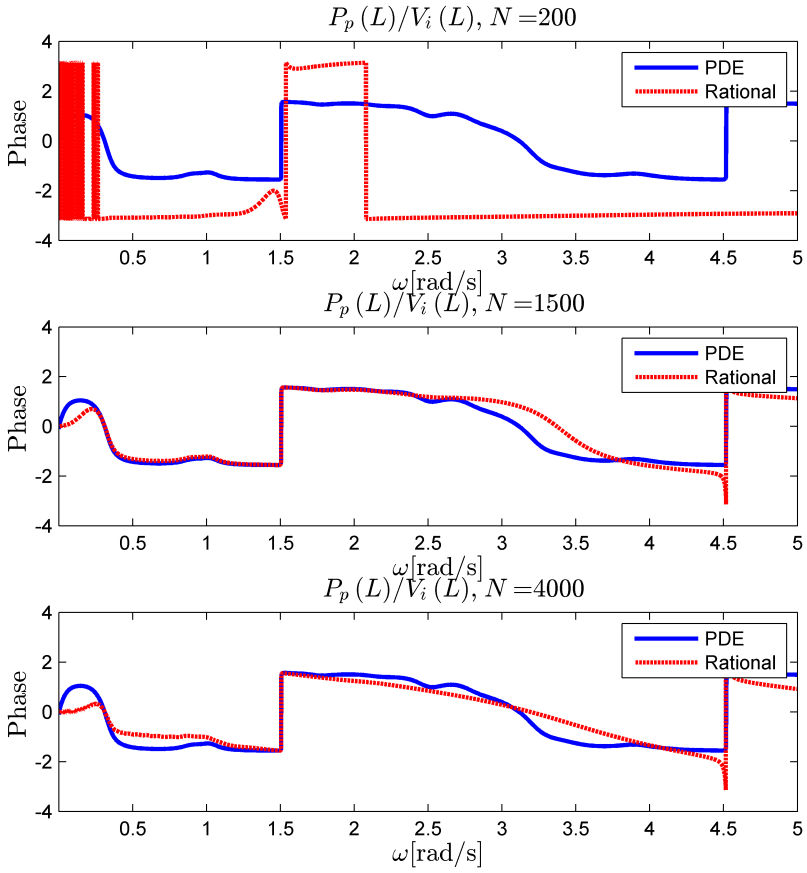

Figure 6.15: Phase of $P_p(L)/V_i(L)$, for different N, $\sigma = 0.01$, $r = 64$.

Chapter 7

Discussion

The main objective of this thesis was to construct a time domain simulator for the coupled hydraulic transmission line presented in chapter 3, with an added model for downhole pressure and boundary conditions representing a continuous circulation system. This goal was not achieved. The reason for this is that there are still some numerical issues to be solved regarding the rational approximation of the irrational transfer functions giving the hydraulic transmission line.

A Ritz approximation was applied with great success to the coupled hydraulic transmission line. The irrational transfer functions obtained using this method were then approximated as rational transfer function using the Laguerre-Gram model order reduction method present Amghayrir et al. (2005) with the extensions given by Anfinsen (2013). Using this method some issues were encountered. As mentioned in chapter 6 some numerical issues arise when many sampling points are used, because the Hankel functions of the second kind diverge when the Laplace operator $s \to \infty$. Leading to a mix of very big and very small numbers, which is a well known numerical problem. This might very well be what cause failure when a high rational order is used for the approximation.

Another issue with the approximations obtained with the Laguerre-Gram method is that in many cases poles where placed in the right half plane, making it unstable. This instability is contradicting the original system, which is stable. Therefore the Laguerre-Gram method as presented is not in general a good way to approximate this system. However the unstable poles were not observed before the order of the approximation or the number of sampling points were increased beyond a certain point. Suggesting that they might arrise due to the same numerical issues discussed above.

A floating rig will in general be subject to heave motion induced by oceanic waves, and MPD operations are usually only done in relatively calm sea states. Furthermore because of the massive size of drilling rigs waves must contain a certain amount of energy before they actually will induce any relevant heave motion. Meaning that the rational approximations only need to be accurate for a relatively small frequency range. Because of the nature of oceanic waves this frequency range will vary with geography, but will in general be at the lower end of the scale. Therefore the method presented in this thesis

can for some practical cases provide a rational approximation of the irrational hydraulic transmission line that is fit for purpose.

A set of boundary conditions and a downhole pressure node has also been presented, however because the time domain simulator were not finished validation/disqualification of these could not be done. The topside boundaries are all easily definable model inputs with natural physical interpretations, and should therefore not constitute any problems. The pressure drop over the drill bit nozzel should be relatively accurate as it is well established in the litterature. The momentum balance should also hold, assuming all major moments affecting the bit have been thought of. What is more uncertain is the validity of the downhole pressure node and the annulus flow boundary condition. The internal flow model presented for the annulus boundary is probably not very useful in practice, as good numerical values will be difficult to obtain.

Chapter 8

Conclusion and Further Work

8.1 Conclusion

In this master thesis a Ritz approximation was developed to disecretize a piston like hydraulic transmission line, using Robin boundary conditions. The pipe and annulus flow was modeled using a two-dimensional viscous compressible model, and coupled through the moving pipe modeled as an elastic rod. Laplace transforming this transmission line allowed for averaging away the radial dynamics. The Laguerre-Gram model order reduction method was applied to the Ritz approximation in order to obtain rational transfer functions.

Frequency analysis indicated that the Ritz approximation provide an excellent discretization scheme for this particular problem. Similar analysis suggested that the Laguerre-Gram method is, for the considered problem, very sensitive to its input parameters, and are subject to numerical issues. The placement of the poles of the rational approximation were also in some cases shown to be unstable, in conradiction with the original system. It was also argued that for some cases the method would most likely be able to provide a fit for purpose model, in spite of the mentioned issues.

A set of Robin boundary conditions were stated, aswell as a downhole pressure node developed using the definition of bulk-modulus. This pressure node was added to serve as and interconnection between the downhole transmission line inputs and outputs, and to test if such a model will improve the accuracy compared to the physical system. Three different annulus flow boundaries were suggested, of which the first is the linear and the second the quadratic valve equation, and the last one was based on internal flow. Due to the complexity of the internal flow model, the other two models will most likely provide better results without investing a lot of time into tuning.

8.2 Further Work

The most obvious remaining work is to tune the inputs to the Laguerre-Gram method and obtain a set of rational transfer functions, in order to perform simulations in the time do-

main. Doing this will allow for testing the validity of the proposed boundary conditions and downhole pressure node. It would be interesting to compare the then obtained model with actual data. The effect of using the different proposed annulus flow boundary conditions should also tested, aswell as their parameter sensitivity.

The multiple input, multiple output extension for the Laguerre-Gram model order reduction method should be investigated, in order to obtain minimal state space realizations. The numerical robustness of this method should also be persued. This includes, but is not limited to:

- Stating the transmission line using Bessel functions as a basis, instead of Hankel functions, to see if this improves numerical stability.
- Testing different forms of the weight parameter σ for the Laguerre-Gram method.
- Forcing unstable poles to become stable. An idea here is to investigate the possibility of forcing passivity.

Other methods to obtain rational approximations than the Laguerre-Gram model order reduction scheme should also be investigated.

Bibliography

Aarsnes, U. J. F., Aamo, O. M., Hauge, E., Pavlov, A., 2013. Limits of controller performance in the heave disturbance attenuation problem. In: Proc. European Control Conference. Zürich, Switzerland, pp. 1071–1076.

Aarsnes, U. J. F., Aamo, O. M., Pavlov, A., 2012. Quantifying error introduced by finite order discretization of a hydraulic well model. In: Australian Control Conferance. Sydney, Australia, pp. 54–59.

Aarsnes, U. J. F., Gleditsch, M. S., Aamo, O. M., Pavlov, A., 2014. Modeling and avoidance of heave-induced resonances in offshore drilling. SPE Drilling & Completion 29 (04), 454–464.

Amghayrir, A., N., T., P., B., Vilbé, P., Calvez, L. C., 2005. Laguerre-gram reduced-order modeling. IEEE Transactions on Automatic Control 50 (9), 1432–1435.

Anfinsen, H., 2013. Disturbance attenuation in linear 2x2 hyperbolic systems.

Burkhardt, J. A., 1961. Wellbore pressure surges produced by pipe movement. Petroleum Engineering 13 (6), 595–605.

Cengel, Y. A., Cimbala, J. M., 2010. Fluid Mechanics: Fundamentals and Applications, 2nd Edition. McGraw-Hill Higher Education.

Chung, J., Whitney, A., 1981. Dynamic vertical stretching oscillation of an 18,000ft ocean mining pipe. In: Offshore Technology Conference. Huoston, Texas.

Deveraux, S., 2012. Drilling Technology in Nontechnical Language, 2nd Edition. Penn Well.

Egeland, O., Gravdahl, J. T., 2002. Modeling and Simulation for Automatic Control. Marine Cybernetics AS.

Fossen, T. I., 2011. Handbook of Marine Craft Hydrodynamics and Motion Control. John Wiley & Sons, Ltd.

Godhavn, J. M., 2010. Control requirements for automatic managed pressure drilling. SPE Drililng & Completion 25 (3), 336–345.

Greenfield, W., Lubinski, A., 1967. Use of bumper subs when drilling from floating vessels. Journal of Petroleum Engineers 19 (12), 1587–1594.

Hsue, C., Hullender, D., 1983. Modal approximations for the fluid dynamics of hydraulic and pneumatic transmission lines. Fluid Transmission Line Dynamics, 51–77.

Hullender, D., Woods, R., Hsue, C., 1988. Time domain simulations of transmission lines using minimum order state variable models. Fluid Transmission Line Dynamics, 78–97.

Jenner, J. W., Elkins, H., Springett, F., Lurie, P. G., Wellings, J. S., 2005. The continuous-circulation system: An advance on constant-pressure drilling. SPE Drilling & Completion 20 (03), 168–178.

Kaasa, G., Stamnes, O., 2011. Intelligent estimation of downhole pressure using simplified hydraulic model. In: IADC/SPE Managed Pressure Drilling and Underbalanced Operations Conference and Exhibition. Denver, Colorado.

Kreyszig, E., 2005. Advanced Engineering Mathematics, 9th Edition. John Wiley & Sons.

Landet, I. S., Mahdianfar, H., F., A. U. J., Pavloc, A., Aamo, O. M., 2012. Modeling for mpd operations with experimental validation. In: IADC/SPE Drilling Conference and Exhibition. San Diego, California.

Mahdianfar, H., Aamo, O. M., Pavlov, A., 2012. Suppresion of heave-induced pressure fluctuations in mpd. In: Proceedings of the 2012 American Control Conference.

Martin, M. D., 2006. Managed pressure drilling techniques and tools.

McAndrews, K. L., 2011. Consequenses of macondo: A summary of recently proposed and enacted changes to us offshore drilling safety and environmental regulation. SPE Americas E&P Health, Safety, Security and Environmental Conference.

Miller, J., Young, R., 1985. Influence of mud column dynamics on top tension of suspended deepwater drilling risers. In: Offshore Technology Conference. Houston, Texas.

Mitchell, R. F., 1988. Dynamic surge/swab pressure predictions. SPE Drilling Engineering 3 (03), 325–333.

Mitchell, R. F., 2004. Surge pressures in low-clearance lines. In: IADC/SPE Drilling Conference. Dallas, Texas.

Mäkinen, J., Piché, R., Ellman, A., 2000. Fluid transmission line modeling using a variational method. Journal of Dynamic Systems, Measurment and Control 122 (1), 153–162.

Namba, Y., Uto, S., Nimura, T., 2010. Experiments for modeling internal fluid effect on hung-off rigid riser under axial motion. Offshore Polar 20 (1), 7–14.

Niedzwecki, J., Thampi, S., 1988. Heave response of long riserless drillstrings. Ocean Engineering 15 (5), 457–469.

Pavlov, A., Kaasa, G. O., Imsland, L., 2010. Experimental disturbance rejection on a full-scale drilling rig. In: 8th International Federation of Automatic Control Sumposium on Nonlinear Control Systems. Bologna, Italy, pp. 1338–1343.

Piché, R., Ellman, A., 1995. A fluid transmission line model for use with ode simulators. The Eight Bath International Fluid Power Workshop.

Rao, S. S., Yap, F. F., 1995. Mechanical Vibrations, 2nd Edition. Addison-Wesley.

Reddy, J. N., 1986. Applied Functional Analysis and Variational Methods in Engineering. McGraw-Hill Book Company.

Rehm, B., Schubert, J., Haghshenas, J., Paknejad, A. S., Hughes, J., 2008. Managed Pressure Drilling. Gulf Publishing Company.

Stecki, J. S., Davis, D. C., 1986a. Fluid transmission lines - distributed parameter models, part 1: A review of the state of the art. Proceedings of the Institution of Mechanical Engineers, Part A: Journal of Power and Energy 200 (4), 215–228.

Stecki, J. S., Davis, D. C., 1986b. Fluid transmission lines - distributed parameter models, part 2: Comparison of models. Proceedings of the Institution of Mechanical Engineers, Part A: Journal of Power and Energy 200 (4), 229–236.

Tikhonov, V. S., Safronov, A. I., 2002. Effect of fluid column dynamics on longitudinal vibrations of an ultra deepwater riser covered by an orifice plug. Ocean Engieneering 29 (1), 99–112.

Totland, J. F. H., 2014. Fast pressure control in managed pressure drilling.

Warren, T. M., 1989. Evaluation of jet-bit pressure losses. SPE Drilling Engineering 4 (4), 335–340.

Watton, J., Tadmori, M., 1988. A comparison of techniques for the analysis of transmission line dynamics in electrohydraulic control systems. Applied Mathematical Modelling 12, 457–466.

Appendix A

Convenience Variables

Table A.1: Convenience variables 1

Subsystem	**Series Impedance**
Fluid in pipe	$Z_i = \rho_0 s \left(1 - C\left[I_i^{(1)} + I_i^{(2)}\right]\frac{2\pi}{A_i}\right)^{-1}$
Fluid in annulus	$Z_a = \rho_0 s \left(1 - \frac{2\pi}{A_a}\left[D^{(1)} I_a^{(1)} + D^{(2)} I_a^{(2)}\right]\right)^{-1}$
Pipe	$Z_p = \rho_p s + k_p$
	Shunt Admitance
Fluid in pipe	$Y_i = s\frac{1}{\beta_i}$
Fluid in annulus	$Y_a = s\frac{1}{\beta_a}$
Pipe	$Y_p = \frac{s}{E}$
	Impedance Cross Terms
Fluid in pipe	$X_i = \frac{2\pi}{A_i} C\left[I_i^{(1)} + I_i^{(2)}\right]$
Fluid in annulus	$X_a = \frac{2\pi}{A_a}\left[E^{(1)} I_a^{(1)} + E^{(2)} I_a^{(2)}\right]$
	Admittance Cross Terms
Fluid in pipe	$Y_{i,x} = s\frac{1}{A_i}\frac{\partial A_i}{\partial p_a}$
Fluid in annulus	$Y_{a,x} = s\frac{1}{A_a}\frac{\partial A_a}{\partial p_i}$

Table A.2: Convenience variables 2

Other Convenience Variables	
$I_i^{(1)} = H_1^{(1)}(\xi r_0) r_0/\xi$	$I_i^{(2)} = H_1^{(2)}(\xi r_0) r_0/\xi$
$I_a^{(1)} = \left(H_1^{(1)}(\xi r_2) r_2 - H_1^{(1)}(\xi r_1) r_1\right)/\xi$	$I_a^{(2)} = \left(H_1^{(2)}(\xi r_2) r_2 - H_1^{(2)}(\xi r_1) r_1\right)/\xi$
$D^{(1)} = -\left(H_0^{(2)}(\xi r_2) - H_0^{(2)}(\xi r_1)\right)/W$	$D^{(2)} = \left(H_0^{(1)}(\xi r_2) - H_0^{(1)}(\xi r_1)\right)/W$
$E^{(1)} = -H_0^{(2)}(\xi r_2)/W$	$E^{(2)} = H_0^{(1)}(\xi r_2)/W$
$C = \left(H_0^{(1)}(\xi r_0) + H_0^{(2)}(\xi r_0)\right)^{-1}$	
$W = H_0^{(1)}(\xi r_2) H_0^{(2)}(\xi r_1) - H_0^{(1)}(\xi r_1) H_0^{(2)}(\xi r_2)$	
$\xi = i\sqrt{s/\nu}$	
$H_n^{(1)}, H_n^{(2)}$ are the n'th order Hankel function of teh first and second kind respectively.	

Appendix B

Frequency Responses: Analytical Versus Irrational Ritz Approximations

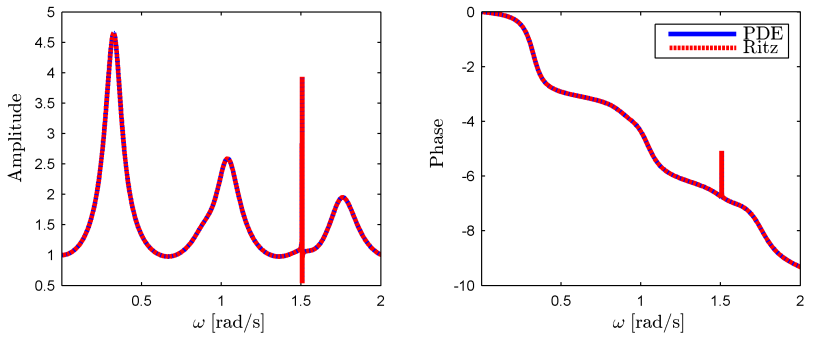

Figure B.1: Frequency diagram: $\bar{V}_i(0)/\bar{V}_i(L)$, 16 modes

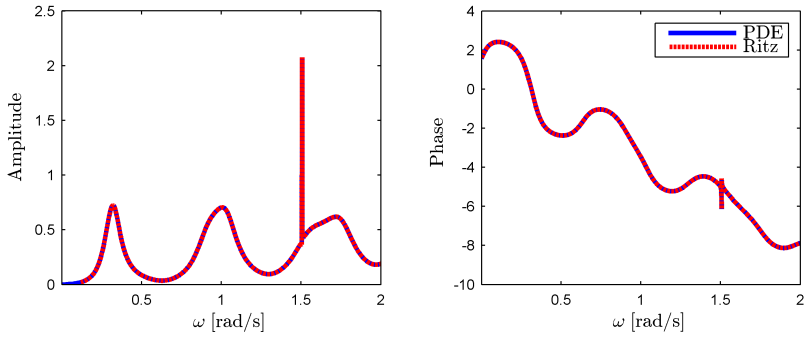

Figure B.2: Frequency diagram: $\bar{V}_i(0)/\bar{V}_a(L)$, 16 modes

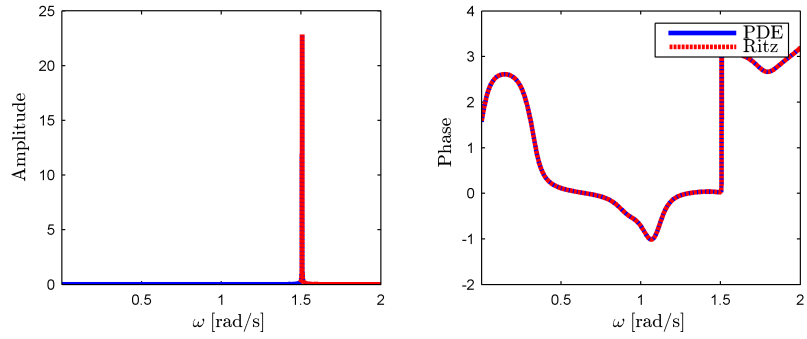

Figure B.3: Frequency diagram: $\bar{V}_i(0)/\bar{V}_p(L)$, 16 modes

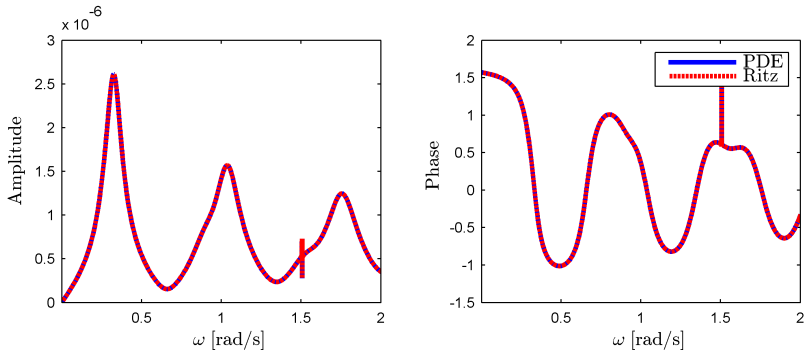

Figure B.4: Frequency diagram: $\bar{V}_i(0)/P_i(0)$, 16 modes

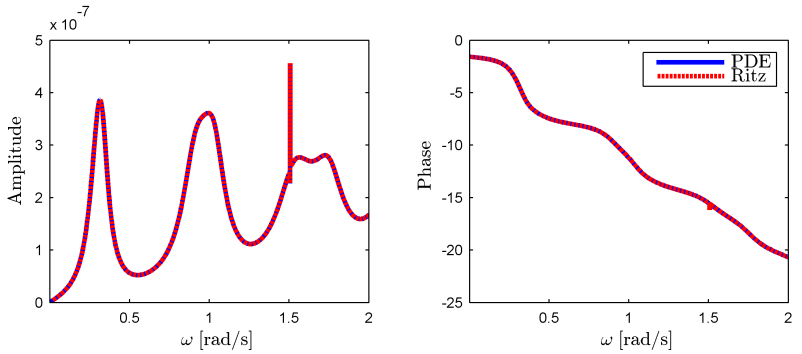

Figure B.5: Frequency diagram: $\bar{V}_i(0)/P_a(0)$, 16 modes

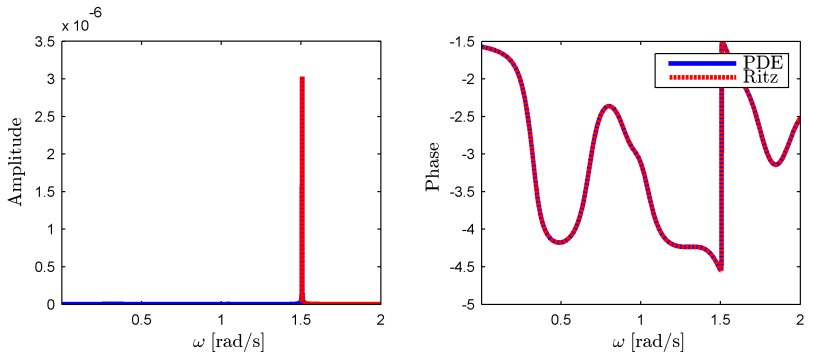

Figure B.6: Frequency diagram: $\bar{V}_i(0)/P_p(0)$, 16 modes

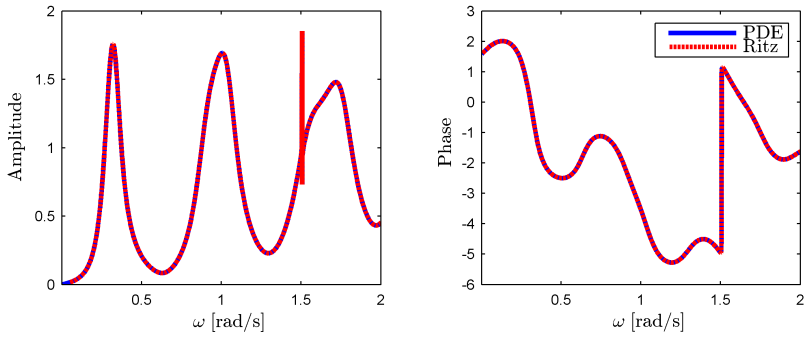

Figure B.7: Frequency diagram: $\bar{V}_a(0)/\bar{V}_i(L)$, 16 modes

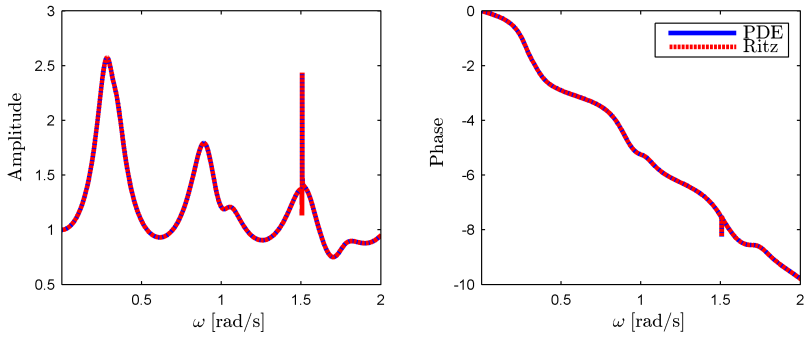

Figure B.8: Frequency diagram: $\bar{V}_a(0)/\bar{V}_a(L)$, 16 modes

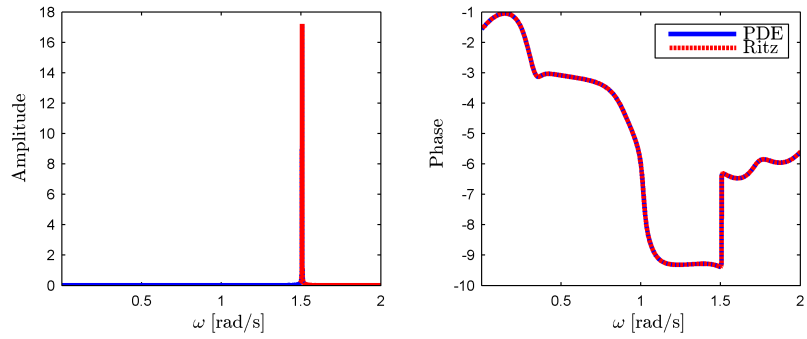

Figure B.9: Frequency diagram: $\bar{V}_a(0)/\bar{V}_p(L)$, 16 modes

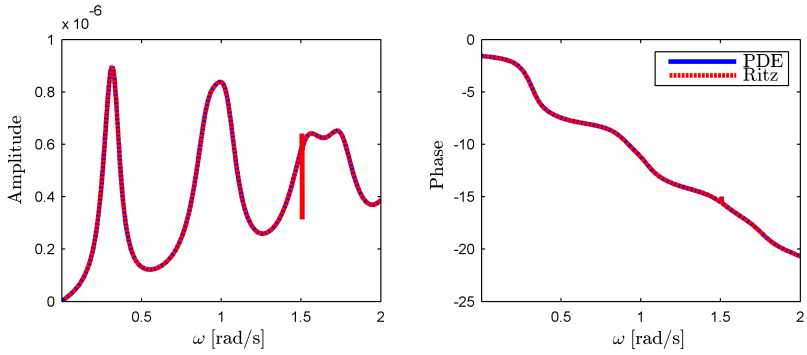

Figure B.10: Frequency diagram: $\bar{V}_a(0)/P_i(0)$, 16 modes

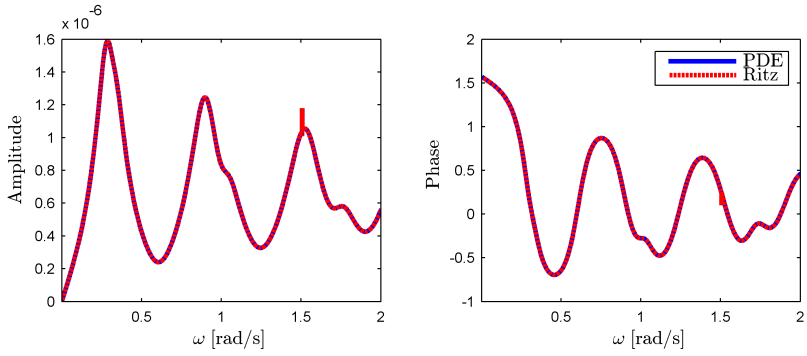

Figure B.11: Frequency diagram: $\bar{V}_a(0)/P_a(0)$, 16 modes

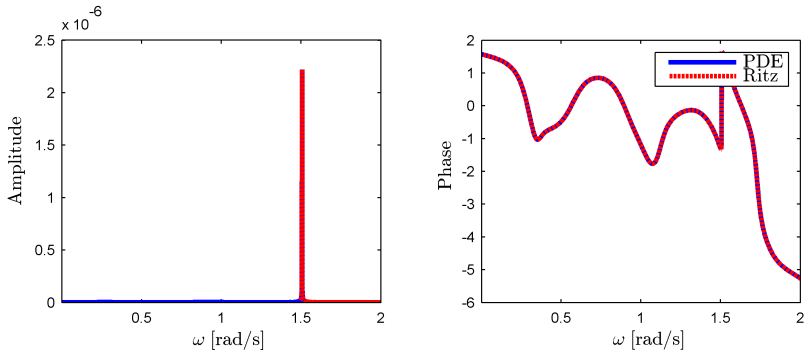

Figure B.12: Frequency diagram: $\bar{V}_a(0)/P_p(0)$, 16 modes

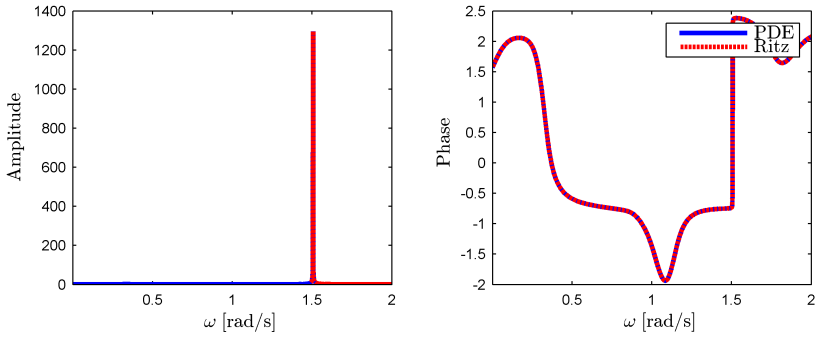

Figure B.13: Frequency diagram: $\bar{V}_p(0)/\bar{V}_i(L)$, 16 modes

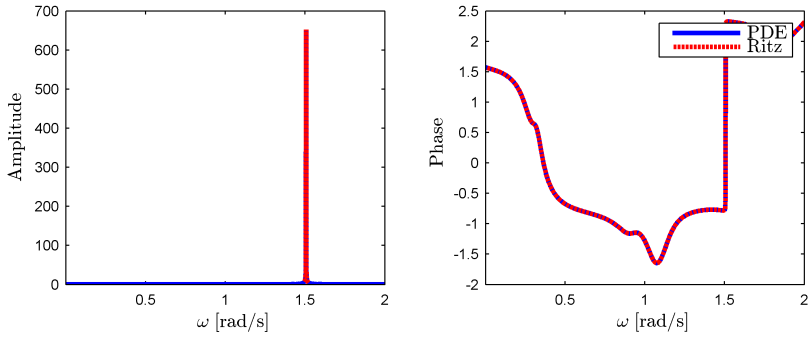

Figure B.14: Frequency diagram: $\bar{V}_p(0)/\bar{V}_a(L)$, 16 modes

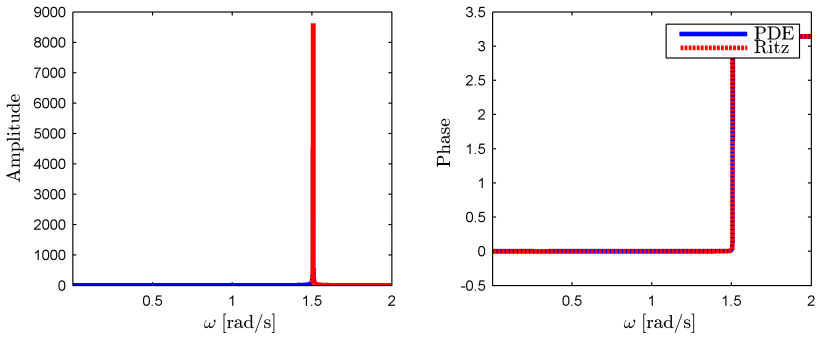

Figure B.15: Frequency diagram: $\bar{V}_p(0)/\bar{V}_p(L)$, 16 modes

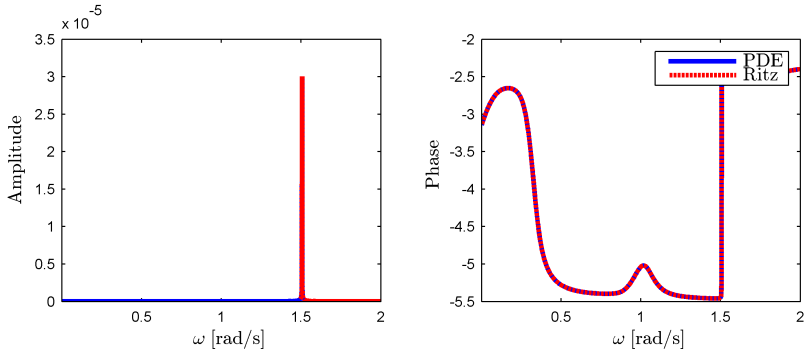

Figure B.16: Frequency diagram: $\bar{V}_p(0)/P_i(0)$, 16 modes

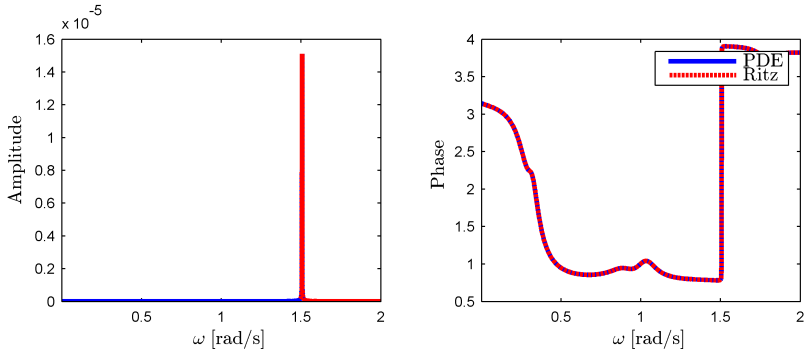

Figure B.17: Frequency diagram: $\bar{V}_p(0)/P_a(0)$, 16 modes

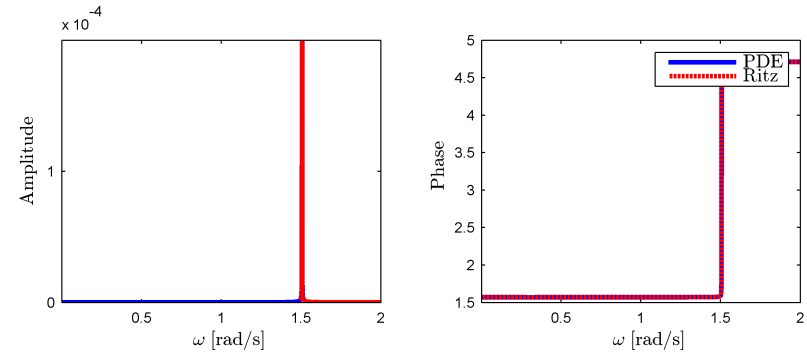

Figure B.18: Frequency diagram: $\bar{V}_p(0)/P_p(0)$, 16 modes

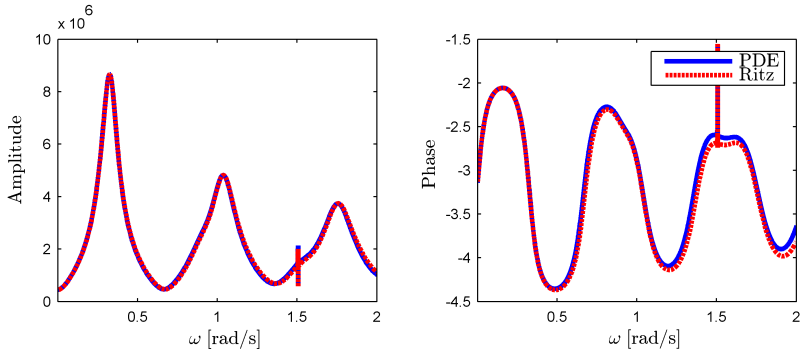

Figure B.19: Frequency diagram: $P_i(L)/\bar{V}_i(L)$, 16 modes

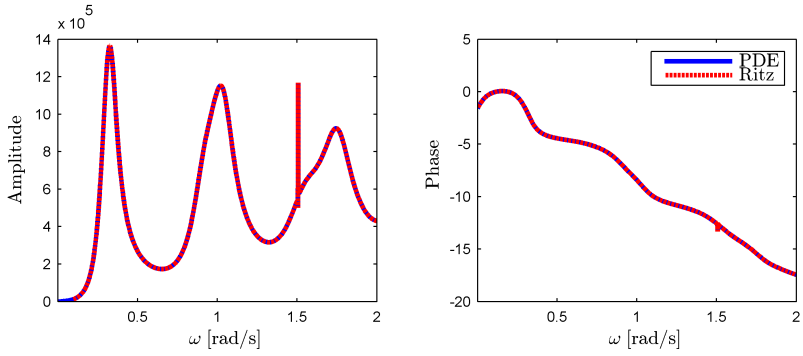

Figure B.20: Frequency diagram: $P_i(L)/\bar{V}_a(L)$, 16 modes

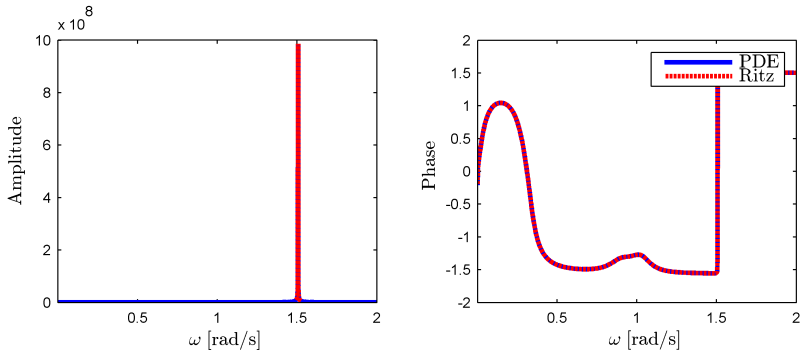

Figure B.21: Frequency diagram: $P_i(L)/\bar{V}_p(L)$, 16 modes

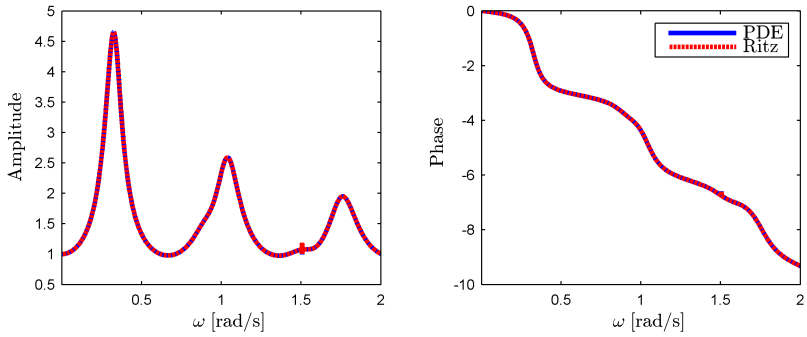

Figure B.22: Frequency diagram: $P_i(L)/P_i(0)$, 16 modes

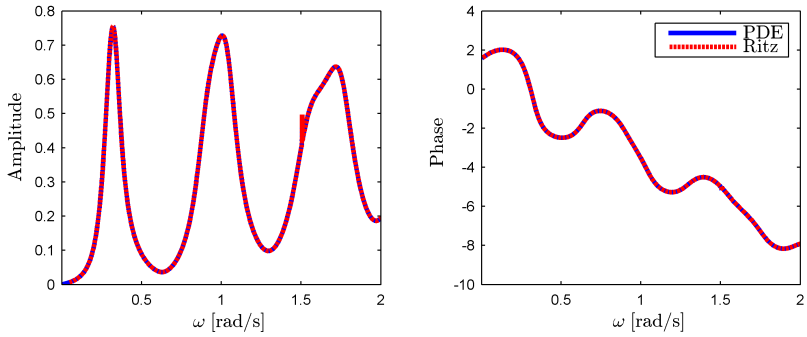

Figure B.23: Frequency diagram: $P_i(L)/P_a(0)$, 16 modes

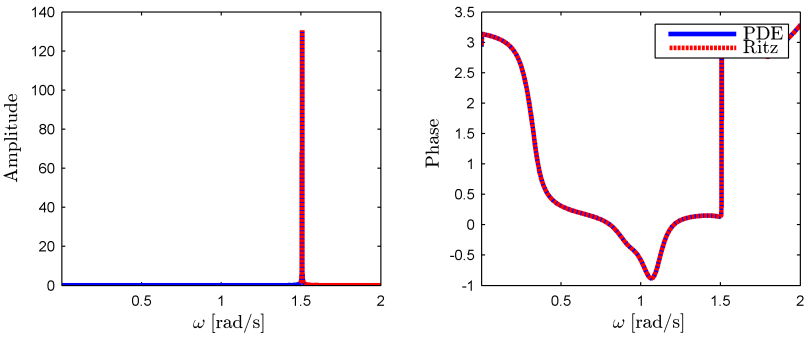

Figure B.24: Frequency diagram: $P_i(L)/P_p(0)$, 16 modes

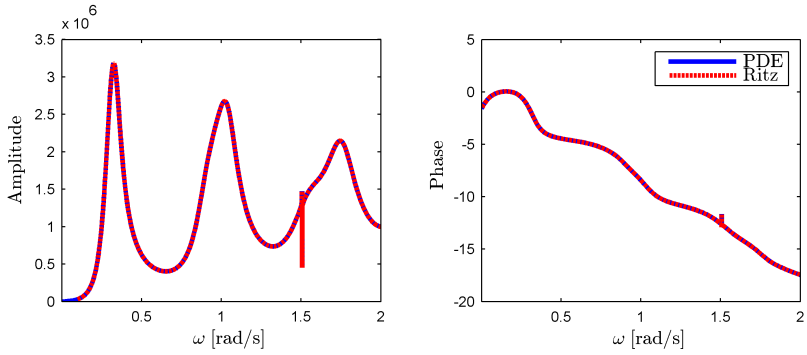

Figure B.25: Frequency diagram: $P_a(L)/\bar{V}_i(L)$, 16 modes

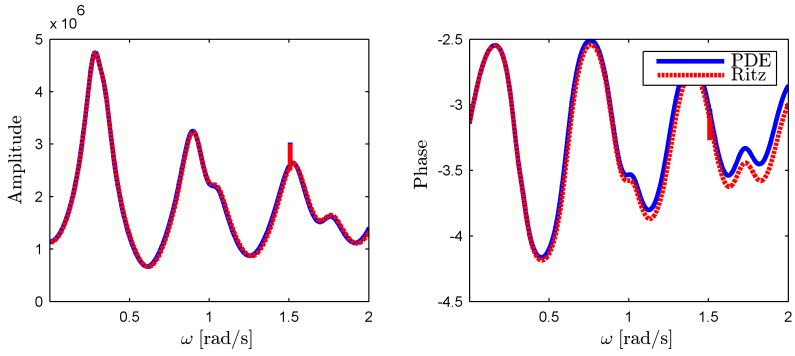

Figure B.26: Frequency diagram: $P_a(L)/\bar{V}_a(L)$, 16 modes

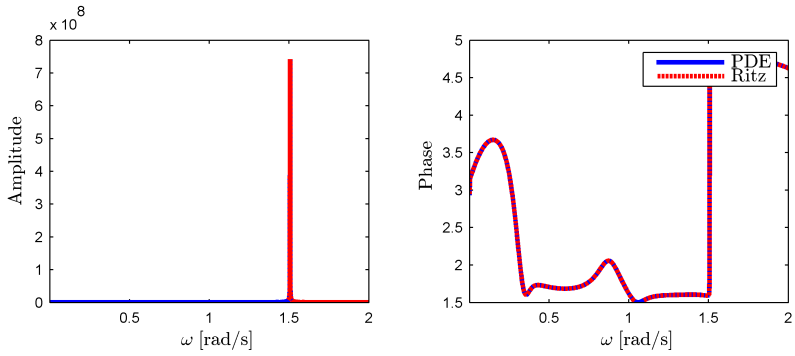

Figure B.27: Frequency diagram: $P_a(L)/\bar{V}_p(L)$, 16 modes

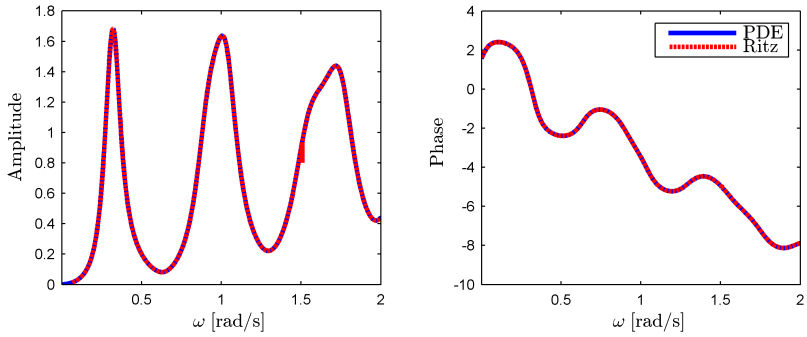

Figure B.28: Frequency diagram: $P_a(L)/P_i(0)$, 16 modes

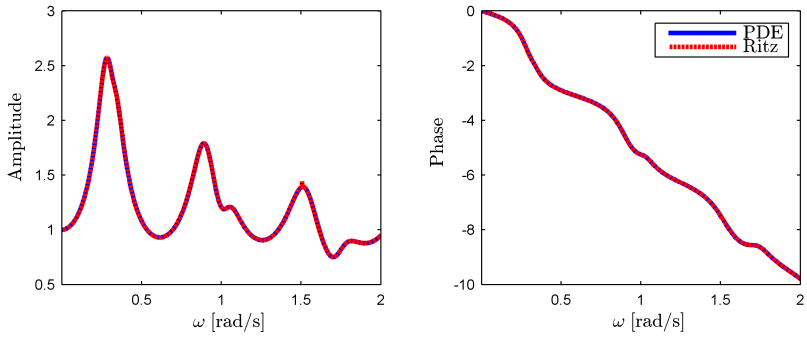

Figure B.29: Frequency diagram: $P_a(L)/P_a(0)$, 16 modes

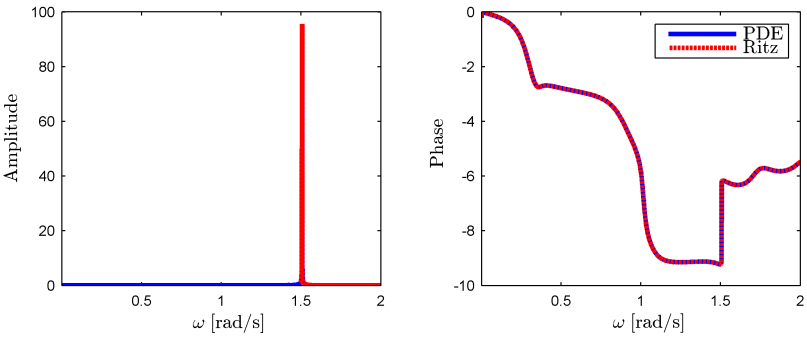

Figure B.30: Frequency diagram: $P_a(L)/P_p(0)$, 16 modes

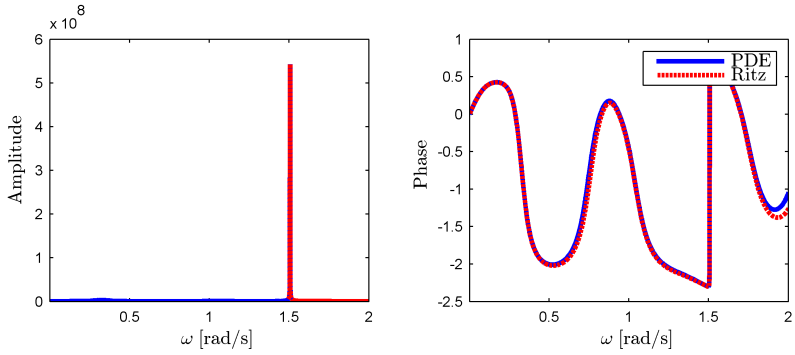

Figure B.31: Frequency diagram: $P_p(L)/\bar{V}_i(L)$, 16 modes

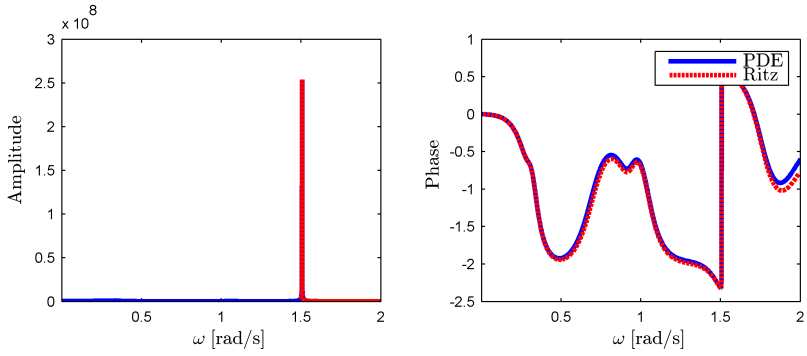

Figure B.32: Frequency diagram: $P_p(L)/\bar{V}_a(L)$, 16 modes

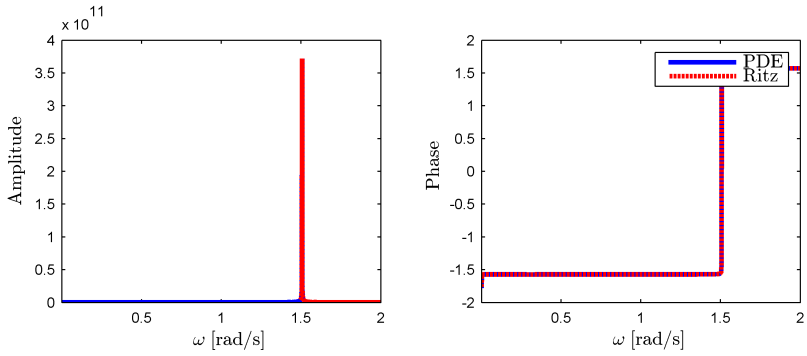

Figure B.33: Frequency diagram: $P_p(L)/\bar{V}_p(L)$, 16 modes

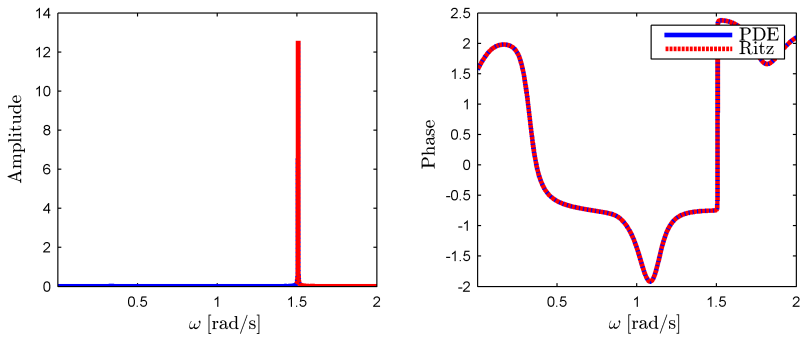

Figure B.34: Frequency diagram: $P_p(L)/P_i(0)$, 16 modes

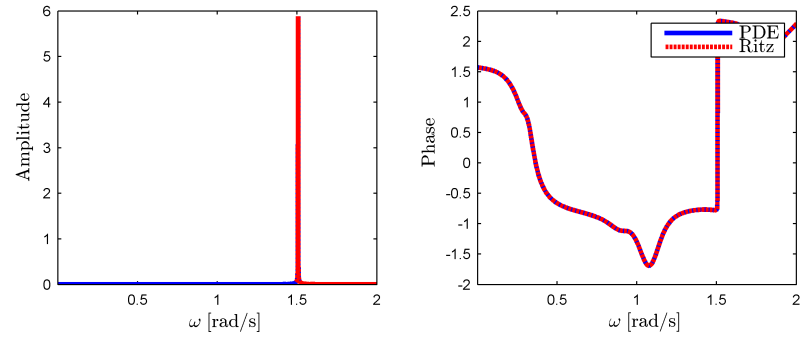

Figure B.35: Frequency diagram: $P_p(L)/P_a(0)$, 16 modes

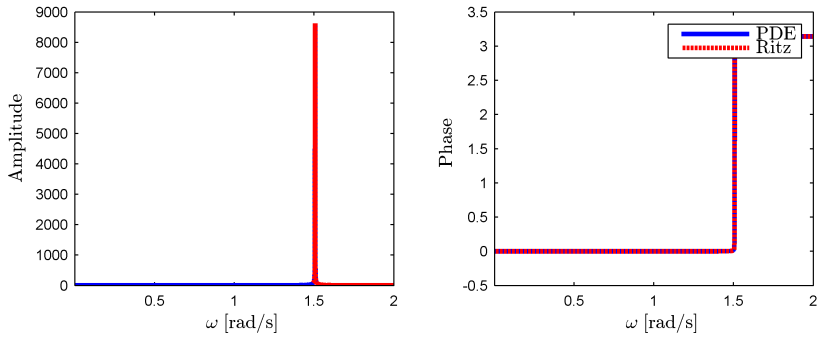

Figure B.36: Frequency diagram: $P_p(L)/P_p(0)$, 16 modes

Appendix C

Frequency Responses: Analytical Versus Rational Approximations 1

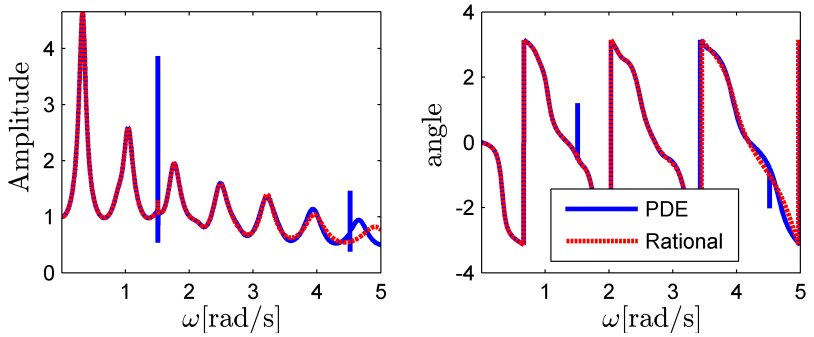

Figure C.1: Frequency diagram: $\bar{V}_i(0)/\bar{V}_i(L)$, $r = 64$, $\sigma = 0$.

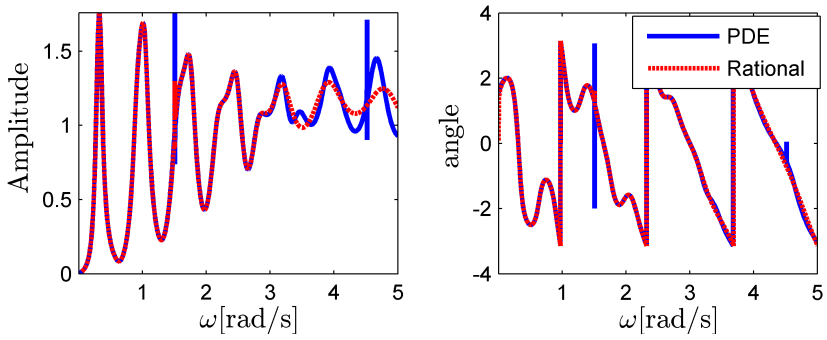

Figure C.2: Frequency diagram: $\bar{V}_i(0)/\bar{V}_a(L)$, $r = 64$, $\sigma = 0$.

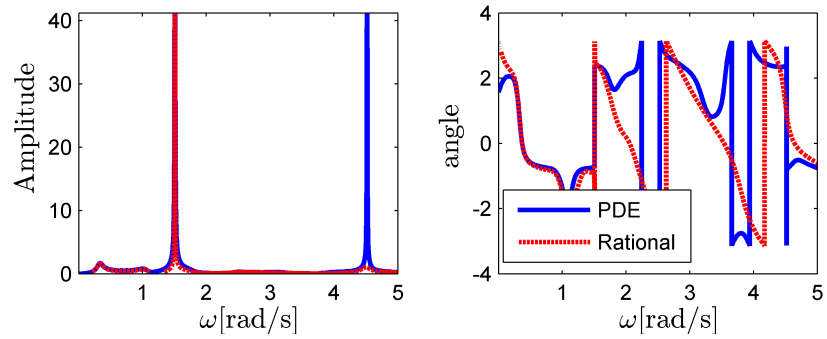

Figure C.3: Frequency diagram: $\bar{V}_i(0)/\bar{V}_p(L)$, $r = 64$, $\sigma = 0$.

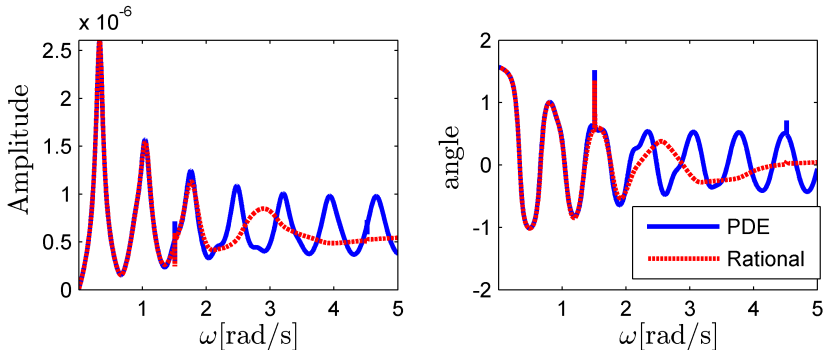

Figure C.4: Frequency diagram: $\bar{V}_i(0)/P_i(0)$, $r = 64$, $\sigma = 0$.

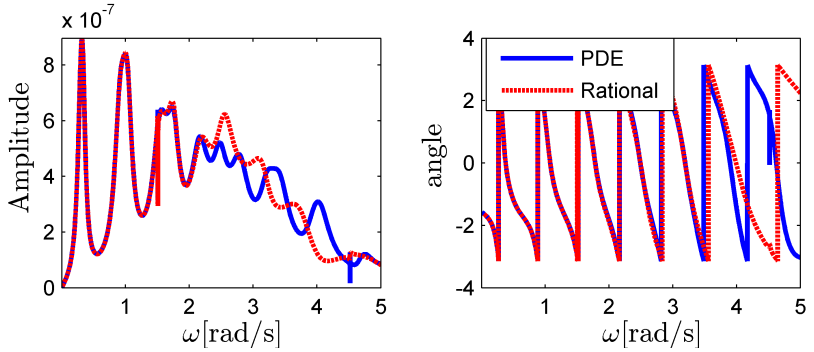

Figure C.5: Frequency diagram: $\bar{V}_i(0)/P_a(0)$, $r = 64$, $\sigma = 0$.

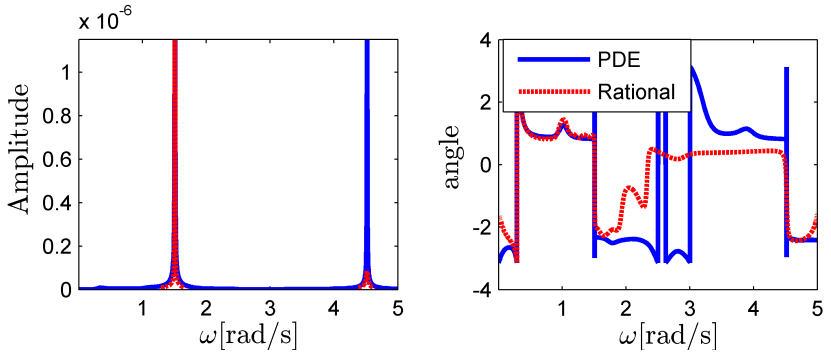

Figure C.6: Frequency diagram: $\bar{V}_i(0)/P_p(0)$, $r = 64$, $\sigma = 0$.

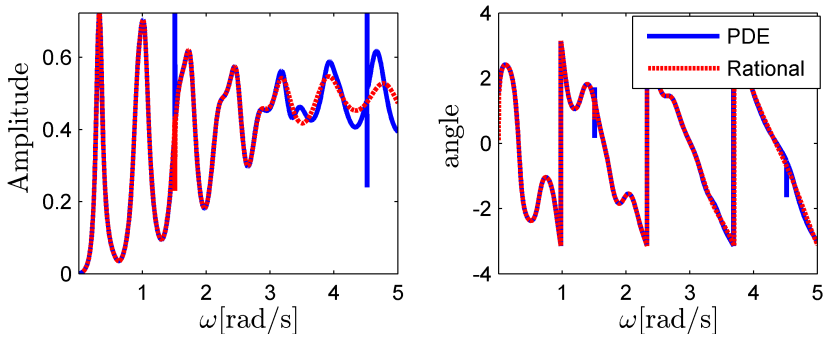

Figure C.7: Frequency diagram: $\bar{V}_a(0)/\bar{V}_i(L)$, $r = 64$, $\sigma = 0$.

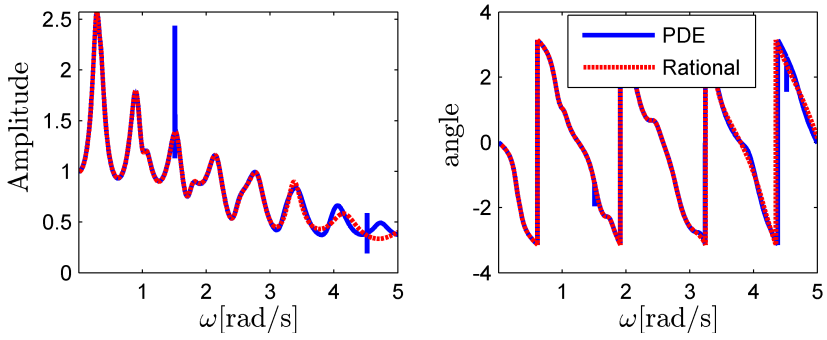

Figure C.8: Frequency diagram: $\bar{V}_a(0)/\bar{V}_a(L)$, $r = 64$, $\sigma = 0$.

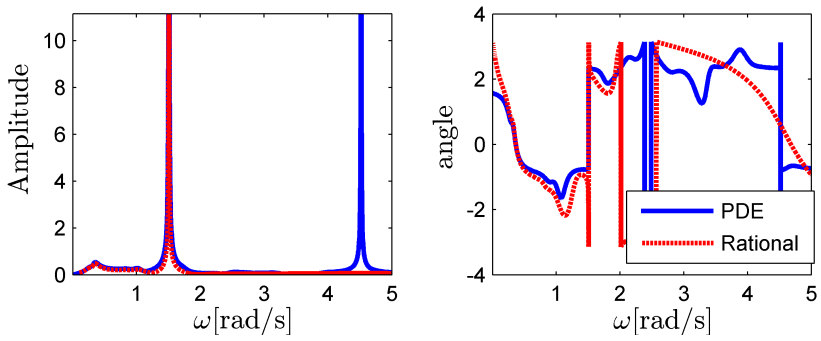

Figure C.9: Frequency diagram: $\bar{V}_a(0)/\bar{V}_p(L)$, $r = 64$, $\sigma = 0$.

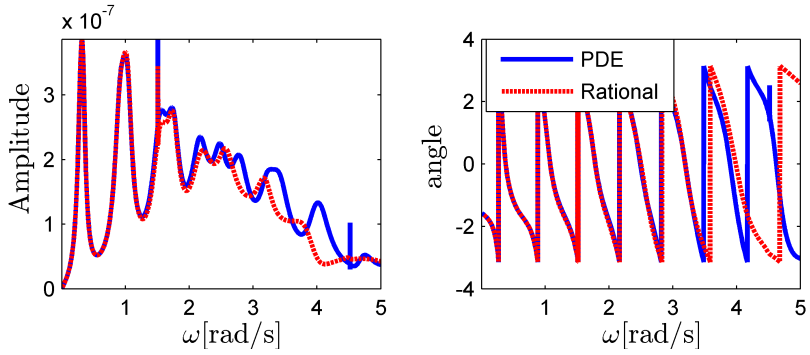

Figure C.10: Frequency diagram: $\bar{V}_a(0)/P_i(0)$, $r = 64$, $\sigma = 0$.

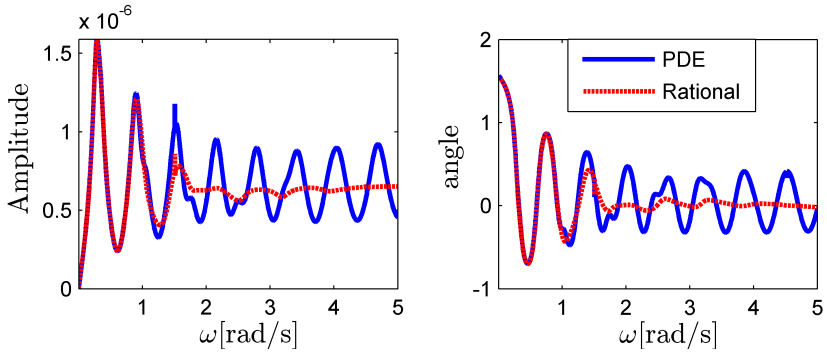

Figure C.11: Frequency diagram: $\bar{V}_a(0)/P_a(0)$, $r = 64$, $\sigma = 0$.

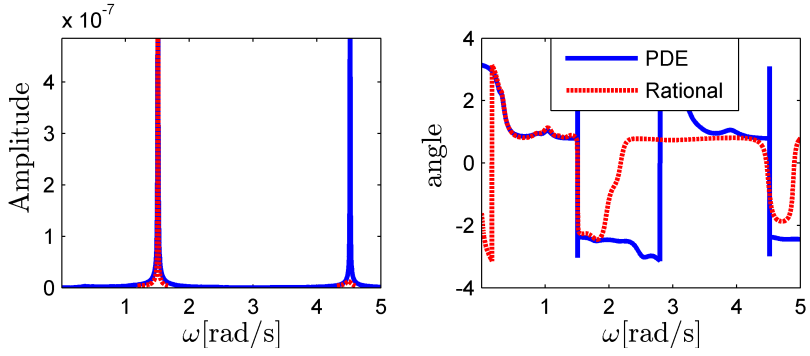

Figure C.12: Frequency diagram: $\bar{V}_a(0)/P_p(0)$, $r = 64$, $\sigma = 0$.

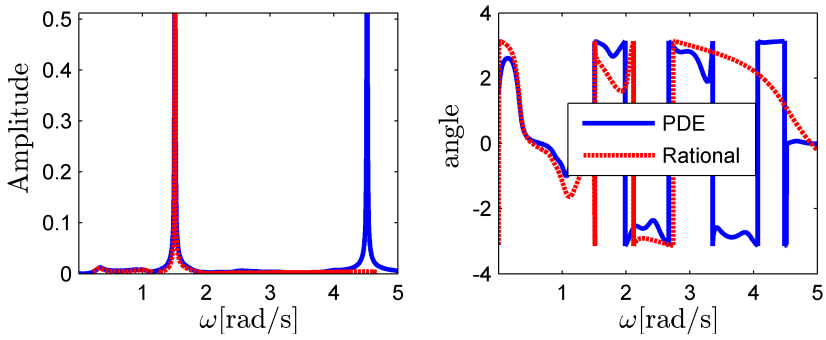

Figure C.13: Frequency diagram: $\bar{V}_p(0)/\bar{V}_i(L)$, $r = 64$, $\sigma = 0$.

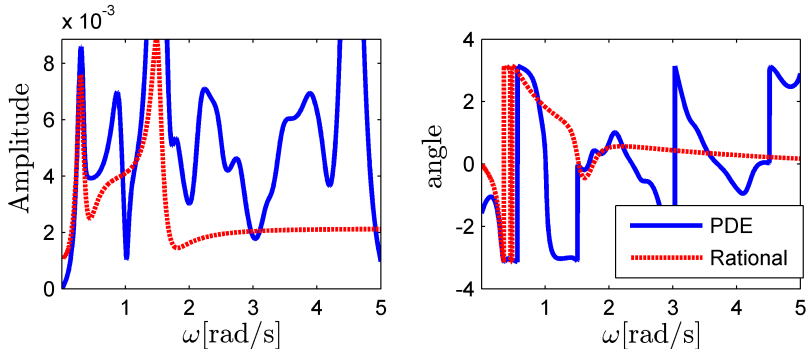

Figure C.14: Frequency diagram: $\bar{V}_p(0)/\bar{V}_a(L)$, $r = 64$, $\sigma = 0$.

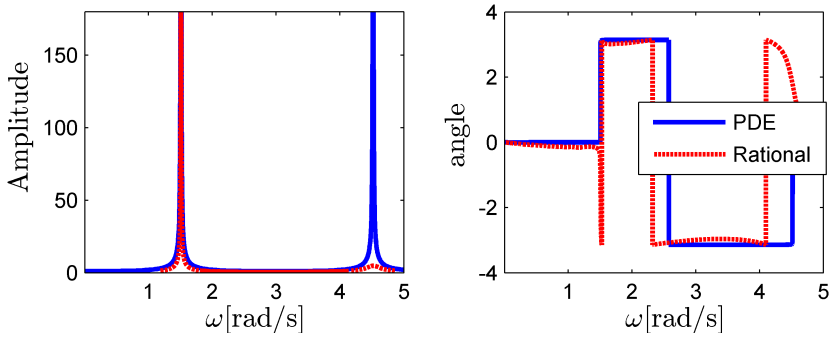

Figure C.15: Frequency diagram: $\bar{V}_p(0)/\bar{V}_p(L)$, $r = 64$, $\sigma = 0$.

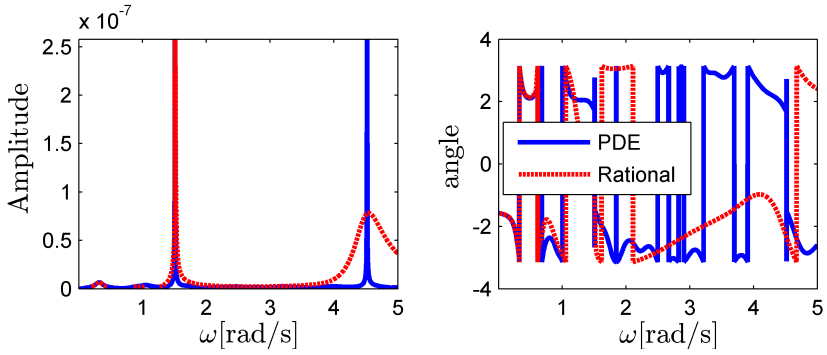

Figure C.16: Frequency diagram: $\bar{V}_p(0)/P_i(0)$, $r = 64$, $\sigma = 0$.

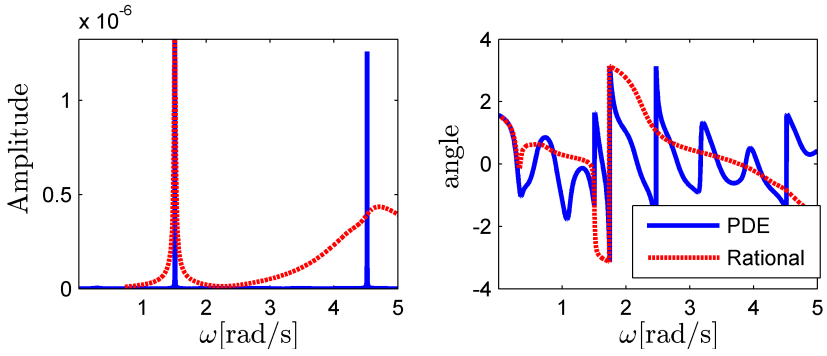

Figure C.17: Frequency diagram: $\bar{V}_p(0)/P_a(0)$, $r = 64$, $\sigma = 0$.

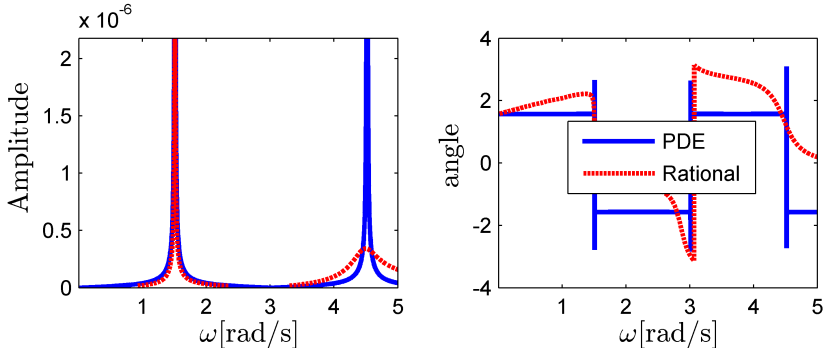

Figure C.18: Frequency diagram: $\bar{V}_p(0)/P_p(0)$, $r = 64$, $\sigma = 0$.

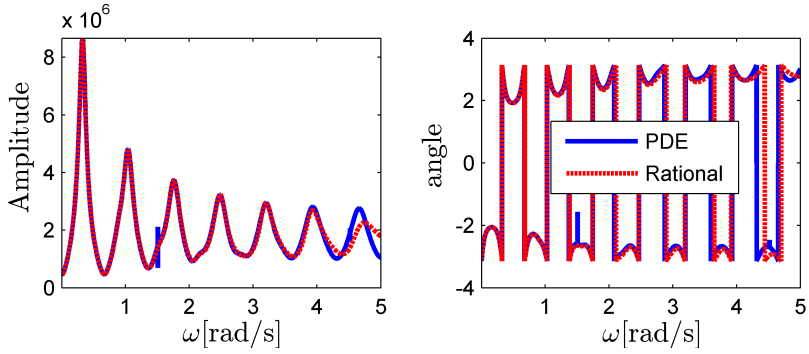

Figure C.19: Frequency diagram: $P_i(L)/\bar{V}_i(L)$, $r = 64$, $\sigma = 0$.

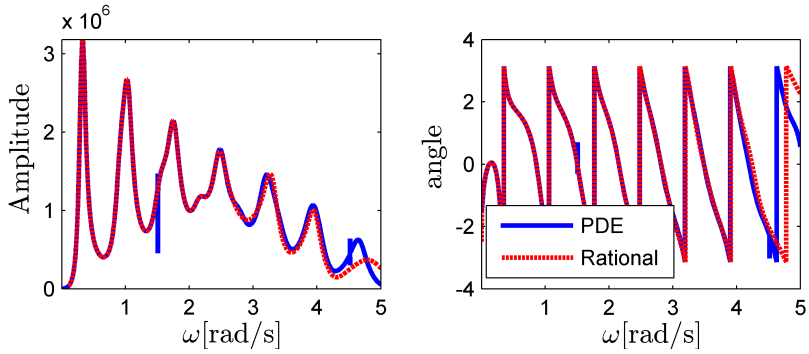

Figure C.20: Frequency diagram: $P_i(L)/\bar{V}_a(L)$, $r = 64$, $\sigma = 0$.

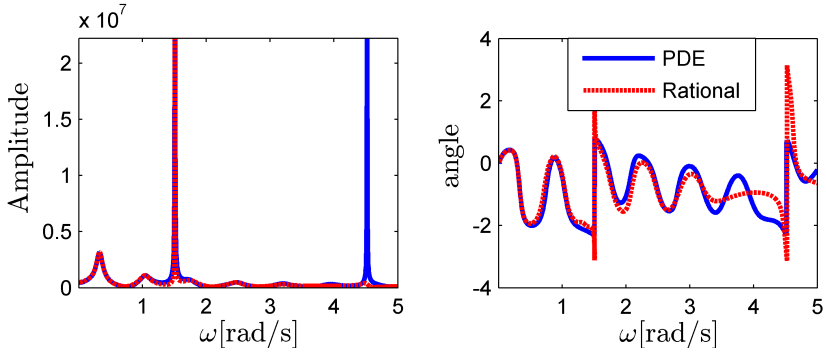

Figure C.21: Frequency diagram: $P_i(L)/\bar{V}_p(L)$, $r = 64$, $\sigma = 0$.

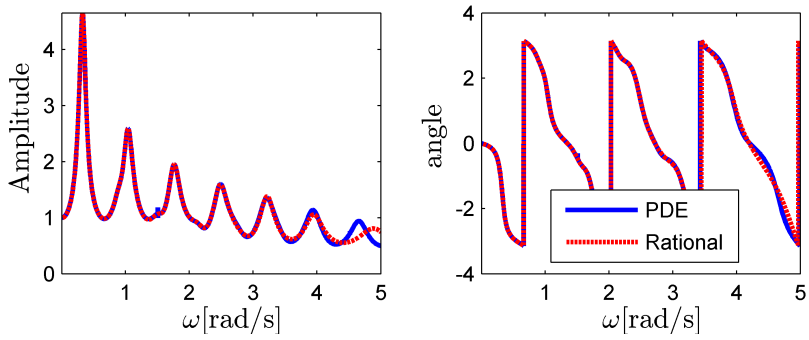

Figure C.22: Frequency diagram: $P_i(L)/P_i(0)$, $r = 64$, $\sigma = 0$.

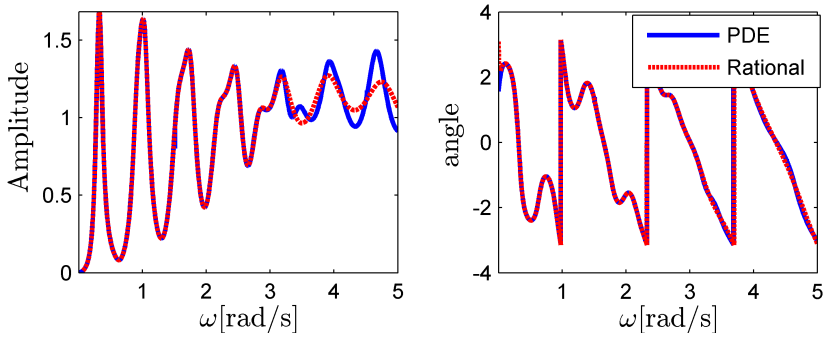

Figure C.23: Frequency diagram: $P_i(L)/P_a(0)$, $r = 64$, $\sigma = 0$.

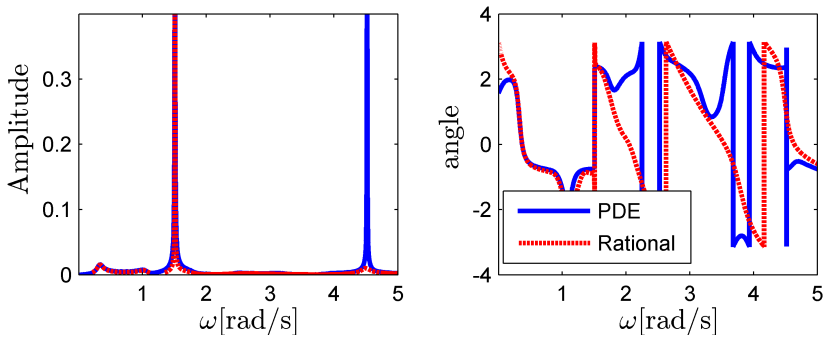

Figure C.24: Frequency diagram: $P_i(L)/P_p(0)$, $r = 64$, $\sigma = 0$.

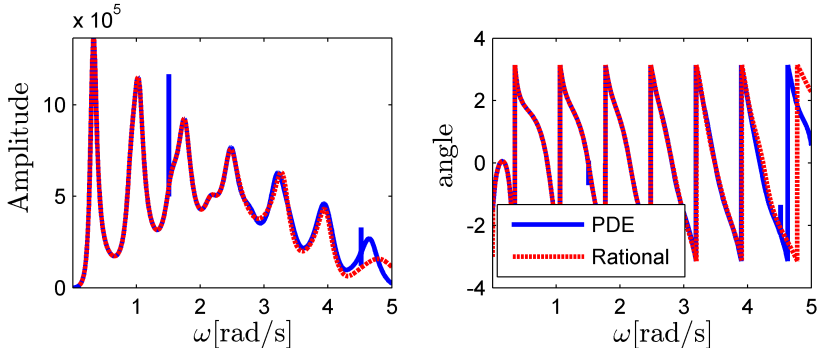

Figure C.25: Frequency diagram: $P_a(L)/\bar{V}_i(L)$, $r = 64$, $\sigma = 0$.

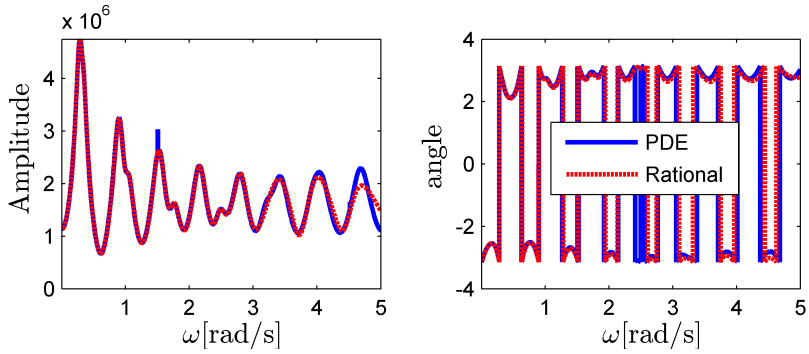

Figure C.26: Frequency diagram: $P_a(L)/\bar{V}_a(L)$, $r = 64$, $\sigma = 0$.

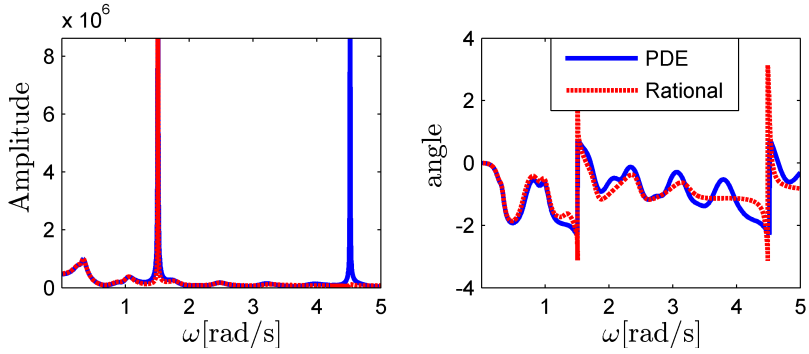

Figure C.27: Frequency diagram: $P_a(L)/\bar{V}_p(L)$, $r = 64$, $\sigma = 0$.

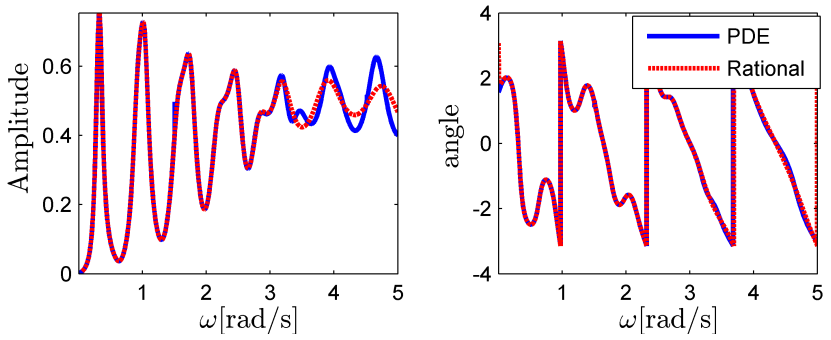

Figure C.28: Frequency diagram: $P_a(L)/P_i(0)$, $r = 64$, $\sigma = 0$.

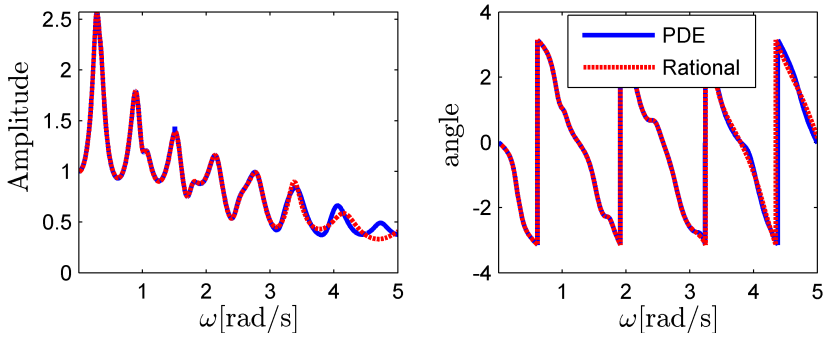

Figure C.29: Frequency diagram: $P_a(L)/P_a(0)$, $r = 64$, $\sigma = 0$.

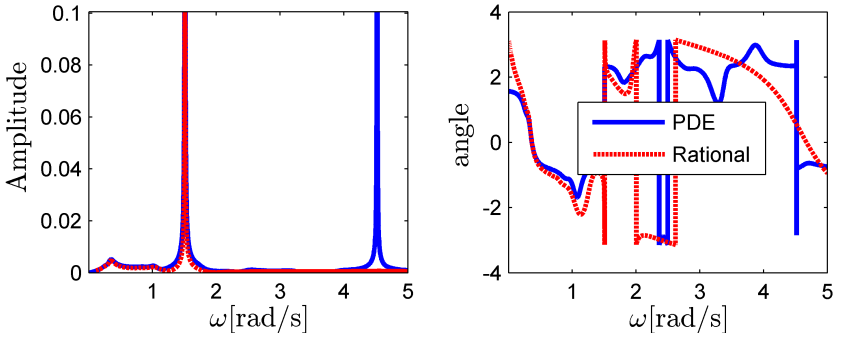

Figure C.30: Frequency diagram: $P_a(L)/P_p(0)$, $r = 64$, $\sigma = 0$.

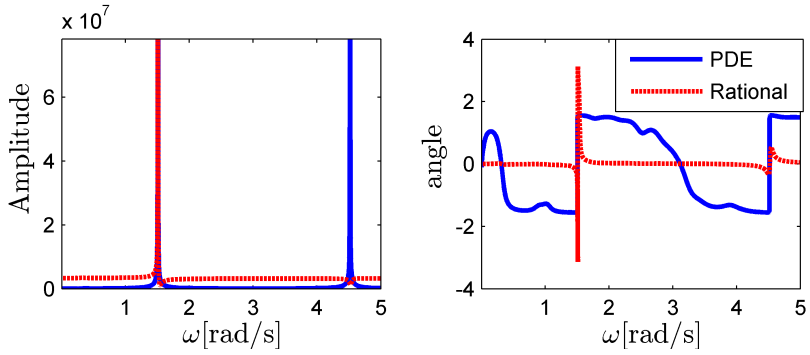

Figure C.31: Frequency diagram: $P_p(L)/\bar{V}_i(L)$, $r = 64$, $\sigma = 0$.

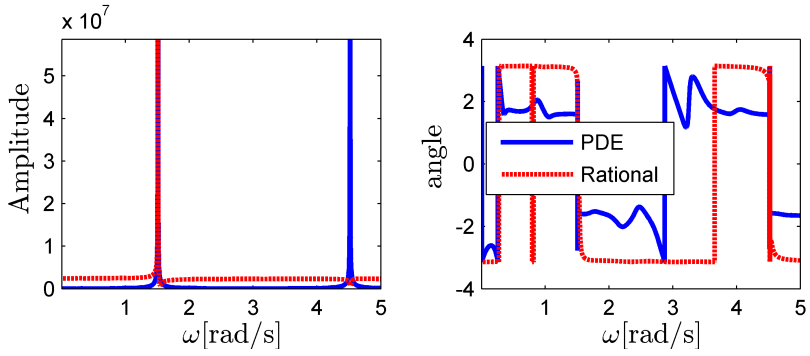

Figure C.32: Frequency diagram: $P_p(L)/\bar{V}_a(L)$, $r = 64$, $\sigma = 0$.

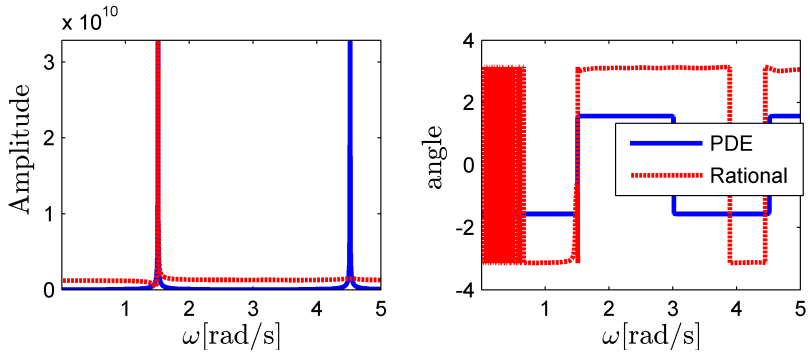

Figure C.33: Frequency diagram: $P_p(L)/\bar{V}_p(L)$, $r = 64$, $\sigma = 0$.

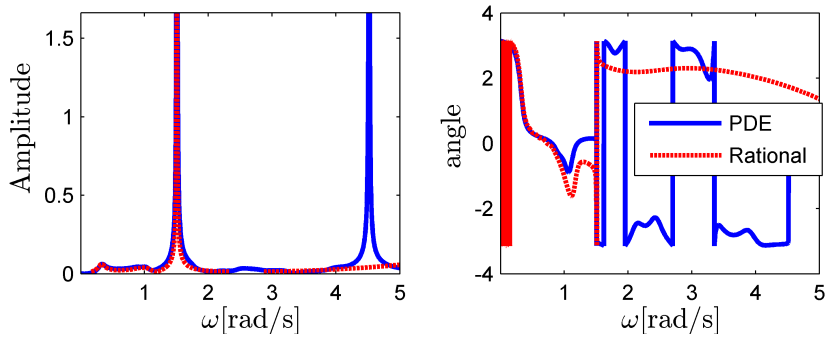

Figure C.34: Frequency diagram: $P_p(L)/P_i(0)$, $r = 64$, $\sigma = 0$.

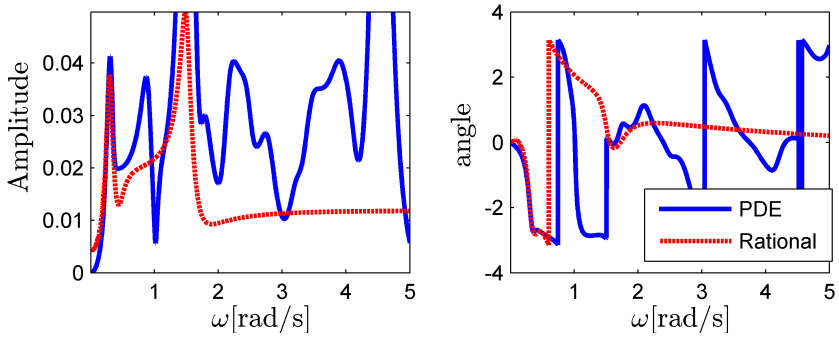

Figure C.35: Frequency diagram: $P_p(L)/P_a(0)$, $r = 64$, $\sigma = 0$.

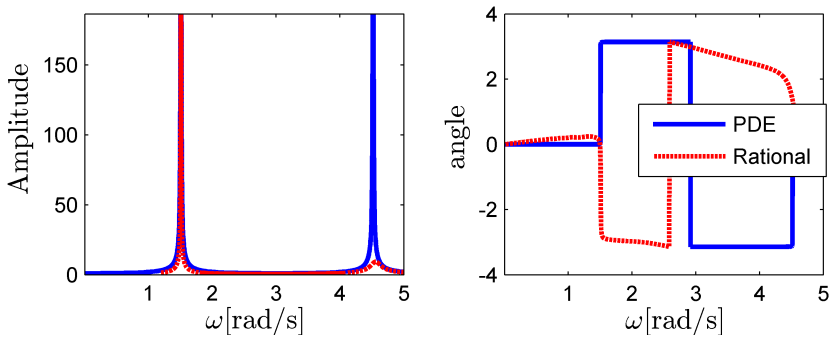

Figure C.36: Frequency diagram: $P_p(L)/P_p(0)$, $r = 64$, $\sigma = 0$.

Appendix D

Frequency Responses: Analytical Versus Rational Approximations 2

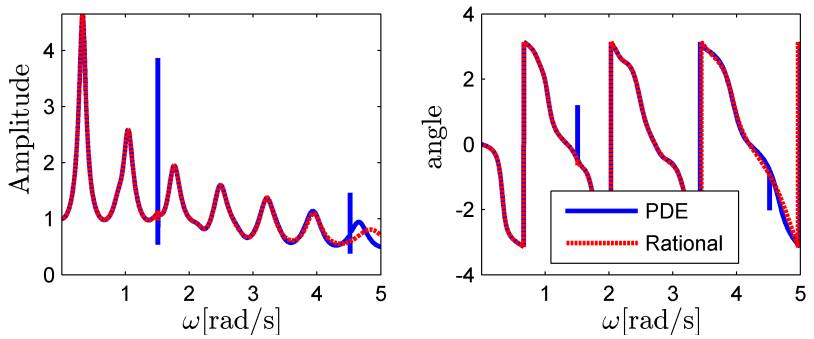

Figure D.1: Frequency diagram: $\bar{V}_i(0)/\bar{V}_i(L)$, $r = 64$, $\sigma = 0.01$.

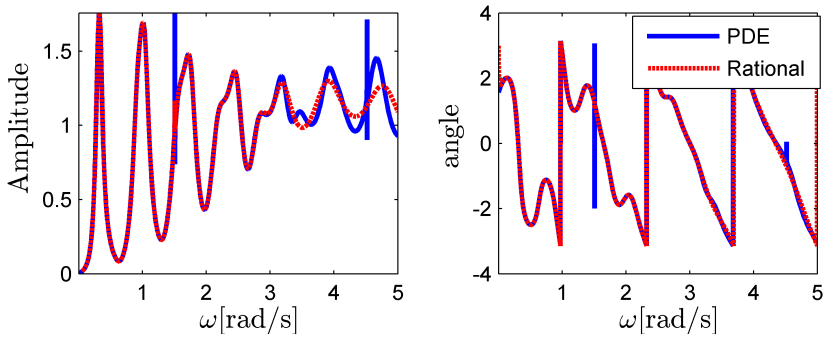

Figure D.2: Frequency diagram: $\bar{V}_i(0)/\bar{V}_a(L)$, $r = 64$, $\sigma = 0.01$.

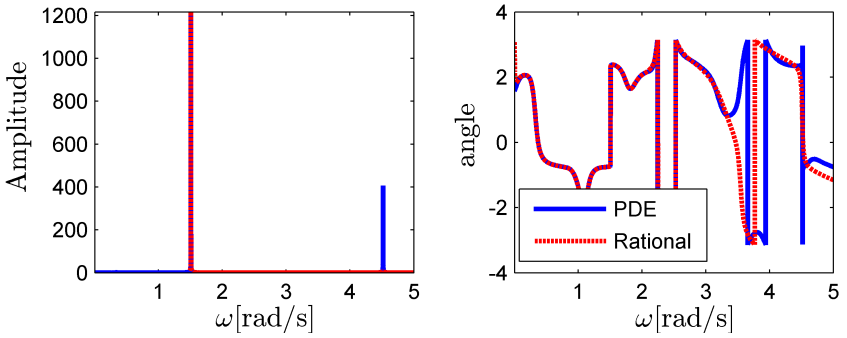

Figure D.3: Frequency diagram: $\bar{V}_i(0)/\bar{V}_p(L)$, $r = 64$, $\sigma = 0.01$.

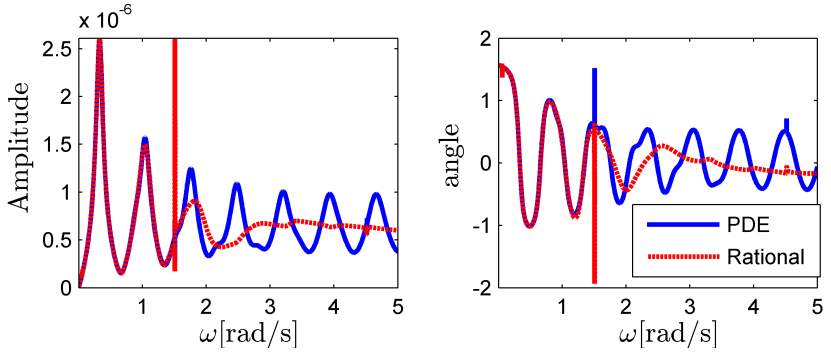

Figure D.4: Frequency diagram: $\bar{V}_i(0)/P_i(0)$, $r = 64$, $\sigma = 0.01$.

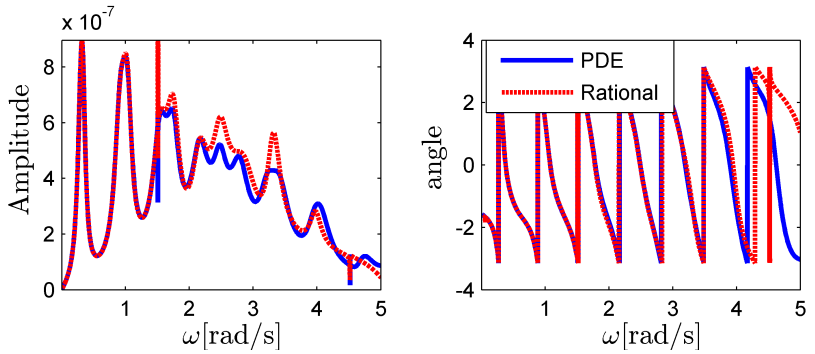

Figure D.5: Frequency diagram: $\bar{V}_i(0)/P_a(0)$, $r = 64$, $\sigma = 0.01$.

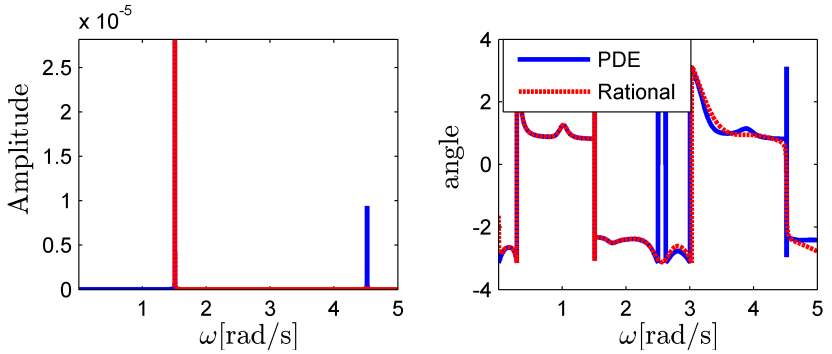

Figure D.6: Frequency diagram: $\bar{V}_i(0)/P_p(0)$, $r = 64$, $\sigma = 0.01$.

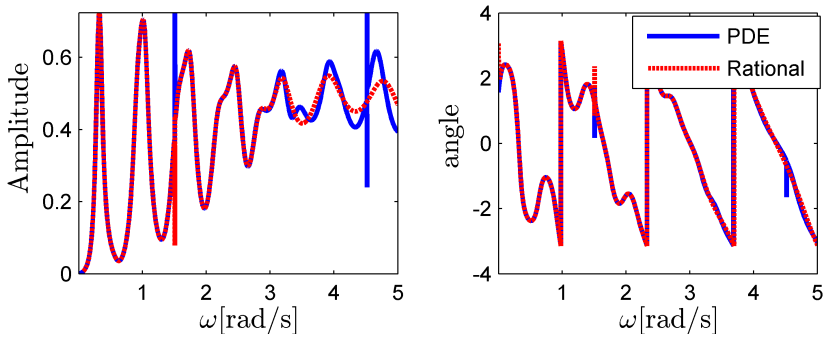

Figure D.7: Frequency diagram: $\bar{V}_a(0)/\bar{V}_i(L)$, $r = 64$, $\sigma = 0.01$.

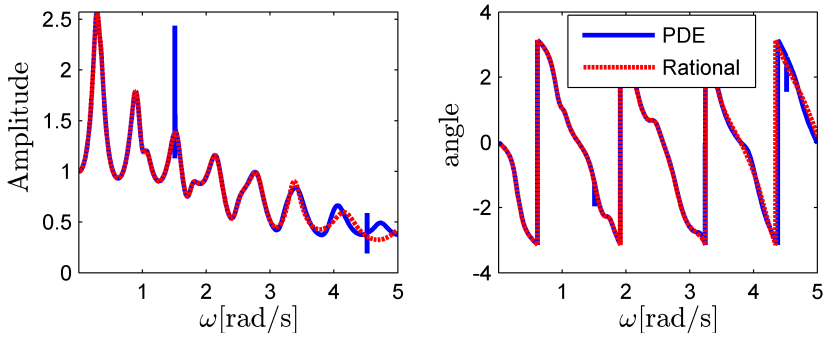

Figure D.8: Frequency diagram: $\bar{V}_a(0)/\bar{V}_a(L)$, $r = 64$, $\sigma = 0.01$.

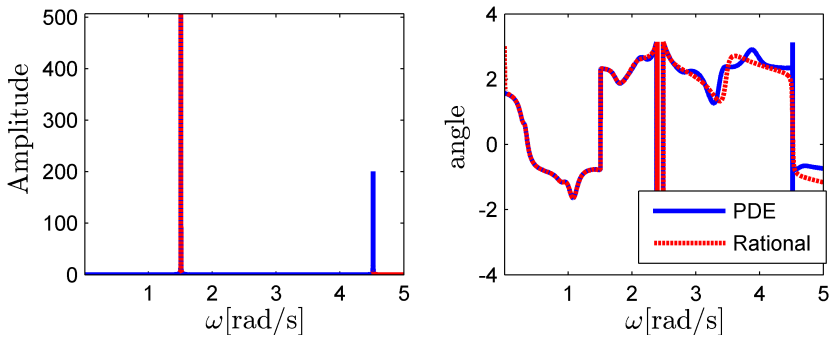

Figure D.9: Frequency diagram: $\bar{V}_a(0)/\bar{V}_p(L)$, $r = 64$, $\sigma = 0.01$.

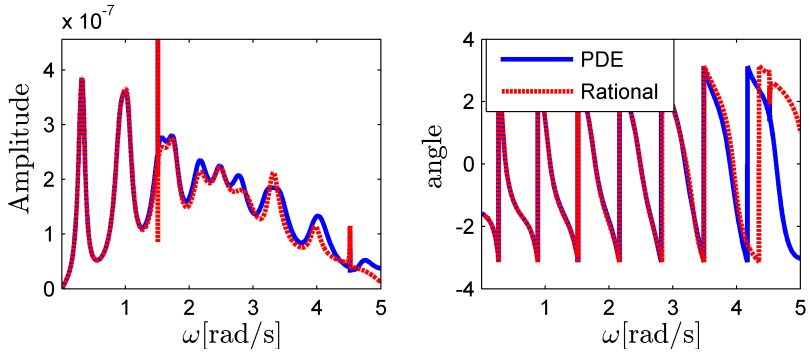

Figure D.10: Frequency diagram: $\bar{V}_a(0)/P_i(0)$, $r = 64$, $\sigma = 0.01$.

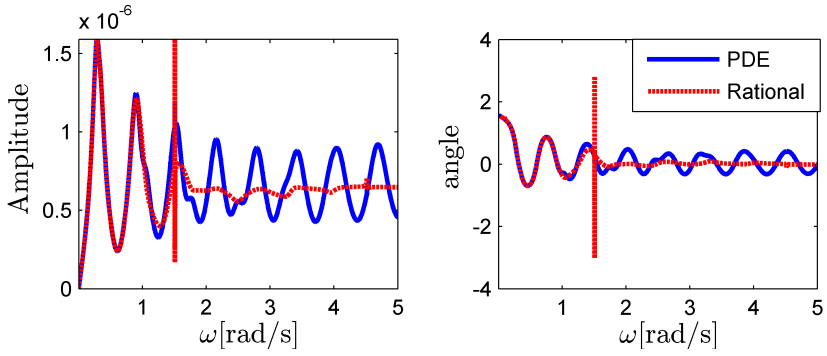

Figure D.11: Frequency diagram: $\bar{V}_a(0)/P_a(0)$, $r = 64$, $\sigma = 0.01$.

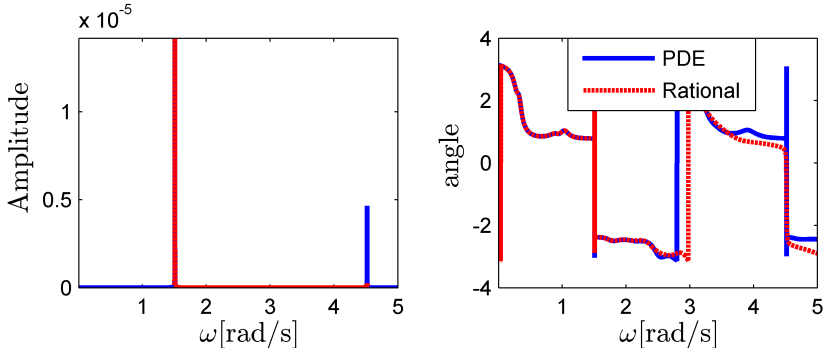

Figure D.12: Frequency diagram: $\bar{V}_a(0)/P_p(0)$, $r = 64$, $\sigma = 0.01$.

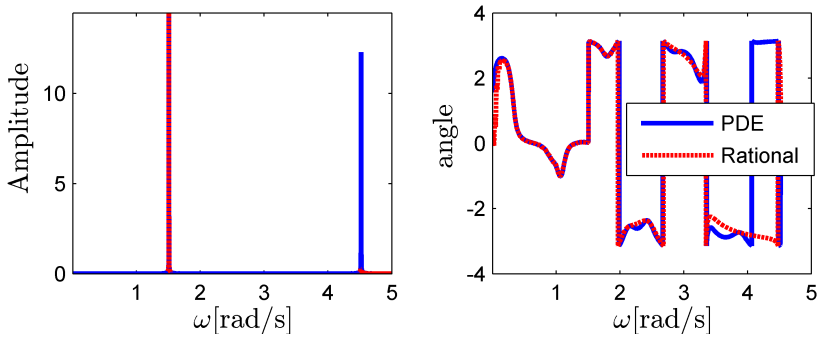

Figure D.13: Frequency diagram: $\bar{V}_p(0)/\bar{V}_i(L)$, $r = 64$, $\sigma = 0.01$.

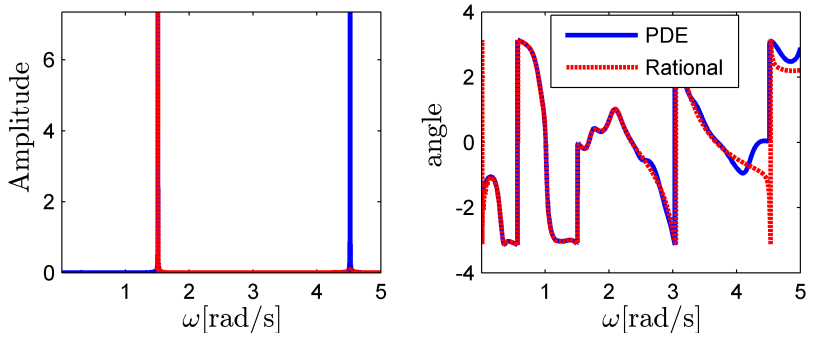

Figure D.14: Frequency diagram: $\bar{V}_p(0)/\bar{V}_a(L)$, $r = 64$, $\sigma = 0.01$.

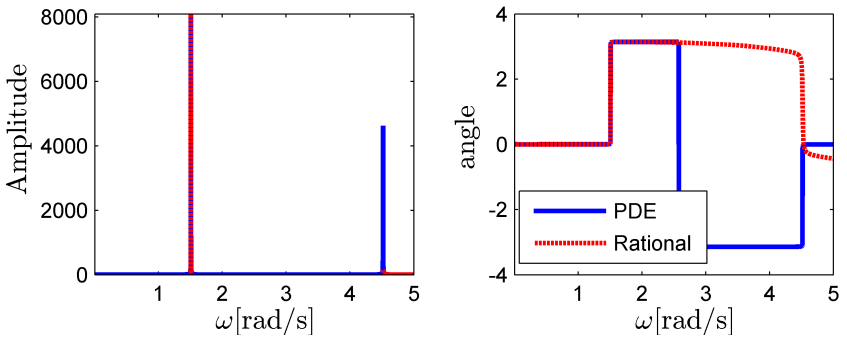

Figure D.15: Frequency diagram: $\bar{V}_p(0)/\bar{V}_p(L)$, $r = 64$, $\sigma = 0.01$.

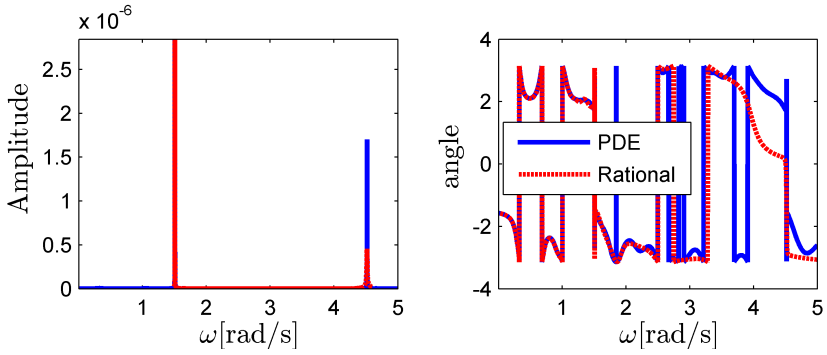

Figure D.16: Frequency diagram: $\bar{V}_p(0)/P_i(0)$, $r = 64$, $\sigma = 0.01$.

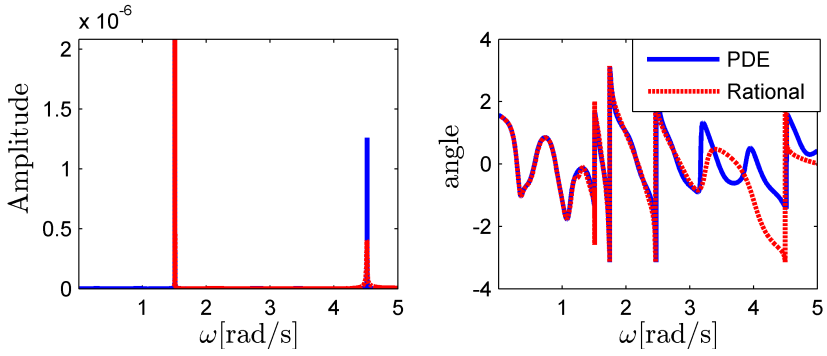

Figure D.17: Frequency diagram: $\bar{V}_p(0)/P_a(0)$, $r = 64$, $\sigma = 0.01$.

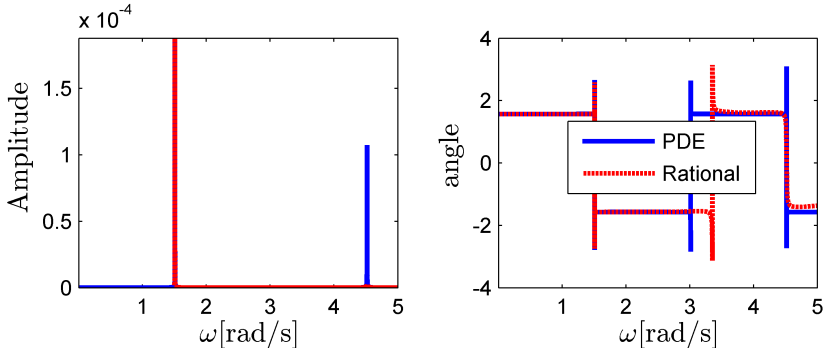

Figure D.18: Frequency diagram: $\bar{V}_p(0)/P_p(0)$, $r = 64$, $\sigma = 0.01$.

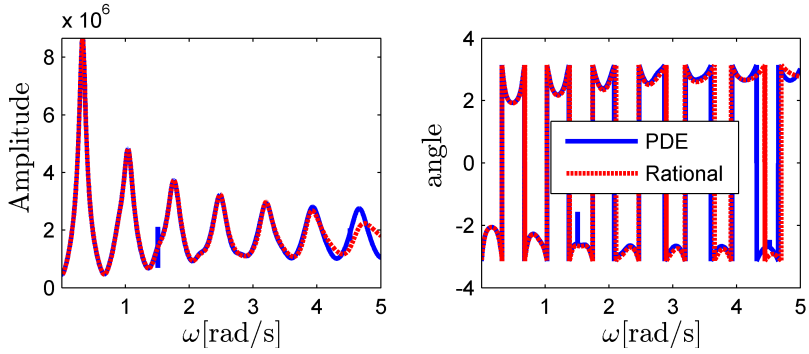

Figure D.19: Frequency diagram: $P_i(L)/\bar{V}_i(L)$, $r = 64$, $\sigma = 0.01$.

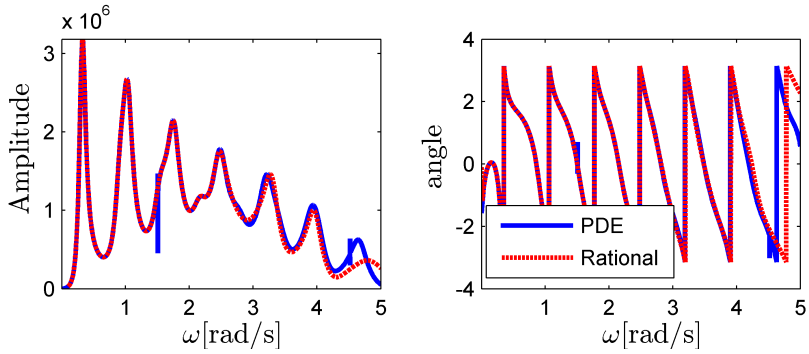

Figure D.20: Frequency diagram: $P_i(L)/\bar{V}_a(L)$, $r = 64$, $\sigma = 0.01$.

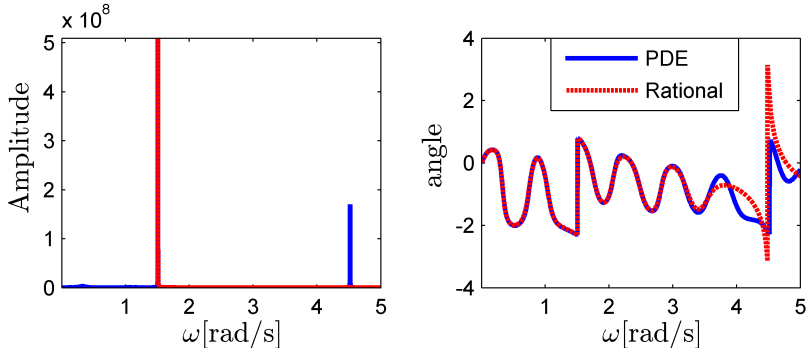

Figure D.21: Frequency diagram: $P_i(L)/\bar{V}_p(L)$, $r = 64$, $\sigma = 0.01$.

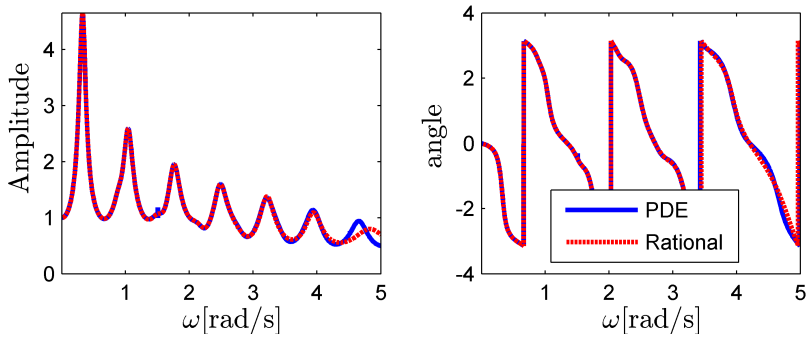

Figure D.22: Frequency diagram: $P_i(L)/P_i(0)$, $r = 64$, $\sigma = 0.01$.

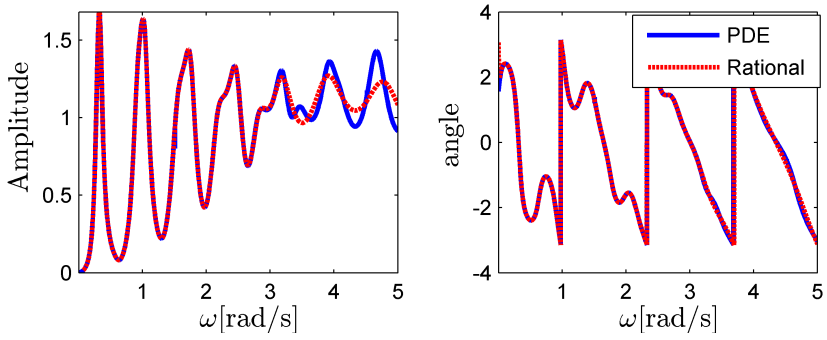

Figure D.23: Frequency diagram: $P_i(L)/P_a(0)$, $r = 64$, $\sigma = 0.01$.

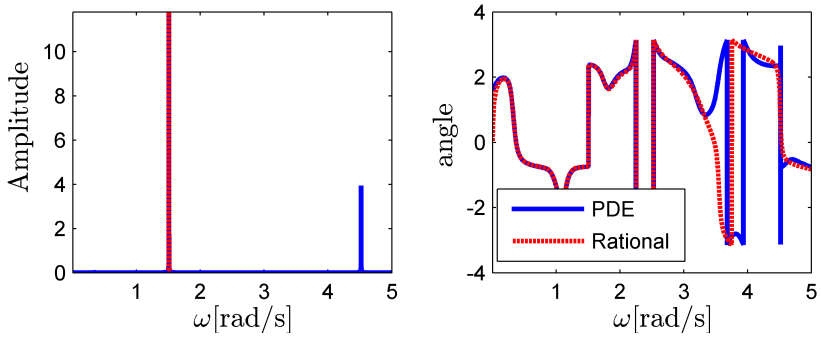

Figure D.24: Frequency diagram: $P_i(L)/P_p(0)$, $r = 64$, $\sigma = 0.01$.

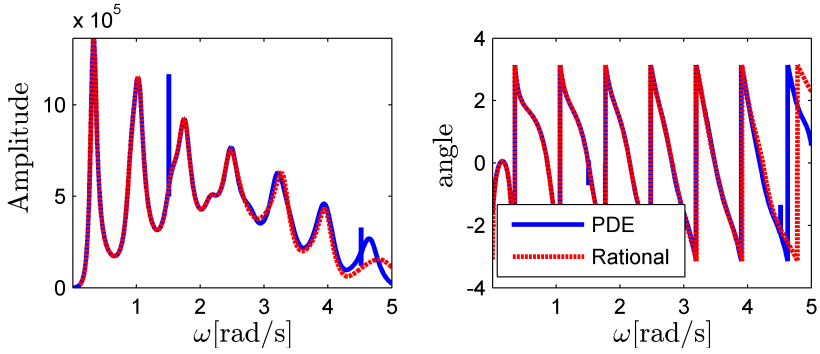

Figure D.25: Frequency diagram: $P_a(L)/\bar{V}_i(L)$, $r = 64$, $\sigma = 0.01$.

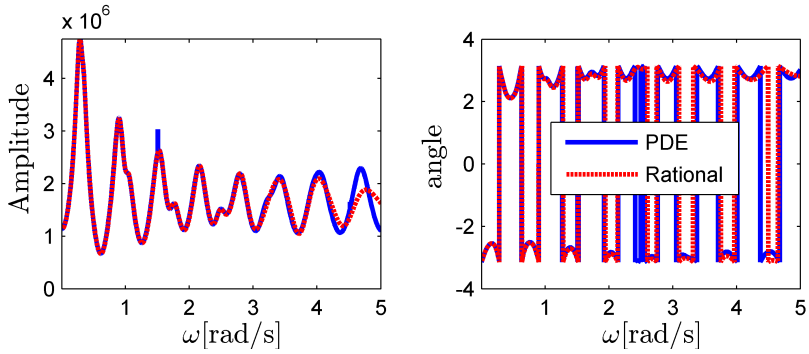

Figure D.26: Frequency diagram: $P_a(L)/\bar{V}_a(L)$, $r = 64$, $\sigma = 0.01$.

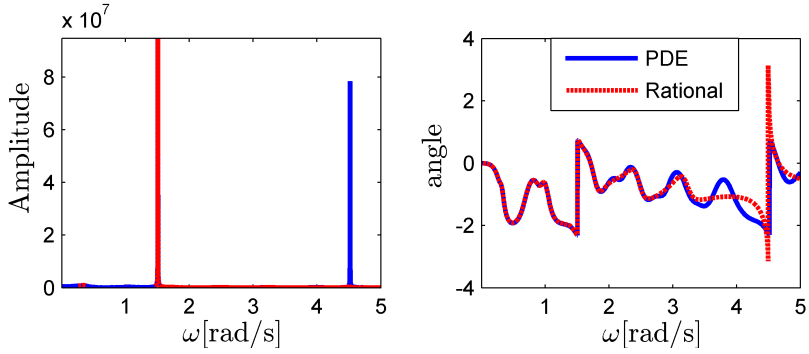

Figure D.27: Frequency diagram: $P_a(L)/\bar{V}_p(L)$, $r = 64$, $\sigma = 0.01$.

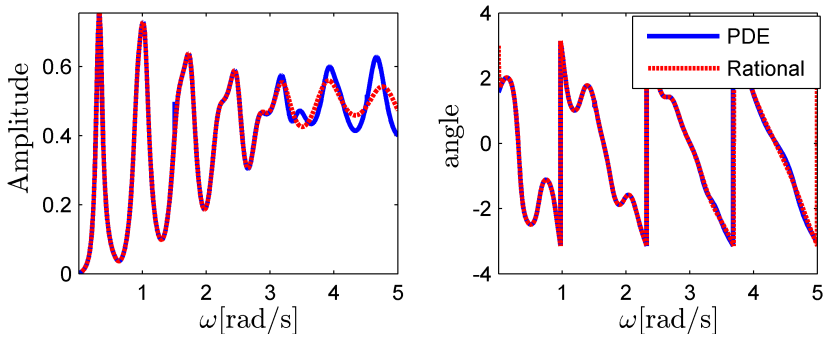

Figure D.28: Frequency diagram: $P_a(L)/P_i(0)$, $r = 64$, $\sigma = 0.01$.

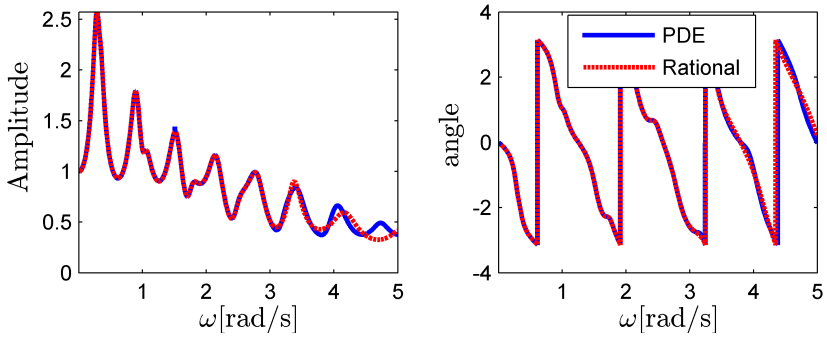

Figure D.29: Frequency diagram: $P_a(L)/P_a(0)$, $r = 64$, $\sigma = 0.01$.

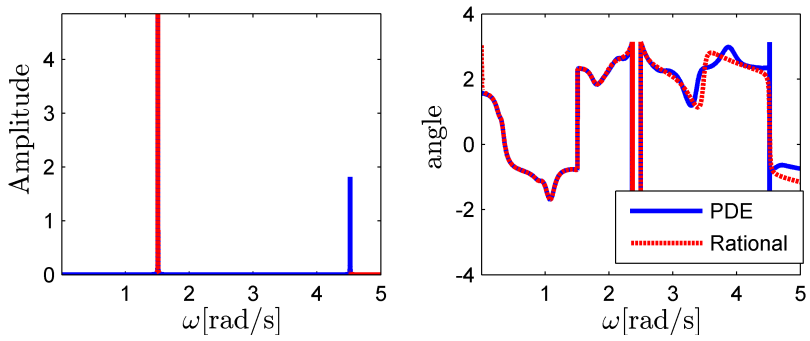

Figure D.30: Frequency diagram: $P_a(L)/P_p(0)$, $r = 64$, $\sigma = 0.01$.

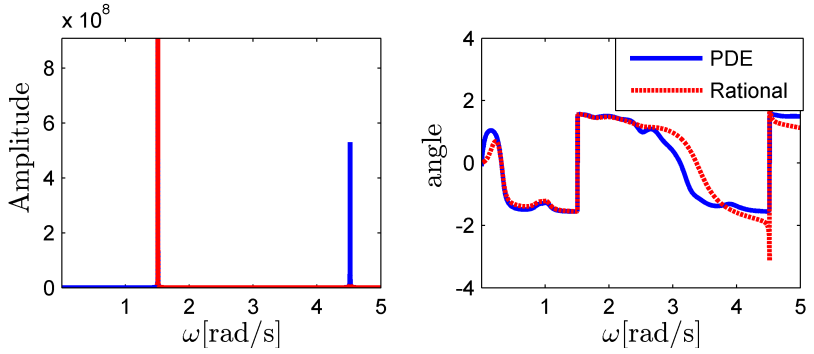

Figure D.31: Frequency diagram: $P_p(L)/\bar{V}_i(L)$, $r = 64$, $\sigma = 0.01$.

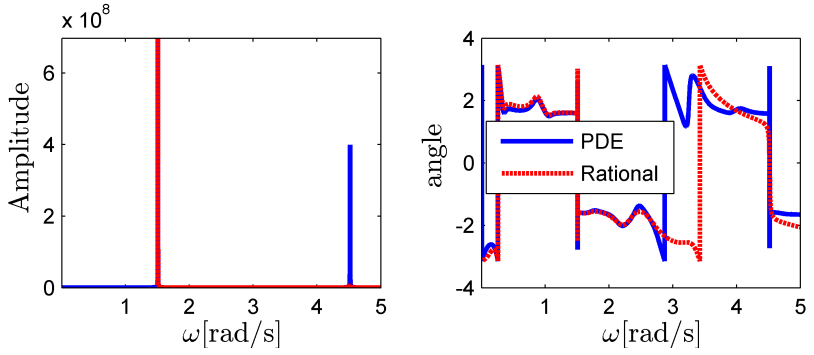

Figure D.32: Frequency diagram: $P_p(L)/\bar{V}_a(L)$, $r = 64$, $\sigma = 0.01$.

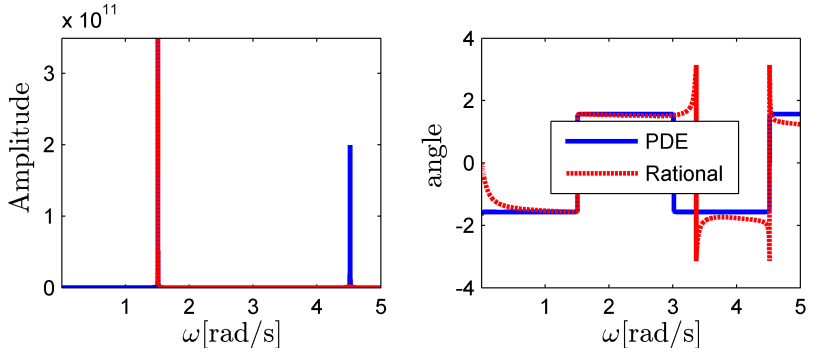

Figure D.33: Frequency diagram: $P_p(L)/\bar{V}_p(L)$, $r = 64$, $\sigma = 0.01$.

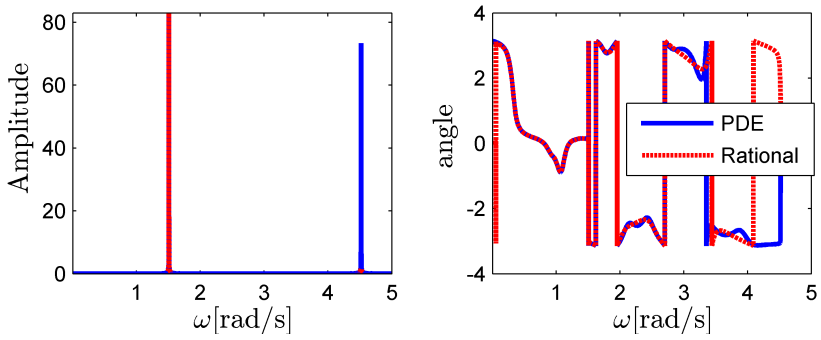

Figure D.34: Frequency diagram: $P_p(L)/P_i(0)$, $r = 64$, $\sigma = 0.01$.

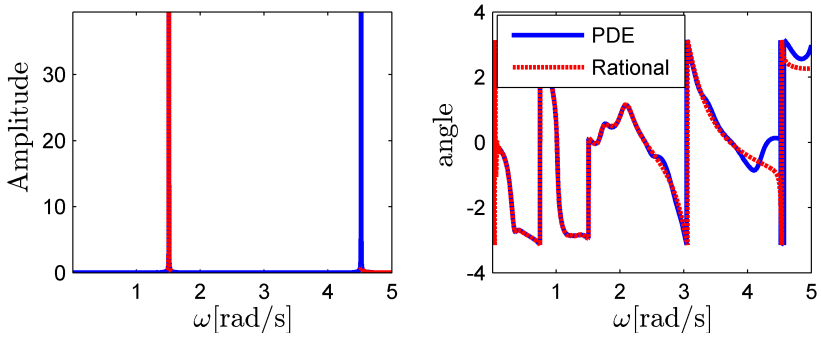

Figure D.35: Frequency diagram: $P_p(L)/P_a(0)$, $r = 64$, $\sigma = 0.01$.

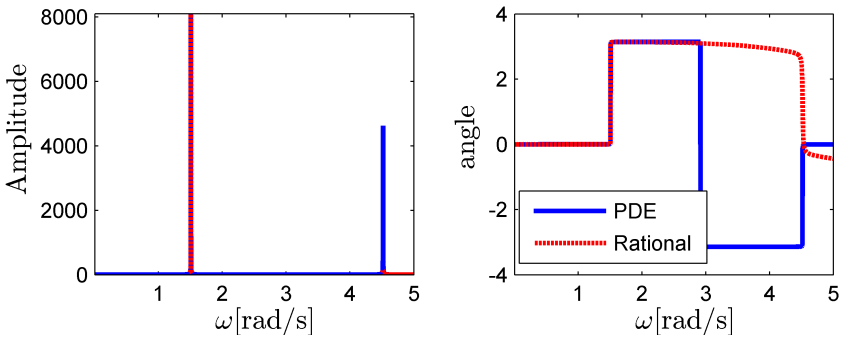

Figure D.36: Frequency diagram: $P_p(L)/P_p(0)$, $r = 64$, $\sigma = 0.01$.